République Algérienne Démocratique et Populaire
Ministère de l'Enseignement Supérieur et de la Recherche Scientifique
Université 8 Mai 1945 Guelma

جامعة 8 ماي 1945 قالمة
UNIVERSITE 8 MAI 1945 GUELMA

Faculté des Science et de la Technologie
Département de Génie Civil et Hydraulique
Laboratoire de Génie Civil et Hydraulique (LGCH)

THÈSE

EN VUE DE L'OBTENTION DU DIPLOME DE DOCTORAT EN 3ème CYCLE

Domaine : Science et technologie. Filière : Génie Civil.
Spécialité : Structures.

Présentée par

BOUROUMANA Issam

Intitulée

Contribution à l'étude du comportement sous chargement sévère des éléments renforcés de structures en béton armé

Soutenue le : 07/07/2025. Devant le Jury composé de :

Nom et Prénom	Grade	Université	
Mr. GUENFOUD Mohamed	Professeur	8 May 1945- Guelma	Président
Mr. NAFA Zahreddine	Professeur	8 May 1945- Guelma	Rapporteur
Mme. NIGRI Ghania	MCA	8 May 1945- Guelma	Co-Rapporteur
Mr. HACENE CHAOUCHE Abdelmadjid	Professeur	Badji Mokhtar- Annaba	Examinateur
Mr. MADI Rafik	Professeur	8 May 1945- Guelma	Examinateur
Mr. BOURAS Faouzi	MCB	8 May 1945- Guelma	Invité

Année Universitaire : 2024/2025

بسم الله الرحمن الرحيم

Dedication

This thesis is lovingly dedicated to:

To ***my parents****, for their endless love, sacrifices, and unwavering support. You have been my guiding light and my greatest source of inspiration.*

To ***my siblings****, for their encouragement, kindness, and belief in me through every step of this journey.*

To ***Anes****,* ***Djana****, and* ***Adam****, whose smiles, laughter, and innocence have brought so much joy and motivation during challenging times.*

To my ***dear friends****, for their steadfast support, shared laughter, and encouragement that kept me going.*

Thank you all for your love, kindness, and unwavering presence in my life. This accomplishment would not have been possible without you.

Acknowledgments

In light of this work, I would first like to thank ALLAH, the All-Powerful, for all the blessings in my life and for granting me the courage, strength, perseverance, and patience to complete this modest scientific contribution.

I am profoundly grateful to many individuals who made the completion of this Ph.D. thesis possible. I extend my warmest thanks to:

My supervisor, Pr. NAFA Zahreddine*, for his invaluable guidance, support, and encouragement throughout these years. His expertise, understanding, and patience have greatly enriched my research experience.*

My co-supervisor, Dr. Nigri Ghania*, for her guidance and support throughout my research, which have been crucial to the success of this thesis.*

The team of the Civil and Hydraulic Engineering Laboratory (LGCH) *and its director,* ***Pr. Nouaouria Mohamed Salah****, for their scientific services and orientations, which were instrumental in shaping this work.*

The members of the jury*, for their time, insightful feedback, and constructive evaluations, which have enhanced the quality of this thesis.*

I also wish to thank all those who have supported me, directly or indirectly, throughout these years of research and study.

Finally, my heartfelt thanks go to all my teachers and colleagues for their encouragement, collaboration, and camaraderie during this journey.

List of Publications

ORCID ID: https://orcid.org/0000-0002-5808-1910

ResearchGate: https://www.researchgate.net/profile/Issam-Bouroumana

The research conducted in this thesis has led to the following publications:

Journal Articles

Bouroumana Issam, Nafa Zahreddine, Nigri Ghania. Numerical Study on the Retrofitting of Exterior RC Beam-column Joints with CFRP Composites Using the Grooving Method. Periodica Polytechnica Civil Engineering, 69(1), pp. 175–192, 2025. https://doi.org/10.3311/PPci.37522.

International Conferences

Bouroumana Issam, Nafa Zahreddine, Nigri Ghania. Numerical Investigation of Retrofitting RC Exterior Beam-Column Joints with CFRP Composites via the Grooving Method. International Seminar on Materials and Engineering Structures (ISMES' 2024), Relizane, Algeria, October 26–27, 2024.

Bouroumana Issam, Nafa Zahreddine, Nigri Ghania. Nonlinear Simulation of RC Exterior Beam-Column Joints Retrofitted with CFRP Sheets. 4th International Symposium on Construction Management and Civil Engineering (ISCMCE-2024), Skikda, Algeria, November 04–05, 2024.

Bouroumana Issam, Nafa Zahreddine, Nigri Ghania. Numerical Analysis of Retrofitting Shear-Deficient RC Beam-Column Joints with CFRP Composites: Impact of Column Axial Load. The First International Conference on Civil Engineering and Materials Innovation (1st ICCEMI 2024), Mascara, Algeria, December 09–10, 2024.

National Conferences

Bouroumana Issam, Nafa Zahreddine, Nigri Ghania. Investigating the Influence of GFRP-Transverse Reinforcement on the Seismic Performance of RC Beam-Column Joints: A Numerical Study. Congrès National de Génie Civil et d'Hydraulique (CNGCH 2023), Guelma, Algeria, November 12–13, 2023.

Bouroumana Issam, Nary Hassan, Nigri Ghania, Benamara Fatima Zohra, Kechekar Chiraz, Nafa Zahreddine. Étude du Comportement des Poutres en Béton Armé Renforcées par Composite en Polymère. 2ème Séminaire National de Génie Civil (SNGC 2022), Souk-Ahras, Algeria, December 18–19, 2022.

Table of Contents

Abstract

Reinforced concrete (RC) beam-column joints (BCJs) are one of the critical structural members in buildings, often lacking adequate seismic detailing, which makes them vulnerable to brittle failure during earthquakes. This deficiency can lead to the collapse of an entire building under severe seismic loading. Retrofitting these joints is crucial for enhancing structural resilience. While fiber-reinforced polymer (FRP) composites have been widely used for this purpose, premature debonding from the concrete surface remains a major challenge. To mitigate this issue, concrete surface preparation using the grooving method (GM) has emerged as a promising technique, enhancing FRP-concrete bond and retrofit efficiency.

This study numerically investigates the behavior of non-seismically designed BCJs retrofitted with carbon fiber-reinforced polymer (CFRP) sheets using the GM. A numerical approach is adopted using the finite element software ABAQUS, employing an explicit solver to accurately capture the nonlinear response of retrofitted joints. The concrete damaged plasticity (CDP) model is utilized to simulate concrete behavior, with a sensitivity analysis conducted on its key parameters. The FRP-concrete interface is modeled as a perfect bond, reflecting the strong adhesion provided by the GM. Numerical results are validated against experimental data from three BCJ specimens selected from the literature, showing good agreement in terms of load-displacement behavior, peak loads, and failure modes.

Parametric analyses are conducted to evaluate the influence of key design parameters on the performance of retrofitted joints. These include column axial load ratio, beam reinforcement ratio, joint aspect ratio in conjunction with joint transverse reinforcement, and fiber type. Results indicate that CFRP retrofitting significantly enhances joint strength and ductility, particularly in joints with pronounced shear deficiencies. The study also highlights the critical role of these design parameters in governing joint shear capacity and, consequently, the effectiveness of the retrofitting technique.

Keywords: Retrofitting, Finite element modelling, Composite materials, Grooving method, Non-seismically joints.

Résumé

Les nœuds poutre-poteau en béton armé (BA) sont des éléments structuraux essentiels dans les bâtiments. Cependant, ils manquent souvent de détails sismiques adéquats, les rendant vulnérables à des ruptures fragiles lors de séismes, ce qui peut entraîner l'effondrement total d'une structure sous des charges sismiques sévères. La réhabilitation de ces nœuds est donc cruciale pour améliorer la résilience structurelle. Bien que les composites en polymère renforcé de fibres (PRF) soient largement utilisés à cet effet, Le décollement prématuré du PRF de la surface du béton demeure un défi majeur. Pour atténuer ce problème, la préparation de la surface du béton à l'aide de la méthode de rainurage (MR) est apparue comme une technique prometteuse, améliorant l'adhérence PRF-béton et l'efficacité de la réhabilitation.

Cette étude examine numériquement le comportement des nœuds poutre-poteau conçus sans considération sismique et réhabilités avec des feuilles de polymère renforcé de fibres de carbone (PRFC) en utilisant la MR. Une approche numérique est adoptée en utilisant le logiciel d'éléments finis ABAQUS, employant un solveur explicite pour capturer avec précision la réponse non linéaire des nœuds renforcés. Le modèle de plasticité endommagée du béton (CDP) est utilisé pour simuler le comportement du béton, avec une analyse de sensibilité menée sur ses paramètres clés. L'interface PRF-béton est modélisée comme une liaison parfaite, reflétant la forte adhésion fournie par la MR. Les résultats numériques sont validés par rapport aux données expérimentales de trois spécimens de nœuds poutre-poteau sélectionnés dans la littérature, montrant une bonne concordance en termes de comportement charge-déplacement, charges maximales et modes de rupture.

Des analyses paramétriques sont menées pour évaluer l'influence des principaux paramètres de conception sur la performance des nœuds réhabilités. Ces paramètres incluent le rapport de charge axiale du poteau, le raport d'armature de la poutre, le rapport d’aspect du nœud en lien avec son armature transversale, et le type de fibres utilisées. Les résultats indiquent que la réhabilitation par PRFC améliore significativement la résistance et la ductilité des nœuds, en particulier pour ceux présentant des déficiences en cisaillement. L'étude met également en évidence le rôle critique de ces paramètres de conception dans la capacité portante au cisaillement du nœud et, par conséquent, dans l'efficacité de la technique de réhabilitation.

Mots-clés : Réhabilitation, Modélisation par éléments finis, Matériaux composites, Méthode de rainurage, Nœuds non parasismique.

ملخص

تُعتبر وصلات الكمرات والأعمدة الخرسانية المسلحة (BCJs) من العناصر الإنشائية الحيوية في المباني. إلا أن نقص التفاصيل التصميمية المقاومة للزلازل يجعلها عرضة للانهيار الهش أثناء الهزات الأرضية، مما قد يؤدي إلى انهيار المبنى بالكامل تحت الأحمال الزلزالية الشديدة. لذا، فإن تعزيز هذه الوصلات يُعد أمرًا بالغ الأهمية لتحسين مرونة الهيكل. وعلى الرغم من الاستخدام الواسع للمواد المركبة المسلحة بالألياف (FRP) لهذا الغرض، إلا أن انفصالها المبكر عن سطح الخرسانة لا يزال تحديًا رئيسيًا. وللتغلب على هذه المشكلة، ظهرت تقنية تحضير سطح الخرسانة باستخدام طريقة التخديد (GM) كحل واعد لتعزيز التصاق FRP بالخرسانة وزيادة كفاءة التعزيز.

تهدف هذه الدراسة إلى تحليل سلوك وصلات الكمرات والأعمدة غير المصممة لمقاومة الزلازل والمعززة بألواح من ألياف الكربون البوليمرية المسلحة (CFRP) باستخدام طريقة التخديد (GM) من خلال النمذجة العددية. تم استخدام برنامج العناصر المحدودة ABAQUS مع محلل عددي صريح لتقييم الاستجابة غير الخطية للوصلات المعززة بدقة. تم تطبيق نموذج تلف اللدونة للخرسانة (CDP) لمحاكاة سلوكها، مع إجراء تحليل حساسية لمعاييره الرئيسية. كما تم نمذجة رابطة الخرسانة و FRP كرابطة مثالية، مما يعكس قوة الالتصاق الناجمة عن طريقة التخديد. تم التحقق من النتائج العددية مقابل البيانات التجريبية لثلاث عينات من وصلات الكمرات والأعمدة المختارة من الأدبيات، وأظهرت توافقًا جيدًا من حيث سلوك الحمل-الإزاحة، وأحمال الذروة، وأنماط الانهيار.

تم إجراء تحليلات بارامترية لتقييم تأثير معايير التصميم الرئيسية على أداء الوصلات المعززة، مثل نسبة حمل العمود المحوري، نسبة تسليح العارضة، نسبة أبعاد الوصلة بالتزامن مع التسليح العرضي للوصلة، ونوع الألياف. أظهرت النتائج أن استخدام ألواح CFRP يعزز بشكل كبير من قوة الوصلات وليونتها، خاصة في الحالات التي تعاني من ضعف مقاومة القص. كما أكدت الدراسة على الدور الحاسم لهذه المعايير التصميمية في تحديد قدرة القص للوصلة، وبالتالي فعالية تقنية التعزيز .

الكلمات المفتاحية: التعزيز الإنشائي، نمذجة العناصر المحدودة، المواد المركبة، طريقة التخديد، الوصلات غير المصممة لمقاومة الزلازل.

List of Figures

List of Tables

List of Symbols

Symbol	Description
Δ	Lateral displacement
L	Length of the beam measured from the column face
H	Height of the column
R	Residual force
F_{ext}	External forces
F_{int}	Internal forces
Δ_t	Time increment
K_{tang}	Stiffness matrix
Δu	Displacement correction
K_{tang}^{-1}	Inverse of stiffness matrix
M	Nodal mass matrix
$\ddot{u}$	Nodal acceleration
$\dot{u}$	Nodal velocity
u	Nodal displacement
P	Externally applied force
I	Internal element force
$\Delta stable$	Stability limit
L_{min}	Smallest element length in the mesh
c_d	Material wave speed
E	Young’s modulus
ρ	Material density
σ	Cauchy stress tensor
d_ε	Strain increment
d_c	Compression damage variable
d_t	Tension damage variable
d	Damage variable
D_0^{el}	Initial (undamaged) elastic stiffness
D^{el}	Degraded elastic stiffness

ε	Total strain
ε^{pl}	Plastic strain
$\bar{\sigma}$	Effective stress tensor
F	Yield function
α, β, γ	Dimensionless material constants
$\bar{p}$	Effective hydrostatic pressure
$\bar{q}$	Equivalent von mises stress
$\bar{\sigma}_{max}$	Maximum eigenvalue of tensor $\bar{\sigma}$
σ_{b0}/σ_{c0}	Ratio of biaxial to uniaxial compressive strengths.
ψ	Dilation angle
ε	Flow potential eccentricity
K_c	Ratio of second stress invariant on the tensile meridian to that on the compressive meridian
f_c'	Concrete compressive strength
σ_{c0}	Concrete yield stress
ε_0	Concrete strain at compressive strength
ε_f	Concrete ultimate strain
E_C	Modulus of elasticity of concrete
ε_c	Concrete strain under given stress level (σ_c)
σ_c	Concrete compressive stress
E_0	Secant modulus of concrete
σ_f	Concrete compressive stress at failure
R	Ratio relation
R_E	Modular ratio
R_σ	Stress ratio
R_ε	Strain ratio
$\tilde{\varepsilon}_c^{in}$	Concrete inelastic strain
ε_c	Concrete total strain
ε_{0c}^{el}	Concrete elastic strain
$\tilde{\varepsilon}_c^{pl}$	Concrete plastic strain
d_c	Concrete compressive damage

f_t	Tensile strength of concrete
G_f	Fracture energy
G_{f0}	Base fracture energy
d_{max}	Maximum aggregate size
u_t^{ck}	Cracking displacement
u_t^{pl}	Plastic displacement
d_t	Concrete tensile damage
l_0	Unit length
E_1	Young's modulus in the direction of symmetry axis (axis 1)
$E_2 = E_3$	Young's modulus in the isotropic plane (axes 2 and 3)
$\upsilon_{12} = \upsilon_{13}$	Poisson's ratio: strain in 2 or 3 due to stress in 1
υ_{23}	Poisson's ratio: strain in 3 due to stress in 2
$G_{12} = G_{13}$	Shear modulus in 1–2 or 1–3 plane
G_{23}	Shear modulus in the isotropic plane (2–3 plane)
X^t, X^c	Tensile and compressive strengths in the fiber direction
Y^t, Y^c	Tensile and compressive strengths perpendicular to the fiber direction
S^l, S^t	Longitudinal and transverse shear strengths
α	Coefficient that determines of the shear stress to the fiber tensile initiation
M	Damage operator
d_f, d_m, d_s	Internal damage variables representing fiber, matrix and shear damage
A_g	Column cross-sectional area
P_u	Peal load
Δ_u	Displacement at peak
v_j	Joint shear strength
ρ_b	Beam longitudinal reinforcement ratio
η	Joint aspect ratio
h_b	Beam depth
h_c	Column depth

*Chapter **I**:*

Introduction

Chapter I: Introduction

I.1 BACKGROUND

Reinforced Concrete (RC) structures, which include buildings and bridges, are integral to modern infrastructure due to their strength, versatility, and cost-effectiveness. However, many RC structures constructed in the 1960s and 1970s did not conform to modern seismic design standards, particularly in earthquake-prone regions. As a result, these structures are highly vulnerable to seismic damage, which can be attributed to poor reinforcement detailing, substandard material quality, and the lack of design provisions for dynamic loading.

Beam-column joints (BCJs) are critical components in RC frames, as they provide the connection between beams and columns, ensuring load transfer during seismic events. However, BCJs are particularly susceptible to shear failure when subjected to lateral forces such as earthquakes. Many BCJs were originally designed based on outdated codes that did not account for modern seismic loading conditions, leaving them prone to brittle and sudden failures. These deficiencies are exacerbated by factors like insufficient transverse reinforcement, inadequate anchorage of beam longitudinal reinforcement, weak column-strong beam configurations, and low joint shear strength.

As shown in Figure I.1, there are significant differences in the reinforcement detailing between non-seismically designed and seismically designed BCJs, which play a decisive role in their performance during seismic events. The main differences between these two types of joints are as follows:

Non-Seismically Designed Joint

- *Column Lap-Splice Above Joint Face*: The column lap-splice is located above the joint core, which can cause premature slippage of the column's longitudinal reinforcement. This results in a wide pullout crack at the column above the slab, further compromising the joint's performance during seismic loading.
- *Insufficient Transverse Reinforcement*: The joint core lacks adequate stirrups or ties, resulting in poor confinement of the concrete and ineffective shear resistance.
- *Inadequate Anchorage of Beam Longitudinal Bars*: The beam longitudinal reinforcement is not anchored with sufficient development length, and not bent at 90° or 180° leading to premature bond failure or slippage.

- *Weak Column-Strong Beam Behavior*: This configuration often violates the capacity design principle, where the column should be stronger than the beam to prevent joint failure.
- *Brittle Shear Failure*: Due to these deficiencies, the joint core is vulnerable to brittle, sudden shear failure without warning, especially under seismic loading.

Seismically Designed Joint

- *Column Lap-Splice at Mid-Height:* In contrast, the column lap-splice is located at the mid-height of the column in seismically designed joints. This placement minimizes the risk of slippage and ensures that the column's longitudinal reinforcement is better anchored
- *Densely Spaced Transverse Reinforcement*: The joint core is reinforced with closely spaced stirrups or hoops, providing effective confinement to the concrete, enhancing shear capacity, and delaying the onset of joint shear failure.
- *Proper Anchorage of Beam Longitudinal Bars*: The beam longitudinal reinforcement extends beyond the joint core with a sufficient development length, and bent with 90° anchorage ensuring better stress transfer and preventing slippage.
- *Defined Critical Regions (l_0 and l_{cr})*: The critical regions near the column-beam interface are confined with closely spaced transverse reinforcement over the length l_0, and l_{cr} .
- *Strong Column-Weak Beam Design*: This configuration ensures that plastic hinges form in the beam rather than in the joint core or column, providing a more ductile failure mechanism and preventing joint collapse.

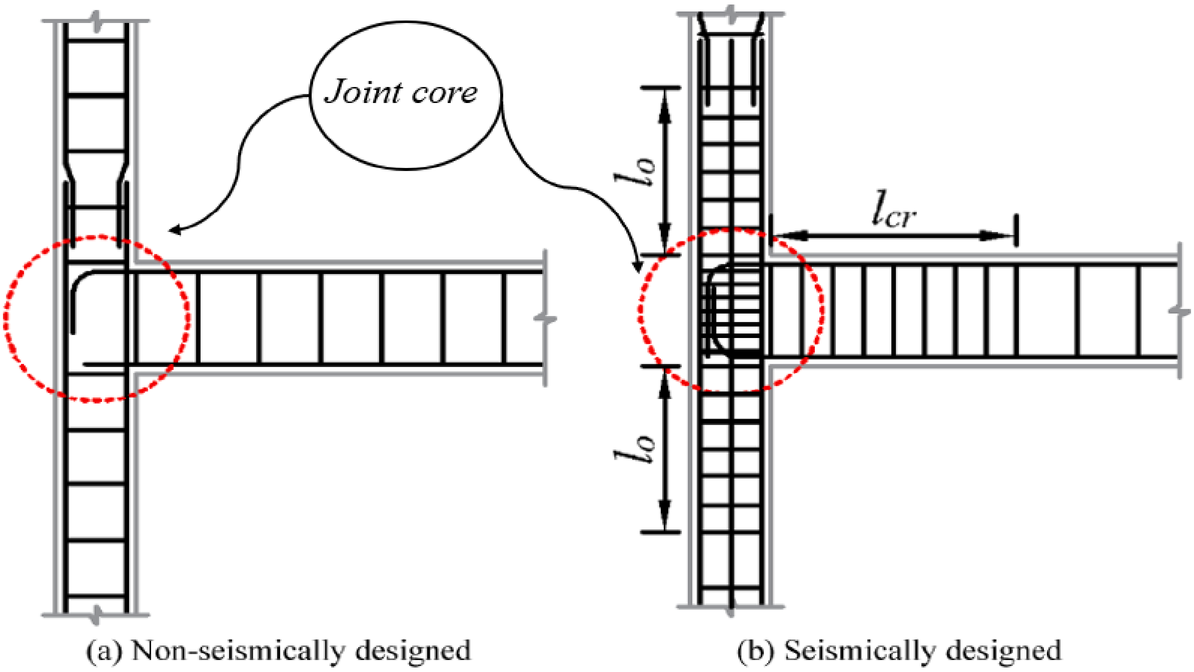

Figure I.1. Structural detailing differences between non-seismic and seismic RC beam-column joints [1].

Historical evidence from major seismic events underscores the detrimental effects of design flaws in RC BCJs. For instance, during the 2019 Kermanshah earthquake in Iran (Figure I.2), the 2008 Sichuan earthquake in China (Figure I.3), and the 1999 Kocaeli earthquake in Turkey (Figure I.4), structural collapses were frequently triggered by shear failures in the joint core. These failures are characterized by their brittle nature, occurring suddenly and with little to no warning. They exhibit minimal ductility, underscoring the pressing need for robust retrofitting strategies to enhance the seismic performance and safety of RC beam-column joints.

Figure I.2. Structural collapse of a RC building during the 2019 Kermanshah earthquake in Iran [2].

Figure I.3. Structural collapse of a RC building during the 2008 Sichuan earthquake in China [2].

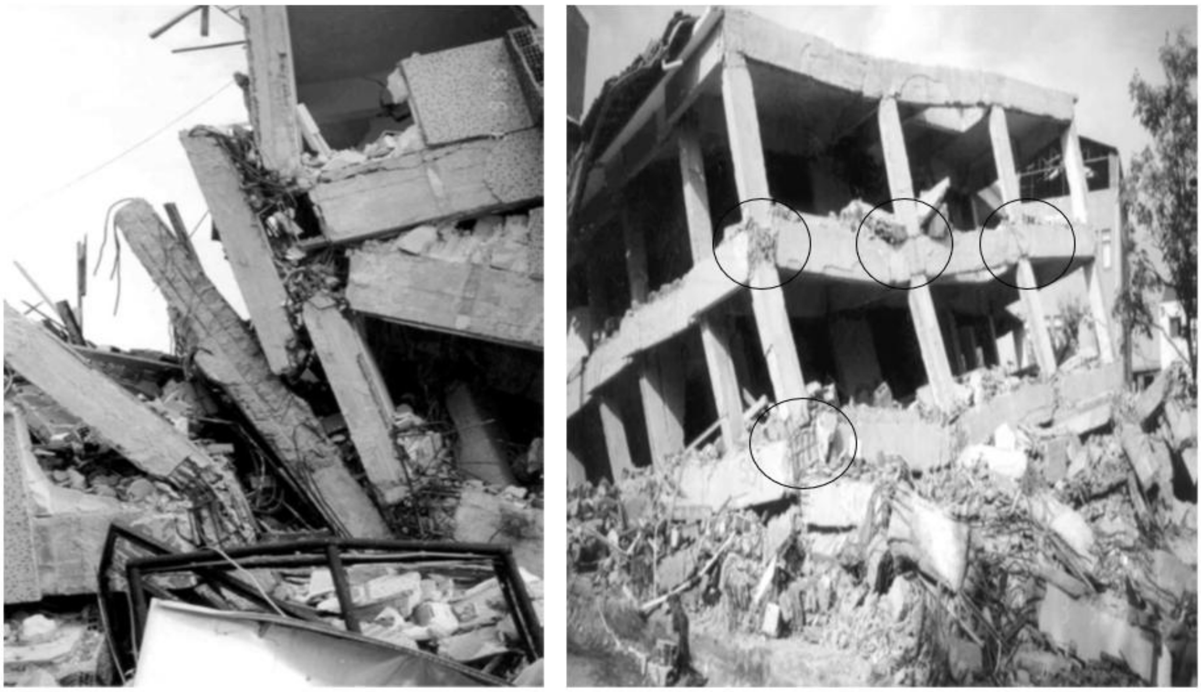

Figure I.4. Structural collapse of a RC building during the 1999 Kocaeli Earthquake in Turkey [3].

I.2 PROBLEM STATEMENT

Numerous retrofitting techniques have been developed to enhance the performance of under-designed BCJs. Traditional methods, such as RC and steel jacketing, have been used for decades and are known to improve strength, stiffness, and energy dissipation capacity while shifting plastic hinges away from the joint core into the beam. However, these methods involve extensive labor, increase member size, and add weight, altering the dynamic properties of the structure, which limits their practical application.

Fiber Reinforced Polymer (FRP) composites have emerged as an alternative retrofitting solution. The most common technique is the Externally Bonded Reinforcement (EBR) method, but it suffers from debonding issues that prevent FRP from achieving its full tensile capacity. To address this, the Near Surface Mounted (NSM) technique and the Grooving Method (GM) have been developed. Experimental studies have shown that the GM effectively mitigates debonding failures due to the strong bond between FRP composites and the concrete.

Despite these advancements, most research has focused on general retrofitting patterns rather than thoroughly validating numerical models such as those using the Concrete Damage Plasticity (CDP) model in ABAQUS against experimental results for GM-retrofitted joints. Furthermore, limited studies explore how different design parameters affect the performance of retrofitted joints.

I.3 RESEARCH OBJECTIVES

The primary goal of this study is to numerically investigate the performance of non-seismically designed BCJ retrofitted with CFRP sheets using the GM. Specific objectives include:

- Developing an accurate finite element model (FEM) using the CDP model in ABAQUS.
- Validating the numerical model against experimental data.
- Conducting a parametric study to examine the influence of various design parameters on the performance of the retrofitted joints (e.g., column axial load ratio, beam longitudinal reinforcement ratio, joint aspect ratio, joint transverse reinforcement and fibers types).
- Assessing the effectiveness of the GM in enhancing the shear capacity of retrofitted joints under the studied parameters.

I.4 THESIS LAYOUT

This thesis is organized into four chapters, each focusing on a specific aspect of the research. The contents of each chapter are summarized as follows:

1. **Chapter I: Introduction**

   This chapter introduces the background of the study, emphasizing the deficiencies of BCJ under seismic loading. It highlights the research problem, defines the objectives, and provides an overview of the thesis structure.

2. **Chapter II**: **Literature review**

   This chapter explores traditional retrofitting techniques, such as reinforced concrete and steel jacketing. Additionally, it reviews research on the retrofitting of BCJs using fiber-reinforced polymer (FRP) composite materials, presenting various techniques, including the Externally Bonded Reinforcement (EBR) method, Near Surface Mounted (NSM) technique, and Grooving Method (GM). Additionally, this chapter provides an overview of existing numerical modelling studies that investigate the effectiveness of retrofitting BCJs with FRP materials. It highlights the methodologies, material models, and findings of these studies to establish a foundation for the current research.

3. **Chapter III: Modelling and validation**

   This chapter details the development of finite element models using ABAQUS software to simulate the behaviour of retrofitted BCJs. It includes descriptions of material constitutive models, interaction modelling, geometry, boundary conditions, element types, and meshing techniques. The validation of the numerical models against experimental data is also discussed.

4. **Chapter IV: Parametric study**

   This chapter presents the results of the parametric study, examining the influence of various design parameters on the performance of retrofitted joints. The studied parameters include column axial load ratio, beam longitudinal reinforcement ratio, joint aspect ratio with joint transverse reinforcement and FRP types.

*Chapter **II**:*

Literature Review

Chapter II: Literature Review

II.1 INTRODUCTION

This chapter aims to provide an in-depth assessment and evaluation of the various confinement methods available in the literature for retrofitting BCJs. It begins with a comprehensive state-of-the-art review of traditional retrofitting techniques, including RC and steel jacketing. The focus then shifts to modern advancements, particularly the use of FRP composites for retrofitting. This chapter also delves into the different FRP retrofit techniques, discussing their respective advantages and disadvantages, thereby offering a thorough understanding of the evolution and current trends in BCJ retrofitting methods.

II.2 GENERAL

Since its invention in the 19th century, Portland cement has contributed to the widespread use of concrete as a primary construction material. Its versatility allows it to be molded into various shapes and sizes, making it suitable for different structural forms. Among these, reinforced concrete moment-resisting frames are particularly favored in the building industry due to their structural efficiency and adaptability to architectural designs. As illustrated in Figure II.1, reinforced concrete frame structures are composed of interconnected columns and beams, forming the structural framework. This system provides support for additional elements such as slabs, walls.

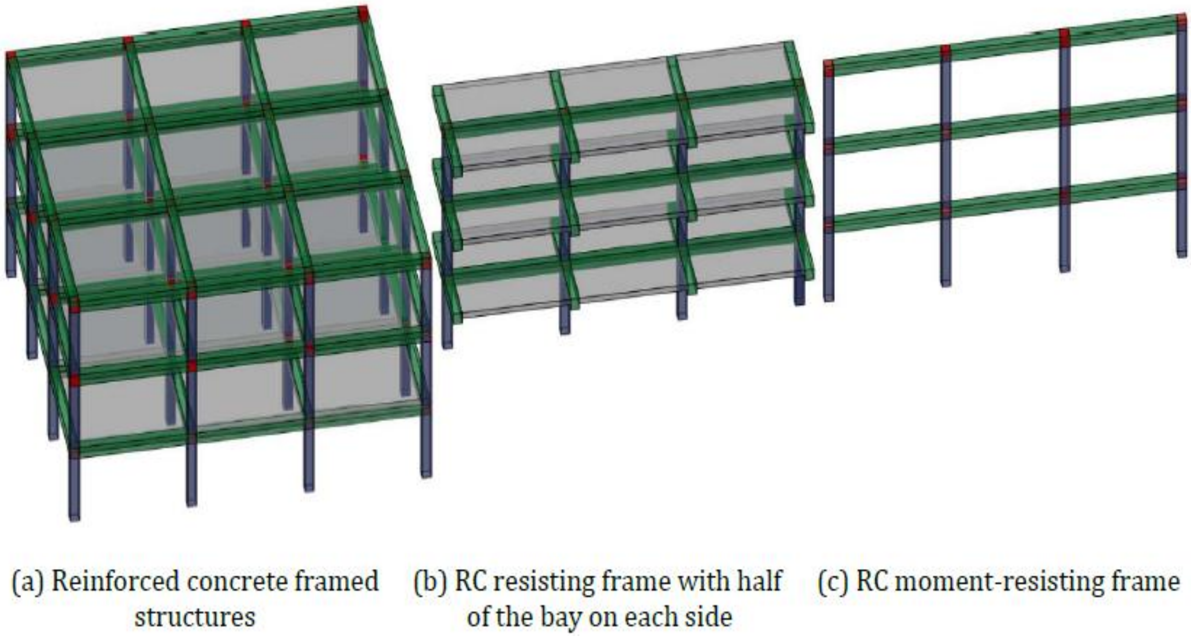
(a) Reinforced concrete framed structures (b) RC resisting frame with half of the bay on each side (c) RC moment-resisting frame

Figure II.1. Schematic representation of a standard reinforced concrete frame structure [2].

Although these structures perform efficiently under gravity loads, they have shown inadequate resistance to lateral forces. Traditionally, structural engineers considered an RC moment-resisting frame to consist solely of beams and columns (Figure II.2 (c)), connected by rigid joints that prevent relative rotation. As a result, joint shear deformation was assumed to be negligible [2]. When only gravity loads are applied (Figure II.2 (a)), this assumption remains valid since the joint panel zone experiences minimal shear force and remains uncracked throughout the loading process. However, under lateral loads (Figure II.2 (b)), this assumption becomes inaccurate, as the joint panel zones experience significant shear forces. As a result, their shear deformation plays a crucial role in the overall structural response and cannot be ignored (Figure II.2 (d)). To accurately represent the behaviour of RC frame structures, it is essential to model the joint as a separate structural element alongside beams and columns (Figure II.2 (f)).

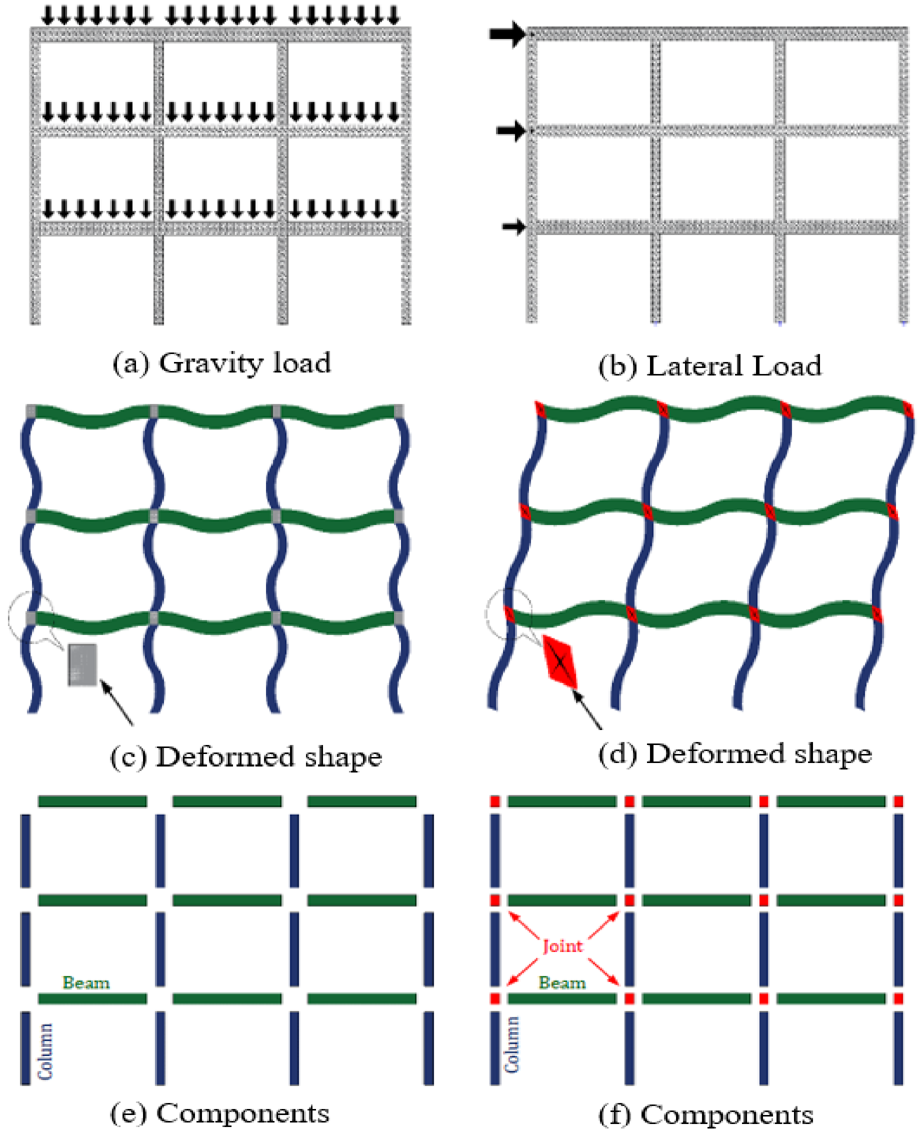

(a) Gravity load (b) Lateral Load

(c) Deformed shape (d) Deformed shape

(e) Components (f) Components

Figure II.2. Moment-resisting frame subjected to gravity and lateral load [2].

II.3 BEAM COLUMN JOINTS

RC frame structures constructed prior to the 1970s often lack adequate detailing compared to those designed according to modern seismic standards. BCJs in these older structures are particularly vulnerable to shear failure under lateral forces. This failure is due to high shear stresses in the joint panel (Figure II.2 (d)), caused by opposing moments on either side of the joint core. Such shear failure is problematic because it negatively impacts the overall seismic performance of RC buildings. Joint shear failure is a brittle failure mode that reduces the frame's ductility. Additionally, its early occurrence can prevent beams from achieving their maximum flexural capacity. Severe joint damage can ultimately lead to the collapse of the structure, especially in seismic regions, if the building was designed using outdated design codes before modern seismic provisions were implemented. As a result, joint shear failure has a detrimental effect on the seismic resilience of RC structures.

The focus on exterior BCJs (Figure II.3), rather than interior ones, is due to their greater vulnerability to seismic damage. The seismic behaviour and failure mechanisms of exterior BCJs with minimal or no transverse reinforcement have been widely investigated. This section provides an overview of experimental studies examining the structural response of these joints when subjected to cyclic lateral loading.

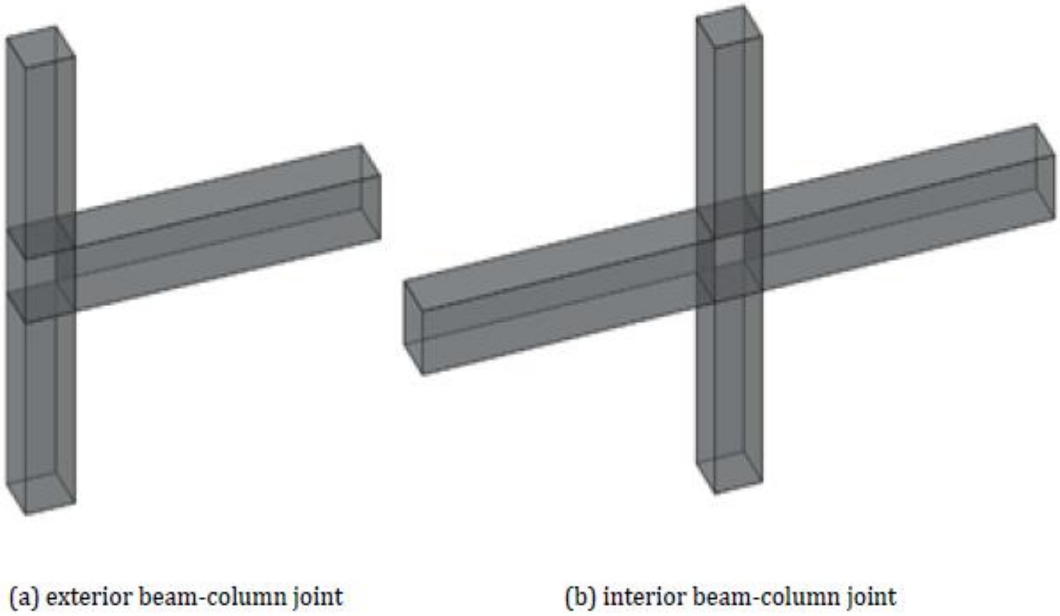

Figure II.3. Schematic of 2D beam-column joint [2].

Clyde et al. [4] tested four half-scale RC exterior joints to study their behaviour in shear-critical mode. The specimens were designed based on 1960s-era buildings, which did not meet current seismic design standards. These joints lacked stirrups in the core, and the beam's longitudinal reinforcement was not adequately anchored at the connection. The specimens were subjected to quasi-static cyclic loading applied at the beam end, with a constant axial compressive force of $0.1f_c'A_g$ for the first two specimens and $0.25f_c'A_g$ for the remaining ones, applied at the top of the columns. The details of the specimens and the observed damage at the end of the tests are shown in Figure II.4. All specimens experienced joint shear failure due to insufficient shear resistance in the joint region. Furthermore, the results revealed that the joints with lower axial loads were more than 1.5 times more ductile than those with higher axial loads. However, higher axial loads enhanced the joint's shear capacity, with an 8% increase in shear capacity due to the increased confinement from the axial compressive load.

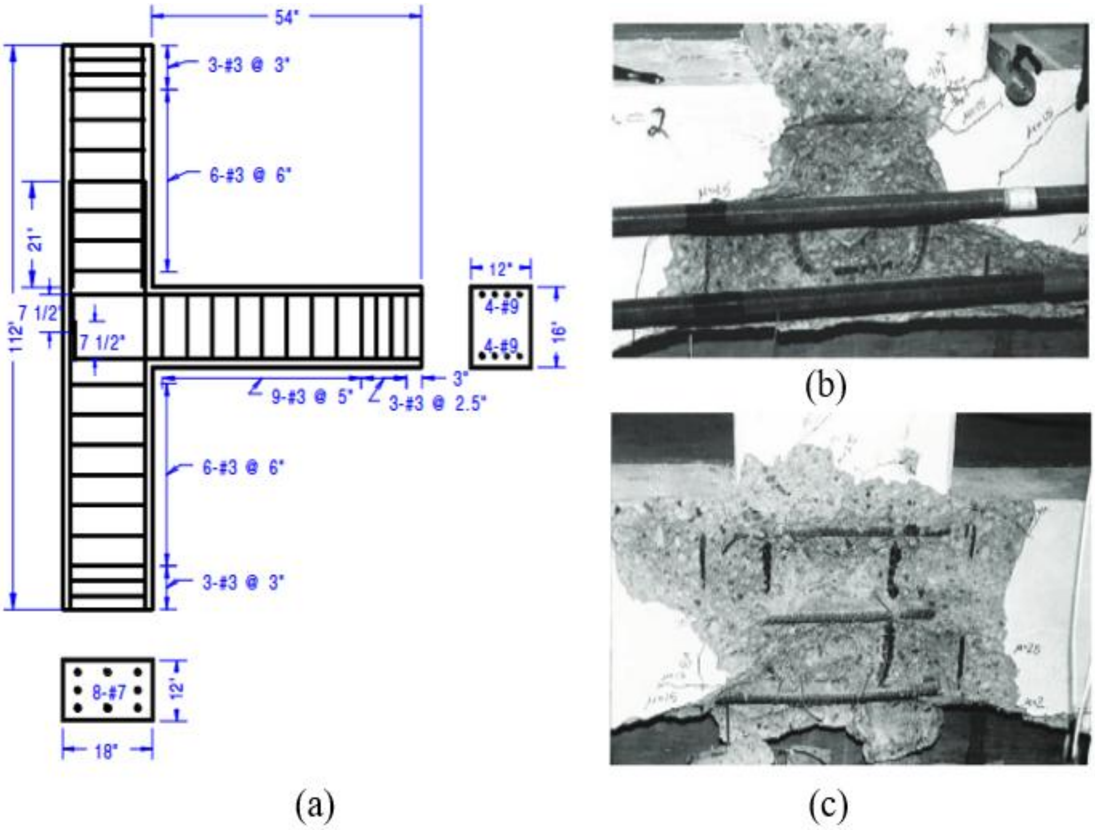

Figure II.4. Experimental investigation by Clyde et al [4]: (a) Reinforcement details; (b) Damage in the specimen under axial load of $0.1f_c'A_g$; (b) Damage in the specimen under axial load of $0.25f_c'A_g$.

An additional study conducted by Pantelides et al. [5] on the influence of column axial load on the seismic behaviour of exterior BCJ demonstrated that an increase in axial load enhances joint shear strength. However, this improvement comes at the expense of reduced ductility and lower energy dissipation capacity.

Wong and Kuang [6] investigated the influence of the joint aspect ratio on the performance of exterior joints. The joint aspect ratio is defined as the ratio of the beam depth to the column depth at the joint. Their study demonstrated that the joint aspect ratio significantly affects joint shear strength, with an increase in this ratio leading to a reduction in shear resistance (Figure II.5). Based on these findings, the study emphasized the necessity of considering the joint aspect ratio in the design process to ensure adequate joint performance under seismic loading

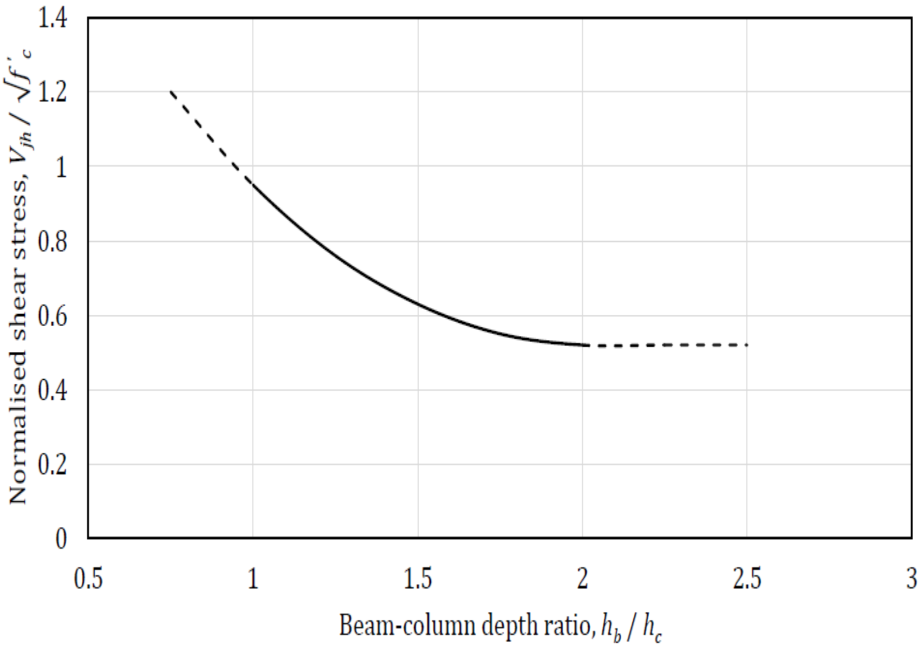

Figure II.5. Joint shear strength vs. joint aspect ratio [6].

The vulnerability of older RC frame structures, particularly the BCJs, to shear failure under lateral loading underscores the critical need for retrofitting. These joints, often lacking proper detailing and transverse reinforcement, are prone to brittle shear failure, which reduces the overall seismic performance of the structure. Studies have shown that exterior BCJs, in particular, are more susceptible to such failures, and joint shear failure can severely compromise a building’s ductility and load-carrying capacity. Given the detrimental effects of this failure mode on the seismic resilience of structures, retrofitting BCJs to enhance their shear resistance and improve their ductility is essential for ensuring the safety and stability of older RC frame buildings, especially those designed before modern seismic codes.

II.4 RETROFIT TECHNIQUES USING TRADITIONAL CONFINEMENT

Extensive research has investigated various retrofit approaches that utilize external confinement to enhance the performance of deficient BCJs. This section provides a comprehensive review and classification of these techniques, organized by the types of materials and methods employed. Furthermore, the practical limitations and challenges associated with implementing these techniques in real-world applications are discussed.

II.4.1 REINFORCED CONCRETE (RC) JACKETING

RC jacketing is a retrofit technique where an additional layer of RC is added around the member’s cross section to increase its structural capacity (Figure II.6). The process involves roughening the existing concrete surface, placing a new steel reinforcement cage, installing formwork, and casting fresh concrete in the prepared form. Achieving strong bonding between the existing and new concrete is critical, as this bond directly effects the overall effectiveness of RC jacketing.

Figure II.6. Example of RC jacketing applied to a BCJ for structural retrofitting [1].

Extensive research has demonstrated that RC jacketing is an effective method for enhancing the strength, stiffness, and energy dissipation capacity of BCJs. Additionally, it facilitates the relocation of plastic hinge formation from the joint to the beam [1]. Despite these advantages, RC jacketing presents several challenges, such as its labor-intensive application, increased cross-sectional dimensions of structural members, and added weight. These modifications can alter the dynamic characteristics of the structure, limiting the widespread adoption of this technique in practical applications.

II.4.2 STEEL JACKETING

Steel jacketing is a widely used technique for retrofitting BCJs, offering enhanced confinement and improved seismic performance. Various steel jacketing methods have been explored (Figure II.7), including corrugated steel sheets, pre-tensioned steel straps, L-shaped steel plates, steel angles, and haunch elements. Studies have demonstrated that extending steel confinement to the beam region can shift failure from the joint to the beam, improving stiffness, reducing stiffness degradation, and enhancing energy dissipation. Additionally, pre-tensioned steel jacketing has been identified as an effective strategy for strengthening deficient joints due to its unique ability to provide active confinement. The selection of proper jacketing dimensions, pre-tensioning levels, and anchorage details plays a critical role in optimizing the seismic performance of retrofitted joints. However, potential durability concerns, such as corrosion, must be considered to ensure long-term effectiveness. Overall, steel jacketing remains a promising retrofitting solution, as highlighted in reference [1].

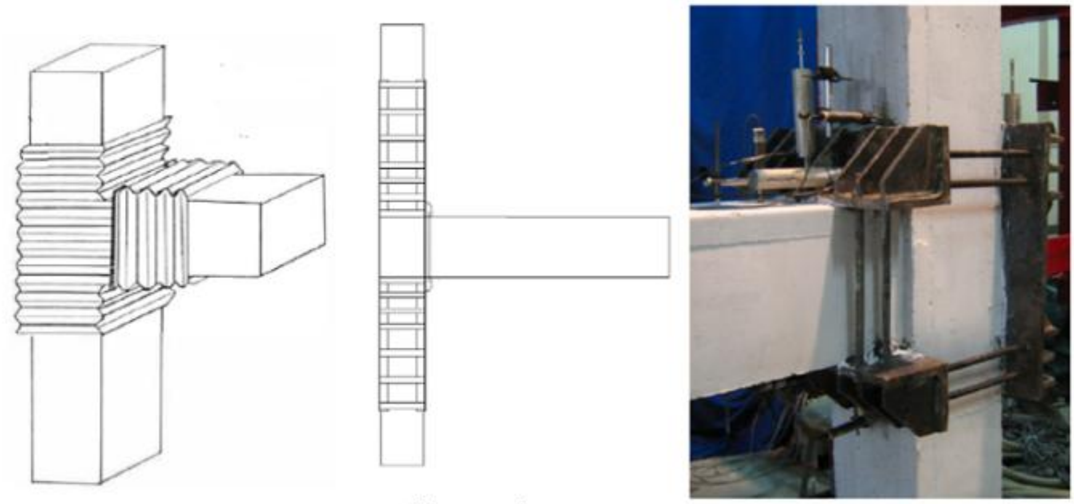

(a): Corrugated steel sheet (b): Steel cages (c): Steel angles

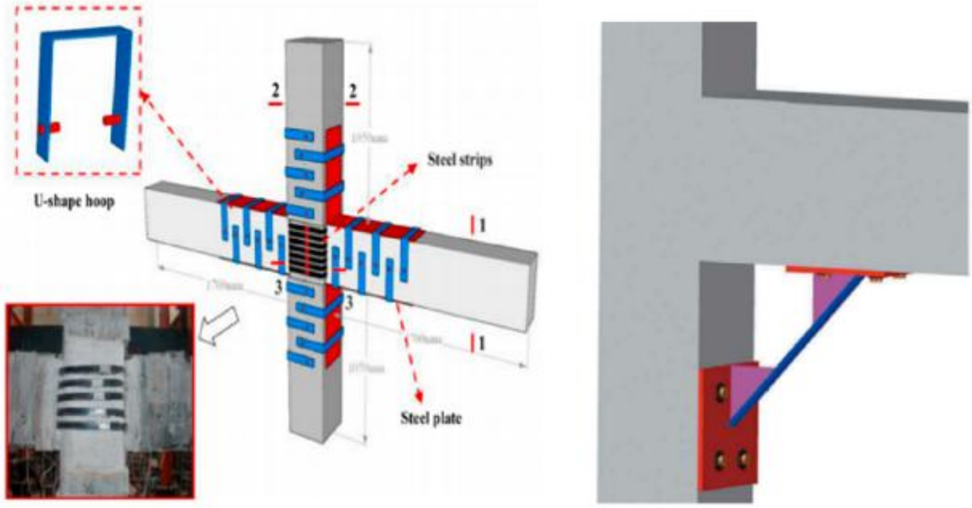

(d): Steel straps (e) Steel haunch

Figure II.7. Various forms of steel jacketing used for structural retrofitting [1].

II.5 FIBER REINFORCED POLYMER (FRP) CONFINEMENT

II.5.1 DEFINITION

Fiber-Reinforced Polymers (FRP) belong to a class of materials referred to as composites. The FRP composites are manufactured by the combination of two or more constituent (phase) materials (Figure II.8) to form an enhanced compound with improved properties that are functionally superior to those of its phases [7]. In general, FRP materials composed of high strength fibers incorporated into a polymer matrix typically made of resin. The fibers act as the primary load-bearing component, offering exceptional tensile strength and rigidity, while the matrix serves to bind and protect the fibers, ensuring load transfer and stability under various conditions. This unique combination results in materials with an impressive strength-to-weight ratio, resistance to corrosion, and adaptability [7].

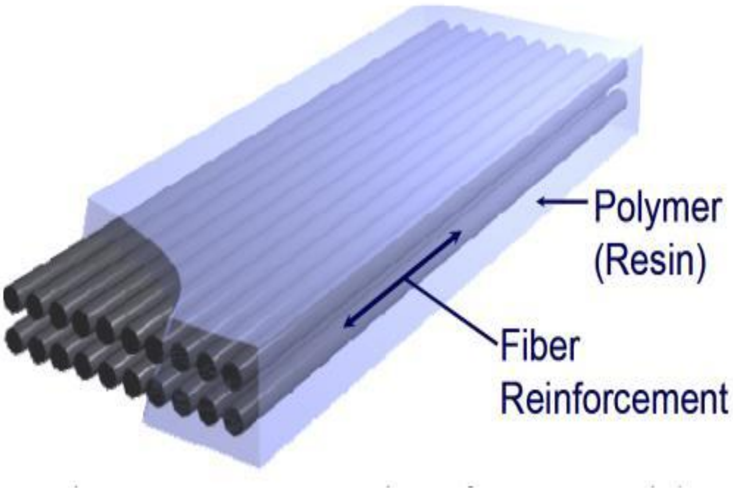

Figure II.8. Components of FRP composites: matrix and fibers.

II.5.2 MATRIX

Polymer matrices, commonly referred to as resins, are classified into two main categories: thermosetting and thermoplastic. Thermosetting resins, including vinyl esters, epoxies, and polyesters, are widely used in composite materials due to their superior chemical resistance, thermal stability, and low creep behavior. These matrices undergo a cross-linking process during curing, forming a rigid structure that cannot be reshaped or dissolved in solvents once set. This characteristic makes them ideal for applications requiring high mechanical performance and durability.

Thermosetting resins are particularly favored in FRP composites due to their strong adhesion to fibers, ease of impregnation, and enhanced structural properties. In contrast, thermoplastics such as polyethylene, polypropylene, polyvinyl chloride (PVC), and polyurethane offer greater flexibility and recyclability but are generally more expensive to produce and highly sensitive to environmental conditions [7].

While matrices can be composed of polymers, metals, or ceramics, polymer-based matrices remain the most commonly used in FRP composites due to their cost-effectiveness and ease of processing. Their role is crucial in transferring stress between fibers, enhancing load distribution, and protecting the composite structure from environmental degradation.

II.5.3 FIBERS

The combination of polymer matrices with reinforcing fibers has led to the development of various types of FRP composites, including carbon FRP (CFRP), glass FRP (GFRP), aramid FRP (AFRP), and basalt FRP (BFRP). More recently, polyethylene naphthalate (PEN) and polyethylene terephthalate (PET) composites have also been introduced.

The mechanical properties of FRP materials vary significantly depending on the type of fiber and polymer matrix used. These variations influence key performance characteristics such as strength and stiffness. Figure II.9 presents a comparison of the stress-strain response curves of typical FRP materials.

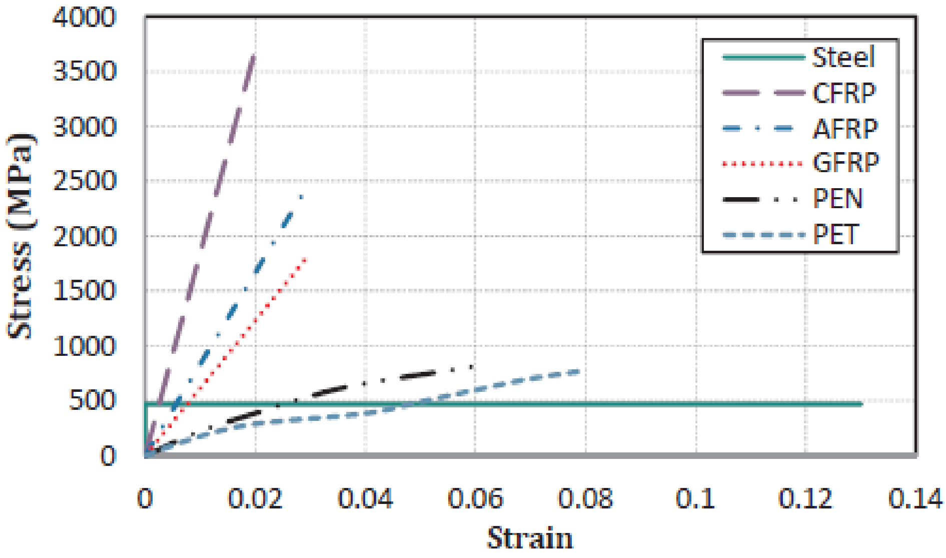

Figure II.9. Tensile stress-strain for steel and different FRP composites [7].

II.5.4 TYPES AND PROPERTIES

FRP composites are available in various forms, including prefabricated laminates, sheets, fabrics, bars, and anchorages. Laminates are rigid elements that offer high in-plane stiffness but are difficult to bend, making them suitable for applications where structural rigidity is required. In contrast, FRP fabrics are flexible and can be supplied in uni- or bi-directional configurations, allowing them to conform to different structural shapes and geometries.

Depending on the intended application, FRP materials can be bonded to structural members to enhance their performance. For instance, fabrics can be adhered to the tension side of beams and slabs to improve flexural capacity. Additionally, wrapping FRP around the joint region and beams helps increase shear resistance, while column confinement enhances both shear and axial load capacity. Figure II.10 illustrates the different types of FRP materials, and Table II-1 presents the typical mechanical properties of different types of FRP composites.

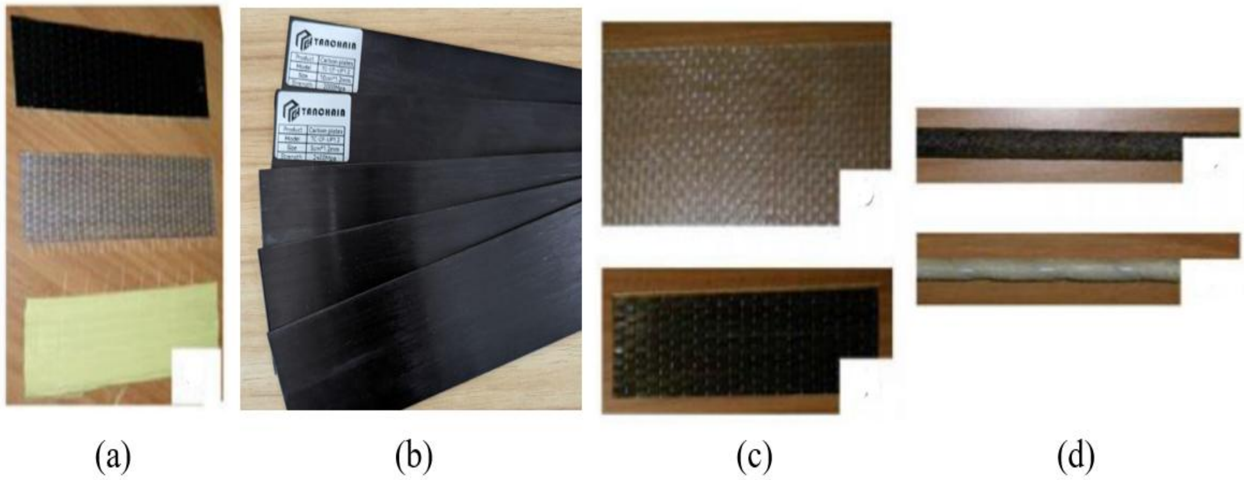

Figure II.10. Different types of FRP composites [8]: (a) Uni-directional carbon, glass, and aramid fiber sheets; (b) CFRP laminate; (c) GFRP and BFRP fabrics; (d) CFRP and GFRP bars.

Table II-1. Mechanical properties of typical commercially available FRP products [7].

FRP Plates				
properties	**Standard modulus carbon FRP**	**High modulus carbon FRP**	**GFRP**	**BFRP**
Fiber volume	65-70	65-70	65-70	68.7
Fiber volume	Unidirectional	Unidirectional	Unidirectional	Unidirectional
Thickness (mm)	1.2-1.9	1.2	1.4-1.9	1.27
Tensile strength (Mpa)	2690-2800	1290	900	1417
Young modulus (GPa)	155-165	300	41	59.2
FRP bars				
properties	**Glass reinforced vinylester**	**Carbon reinforced vinylester**	**AFRP**	**BFRP**
Fiber volume	50-60	50-60	NA	NA
Fiber volume	Unidirectional	Unidirectional	Unidirectional	Unidirectional
Tensile strength (Mpa)	620-690	2070	1448	676
Young modulus (GPa)	41-42	124	70.3	35.2
FRP sheets				
properties	**Standard modulus carbon fiber (two sheets)**	**High modulus carbon fiber (two sheets)**	**Glass fiber**	**Basalt fiber**
Fiber architecture	Unidirectional	Unidirectional	Unidirectional	Unidirectional
Thickness (mm)	0.165-0.330	0.165	0.365	0.17
Tensile strength (Mpa)	3790	3520	1520-3240	2100
Young modulus (GPa)	230	370	72	91
Strain at rupture (%)	1.2-1.5	1.0-1.5	3.5	2.4

II.6 RETROFITTING METHODS USING FRP COMPOSITES

II.6.1 EXTERNALLY BONDED REINFORCEMENT (EBR) METHOD

The EBR method is one of the most widely used techniques for retrofitting or strengthening of RC structural members. This method involves attaching FRP sheets, plates, or fabric directly to the surface of the concrete members using adhesives. Figure II.11 illustrates the schematic representation of the EBR technique, where FRP composites are bonded directly to the surface of the concrete. A notable challenge with this method is the potential for premature debonding of the FRP from the concrete, which can hinder the utilization of the FRP's full tensile capacity. The debonding phenomenon occurs when the induced force in the FRP composite violates the bond capacity of the FRP to concrete [9].

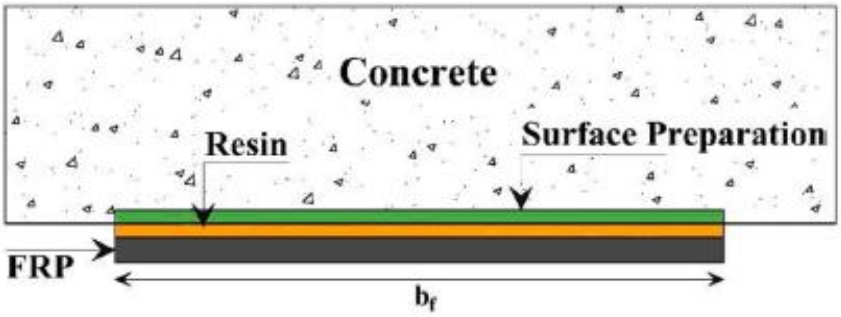

Figure II.11. Schematic representation of externally bonded reinforcement method [9].

The application process of FRP composites typically involves several key steps:

1. Surface preparation, which includes cleaning the concrete to remove contaminants and irregularities.
2. Application of a primer or epoxy layer to enhance adhesion.
3. Placement of FRP sheets, which are bonded with epoxy resin and layered until the desired reinforcement thickness is achieved.

II.6.1.1 REVIEW OF RELATED STUDIES

Several experimental studies have investigated the effectiveness of the EBR technique in retrofitting exterior, non-seismically BCJs. Figure II.12 provides a summary of four primary shear retrofitting approaches, including X-shaped, U-shaped, T-shaped configurations, and retrofits utilizing multiaxial FRP sheets.

The retrofit schemes suggested in most studies can be categorized into the following four groups:

- U-shaped configuration: This is the most commonly adopted confinement scheme for retrofitting exterior joints. It involves wrapping the joint core horizontally using a U-shaped FRP configuration.
- T-shaped configuration: In this approach, FRP sheets are applied in both horizontal and vertical directions within the joint core.
- X-shaped configuration: FRP sheets are applied diagonally along the joint core, aligning with the principal stress directions.
- Multiaxial FRP application: This method involves the use of bi- or quadri-axial FRP sheets in the joint, similar to the X-shaped configuration, to provide multidirectional reinforcement.

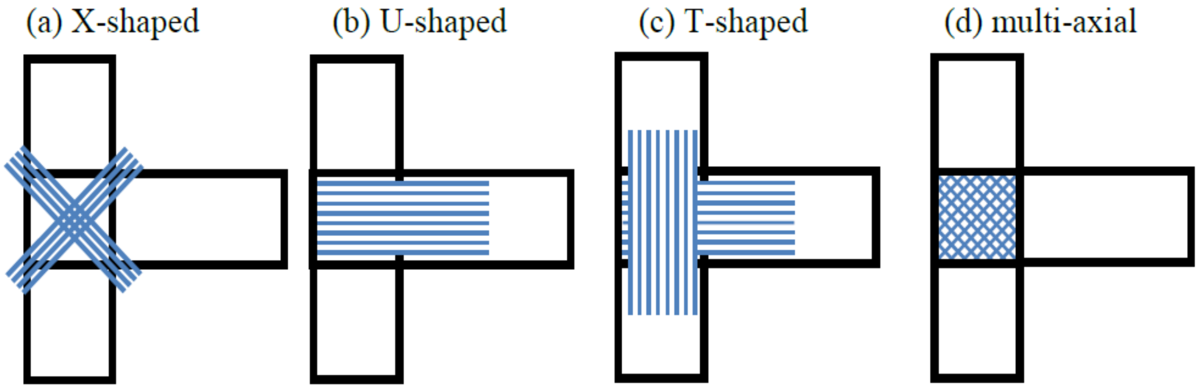

Figure II.12. Schematics of typical joint shear retrofit schemes found in the literature [10].

Ghobarah and Said [11] tested six specimens retrofitted using two different configurations of GFRP composites around the joint core: U-wrap and X-wrap. The results indicated that the U-wrap configuration, applied with a single layer of bi-directional GFRP sheets and anchored with steel plates, effectively delayed shear failure by shifting the plastic hinge away from the joint core to the beam (see Figure II.13 (b)). In contrast, the X-wrap configuration, which lacked steel plate anchorage, experienced premature debonding of the FRP, leading to shear failure within the joint core (Figure II.13 (c)). These findings underscore the critical role of proper anchorage in preventing FRP debonding and enhancing bond performance. The use of steel plate anchorage was shown to mitigate brittle shear failure in the joint and significantly improve its overall structural response under loading.

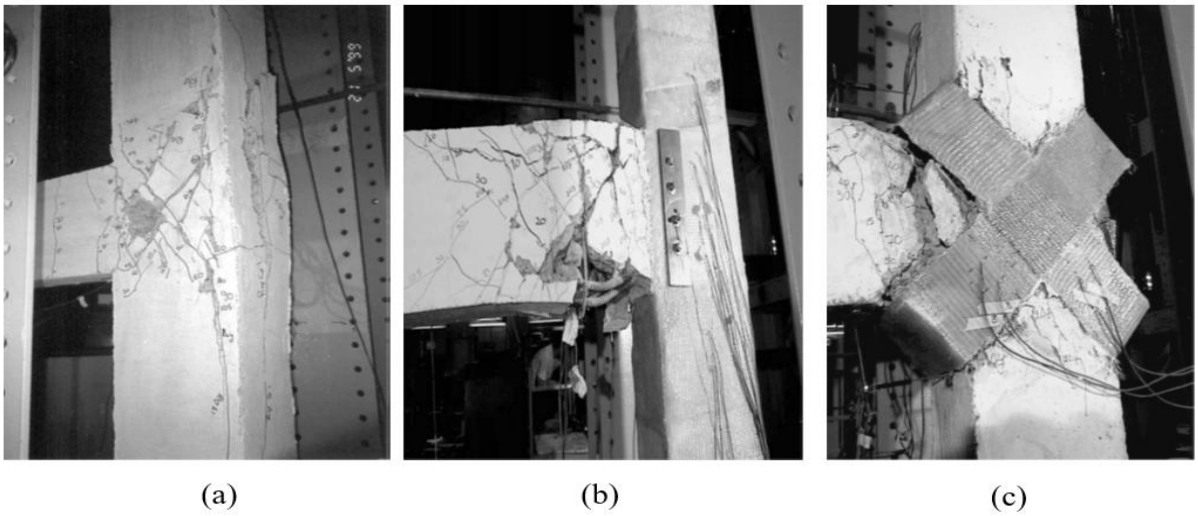

Figure II.13. Failure of specimens tested by Ghobarah and Said [11]; (a) control specimen T1, (b) rehabilitated specimen T2R; (c) rehabilitated specimen T9.

A key observation from most experiments on the EBR technique is the critical need for anchorage. For U-shaped configurations, Ghobarah and Said [11] reported no significant improvement in behavior without proper anchorage. Similarly, Realfonzo et al. [12] observed only a modest strength increase without anchorage, whereas an adequately anchored U-shaped retrofit achieved a substantial strength enhancement of 99%. The importance of anchorage was also emphasized in the study by Antonopoulos and Triantafillou [13], which investigated various T-shaped retrofits with different amounts of vertical and horizontal FRP layers. Their findings indicated that horizontal FRP layers contribute more significantly to the strength of retrofitted joints compared to vertical layers.

When comparing X-shaped retrofits with U-shaped or T-shaped configurations, despite the favorable fiber orientation along the principal stress axis in the X-shaped scheme, studies by Ghobarah and Said [11] and Le-Trung et al. [14] reported a relatively lower strength enhancement. This reduced performance is primarily attributed to debonding issues associated with the X-shaped configuration.

From a practical perspective, retrofits utilizing horizontal and vertical FRP sheets are easier to anchor, as they can be effectively anchored to beams and columns using steel anchors or FRP wrapping techniques.

Table **II-2** presents the strength increases reported in various studies from the literature.

Table II-2. Strength increase achieved through due to shear retrofits.

Author	Main parameter	U-Shaped	T-Shaped	X-Shaped
Ghobarah and Said [11]		+18%		
Antonopoulos and Triantafillou [13]	CFRP		+41%	
	GFRP		+45%	
Le-Trung et al [14]			+32%	+17%
Realfonzo et al [12]	Unanchored	23%		
	anchored	99%		
Karayannis and Sirkelis [15]		+88%		

II.6.2 NEAR SURFACE MOUNTED (NSM) METHOD

The NSM technique involves cutting grooves into the concrete cover of structural elements, such as BCJs, where FRP bars, strips, or rods are then inserted and bonded using a high-strength adhesive. This method has gained widespread use for retrofitting BCJs, as it improves their load-carrying capacity, enhances shear strength, and reduces the risk of debonding, which is a common issue with external FRP applications. Figure II.14 illustrates the schematic representation of the NSM technique, highlighting the groove cutting process and FRP installation.

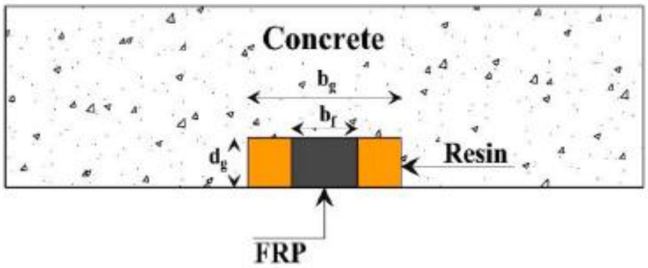

Figure II.14. Schematic representation of near surface mounted technique [9].

Numerous experimental studies have demonstrated the effectiveness of the NSM technique in retrofitting deficient BCJs. For instance, Wang et al. [16] investigated the combined use of EBR-FRP sheets and NSM-FRP strips to retrofit non-seismically designed BCJs. Six BCJ specimens were tested under cyclic loading, including two un-retrofitted specimens: ND (non-seismically designed) and D (seismically designed). The remaining four specimens, designed according to an outdated code, were retrofitted using a combination of EBR and NSM techniques.

- NDSL: Retrofitted solely with the EBR technique in different configurations.
- NDSB and NDSB2: Retrofitted with both EBR and NSM CFRP strips parallel to the beam axis, with NDSB featuring a mechanical anchorage device at the exterior surface of the column.
- NDSC: Retrofitted with both EBR and NSM CFRP strips oriented along the column axis.

The details of the retrofitted joints are illustrated in Figure II.15.

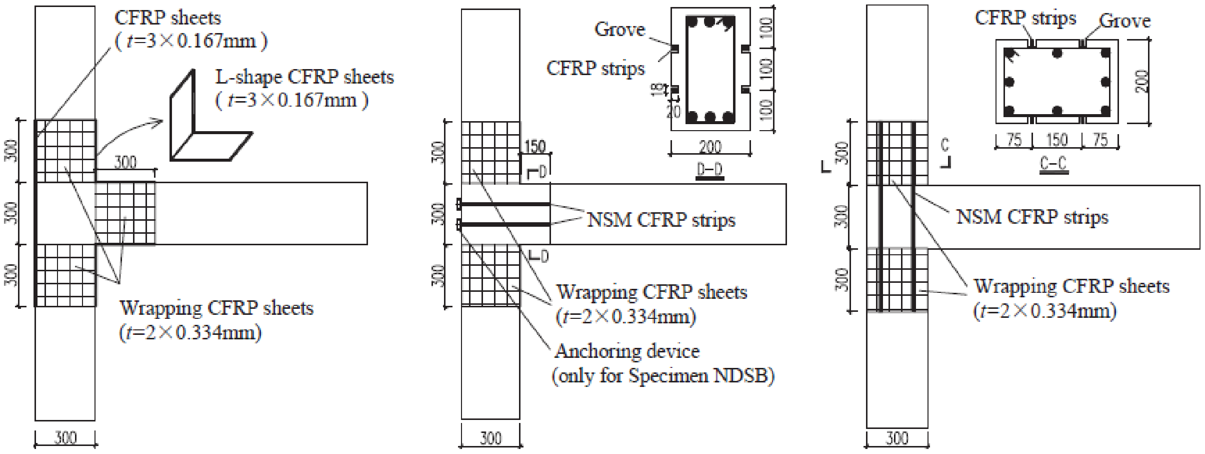

(a) NDSL (b) NDSB & NDSB2 (c) NDSC

Figure II.15. Retrofitting schemes of specimens tested by Wang et al [16].

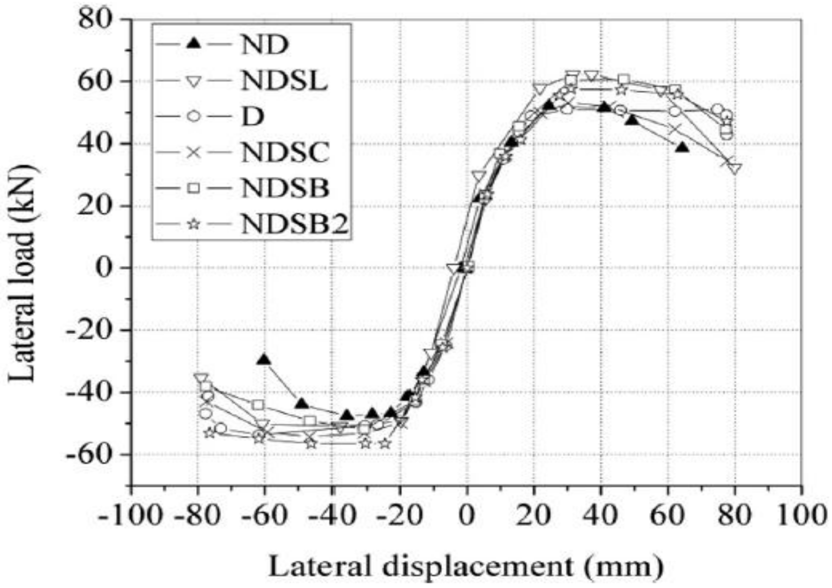

Figure II.16. Load-displacement envelope curves of specimens tested by Wang et al [16].

The envelope curves of the tested specimens are shown in Figure II.16. According to the authors' results, the EBR technique was not effective, as joint shear failure still occurred. In contrast, the use of NSM CFRP strips with anchorage at the beam, combined with CFRP wrapping (Specimens NDSB and NDSB2), proved to be the most effective retrofitting scheme. Additionally, the anchorage of the CFRP strips at the exterior surface of the joint (NDSB) was found to be unnecessary due to the strong bond between the NSM CFRP strips and the surrounding concrete.

Furthermore, placing the NSM CFRP strips along the column axis (NDSC) was significantly less effective than placing them along the beam axis, as joint shear failure still occurred. In conclusion, the results highlight the effectiveness of the NSM technique in retrofitting BCJs, particularly in preventing shear failure and relocating the plastic hinge into the beam, thereby promoting a ductile failure mode.

Zaferani et al. [17] investigated the effectiveness of the NSM technique and the hybrid NSM + EBR method in enhancing the performance of damaged external joints. Eight joint specimens with non-seismic details were tested under three different retrofitting schemes, as illustrated in Figure II.17. Among them, two were left as control specimens, while the remaining six were preloaded, with three subjected to a 1.5% drift and three to a 3% drift. In each case, the preloaded specimens were repaired using the three different retrofitting schemes:

- **Design B**: GFRP bars were inserted into the joint core using the NSM method and extended 600 mm into the beam (Figure II.17 (a)).
- **Design C**: A combination of Design B (NSM GFRP bars) and EBR technique, with three different configurations, as shown in (Figure II.17 (b)).
- **Design D**: Similar to Design C but with additional L-shaped sheets placed on the sides of the beam and column (Figure II.17 (c)).

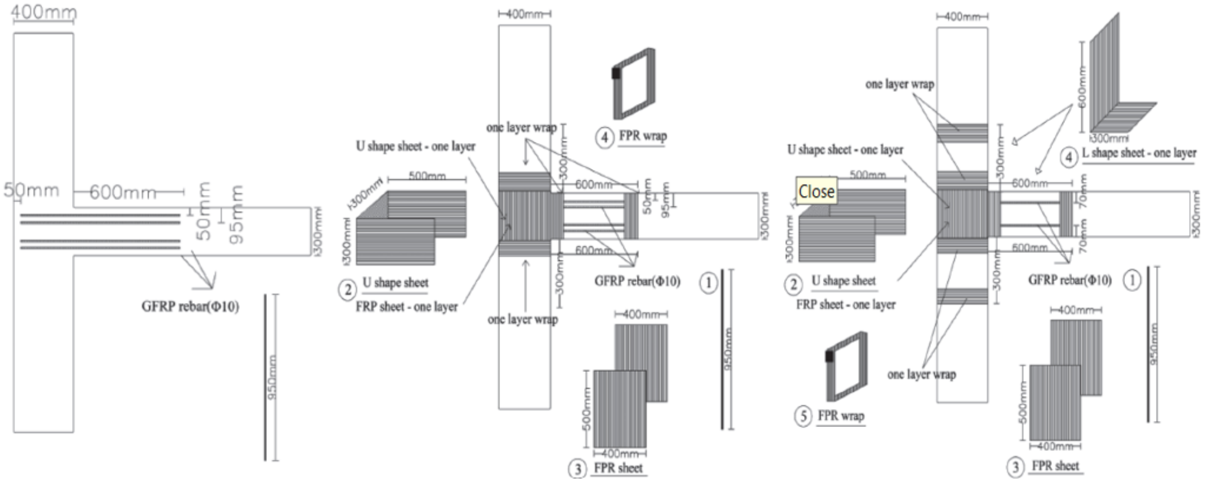

(a) : Design B (b) : Design C (c) : Design D

Figure II.17. Retrofitting schemes of specimens tested by Zaferani et al [17].

Figure II.18 illustrates the envelope curves of the hysteresis responses for the tested joints. The study's findings suggest that hybrid retrofitting techniques not only restore the strength of damaged external joints but can also enhance their capacity beyond that of seismically designed joints. Compared to the NSM approach, these methods provide notable benefits. Although hybrid retrofitting design D incorporated L-shaped sheets at the joint corners, its performance remained comparable to that of retrofitting design C.

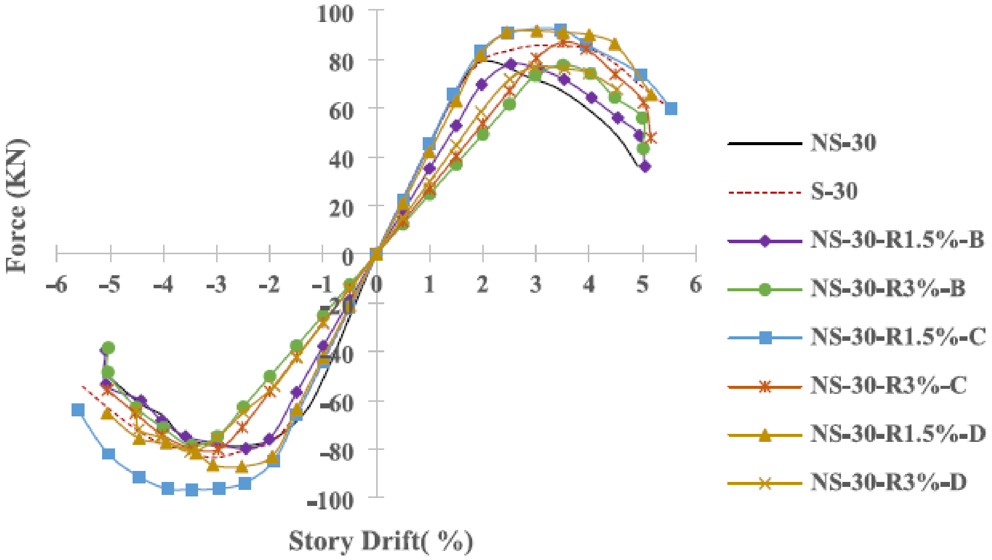

Figure II.18. Load-displacement envelope curves of specimens tested by Zaferani et al [17].

II.6.3 GROOVING METHOD

The EBR method is a widely adopted approach for retrofitting RC structures. However, it faces a significant drawback: premature debonding, which can prevent the FRP composite from achieving its full tensile capacity. This limitation not only compromises the effectiveness of the retrofit but also leads to inefficient use of costly FRP materials. To ensure FRP composites in EBR applications reach their maximum potential, thorough surface preparation is essential to reduce the likelihood of premature debonding.

To address this issue, an innovative method called the Grooving Method (GM) was developed and advocated by researchers at Isfahan University of Technology (IUT) to improve the preparation of concrete substrate surfaces for FRP applications. Originally introduced by Mostofinejad and Mahmoudabadi (2010) [18], this method provides an alternative to conventional surface preparation techniques. The GM involves creating longitudinal grooves in the concrete substrate, which are then filled with epoxy resin. In the first technique of the GM, known as Externally Bonded Reinforcement on Grooves (EBROG), the FRP sheets are subsequently bonded onto the grooved concrete surface without being embedded inside the grooves, as illustrated in Figure II.19 (a). This technique has been extensively studied experimentally, with results indicating that EBROG effectively prevents debonding in FRP-retrofitted specimens, allowing FRP rupture to be the primary failure mode.Building on these advancements, Mostofinejad and Shameli (2013) [19] introduced a second variant, known as Externally Bonded Reinforcement in Grooves (EBRIG), as an alternative to the traditional EBR method. In the EBRIG technique, shown in Figure II.19 (b), the grooves are cut into the concrete and filled with resin, and the FRP sheets are partially embedded inside these grooves before being bonded to the surface.

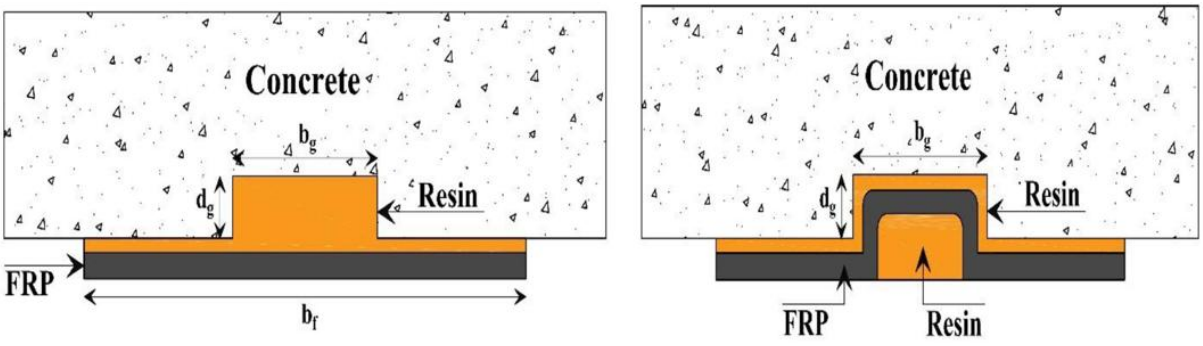

(a) EBROG (b) EBRIG

Figure II.19. Schematic representation of the grooving method [9].

II.7 EXPERIMENTAL TESTING METHODS

In earthquake-prone regions, the lateral load-carrying capacity of structures under seismic loads is commonly evaluated using an amplitude-controlled cyclic load [20]. Two main testing approaches are used to assess the behavior of BCJs under cyclic loading: the displacement-controlled method and the yield displacement-controlled method [1]. These methods evaluate the joint’s strength, stiffness, and ductility but differ in how loads are applied and controlled during testing. In the displacement-controlled method, a lateral displacement is incrementally applied to the BCJ, typically based on the story drift ratio. The drift ratio expresses the lateral displacement at a specific point in the structural component, usually as a percentage of its total height. The measurement of the story drift ratio depends on the location of the applied load, either at the beam or the column end, as illustrated in Figure II.20. For beam-end loading, the drift ratio is calculated using the displacement at the beam end, as shown in Eq. II-1. Conversely, for column-end loading, the drift ratio considers the displacement at the column’s end, as shown in Eq. II-2.

$$\text{Drift Ratio }(\%) = \Delta/L \times 100(\%) \quad \text{II-1}$$

$$\text{Drift Ratio }(\%) = \Delta/H \times 100(\%) \quad \text{II-2}$$

Where:

Δ is lateral displacement under loading;

L is the length of the beam measured from the column face to the loading point;

H is the height of the column from the support to the loading point;

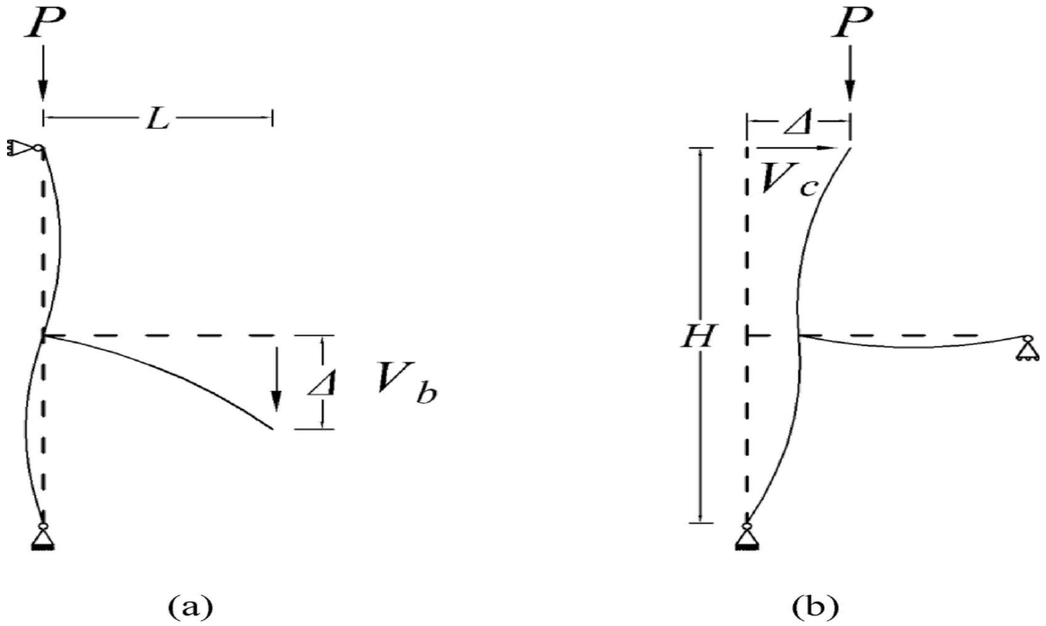

Figure II.20. Drift of the exterior joint under cyclic loading [1]; (a) on beam (b) on column.

The yield displacement-controlled method involves two distinct phases: an initial force-controlled phase followed by a displacement-controlled phase. This is designed two capture the behavior of the joint at different stage of loading, including the yield and post yield behavior. This method is essential for accurately recording the joint's softening beyond the peak load.

- **Phase 1- Force-controlled test:** The test begins with a force-controlled phase, where the load is gradually increased up to 75% of the predicted analytical yield load. This phase allows the joint to experience the initial elastic behavior and approach the yield point without exceeding it.
- **Phase 2-Displacement-controlled test:** After reaching 75% of the predicted yield load, the testing switches to a displacement-controlled method. The displacement is gradually increased from the point of initial yielding (referred to as yield displacement $\varDelta_y$), which corresponds to the first instance of yielding in the beam reinforcement. The displacement is then increased incrementally, which each step being a multiple of the yield displacement (e.g., $1\varDelta_y,\ 2\varDelta_y,\ 3\varDelta_y, etc.$), until the joint fails.

Figure II.21 illustrates the loading protocol applied at the beam end during testing of BCJs, as derived from previous studies utilizing both displacement-controlled and yield displacement-controlled methods. In these protocols, cyclic loads are applied incrementally to evaluate the joint's behavior under simulated seismic conditions.

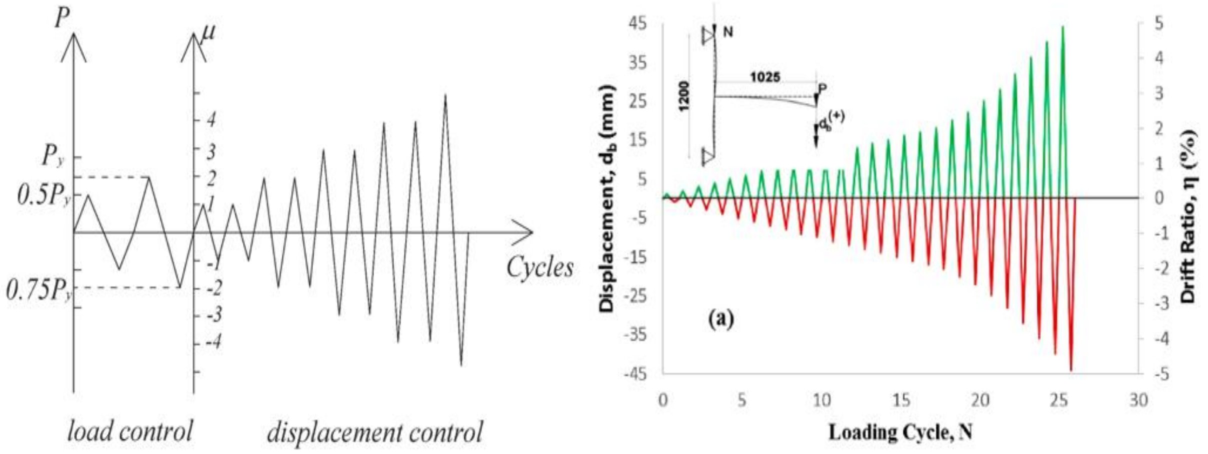

Figure II.21. Example of cyclic loading protocol; (a) force-controlled [16].
(b) Displacement-controlled [21].

II.8 REVIEW OF THE RELATED LITERATURE ON THE GM

An extensive body of research has investigated the EBRIG technique for strengthening beams and columns, as reviewed in Refrence [9]. However, to the best of the authors' knowledge, no studies have explored the application of the EBRIG technique for retrofitting BCJs. Therefore, this section focuses solely on the retrofitting of BCJs using the EBROG technique.

A total of 22 BCJs specimens were examined across four independent studies reviewed in this section. Figures. II-23 to II-25 show the schematic plans of the retrofitted specimens and the retrofitting details.

II.8.1 APPLICATION OF THE EBROG

A brief description on the application of the EBROG technique can be found in References [22, 23]. In all tests, the grooves created were 10 mm deep and 10 mm wide, with a 30 mm free space. An angle grinder machine was used to cut the grooves with the specified dimensions in the areas where the FRP sheets were to be installed. The grooves were only in the concrete cover, ensuring no intersection with the steel reinforcement due to the shallow depth of the grooves.

After cutting the grooves:

1. They were filled with an appropriate epoxy resin.

2. A layer of epoxy resin was applied to the concrete substrate.
3. The FRP sheets were impregnated with the same epoxy.
4. Once the FRP fabric was bonded onto the concrete substrate, sufficient suturing resin was applied again to achieve full saturation.

II.8.2 APPLICATION OF FRP FAN ANCHORS

In some of specimens, the FRP composites were anchored in the concrete substrate using hand-made FRP fan anchors to investigates the effects of FRP composites end anchorage. The procedure used to make the FRP fan anchors is as follows:

1. Cutting the FRP sheets to the required lengths.
2. An adequate amount of epoxy resin was added in the middle part of the sheet, and then the sheets was rolled around a metal rod.
3. Holes was made in the concrete surface and then filled with epoxy into which FRP fans were inserted. The metal rod was pulled out of the FRP fan.
4. The two spikes at the end of the FRP fan remaining outside the concrete surface were impregnated with the resin and fanned out on the original FRP sheets.

Figure II.22 shows an example on the application of hand-made FRP fan to anchor the external FRP composites.

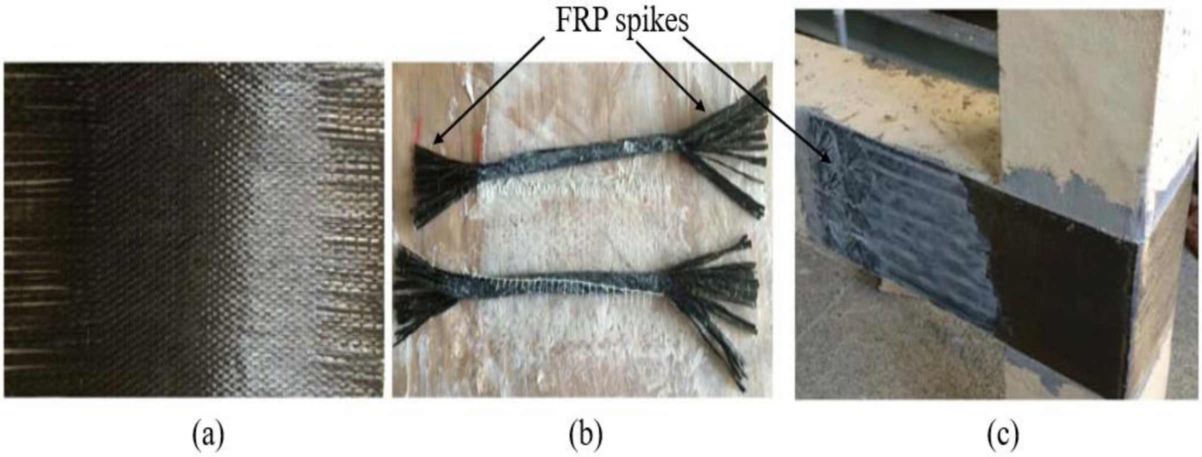

Figure II.22. Application of hand-made FRP fan [24]: (a) CFRP sheets; (b) FRP fan; (c) Anchorage the external CFRP composites.

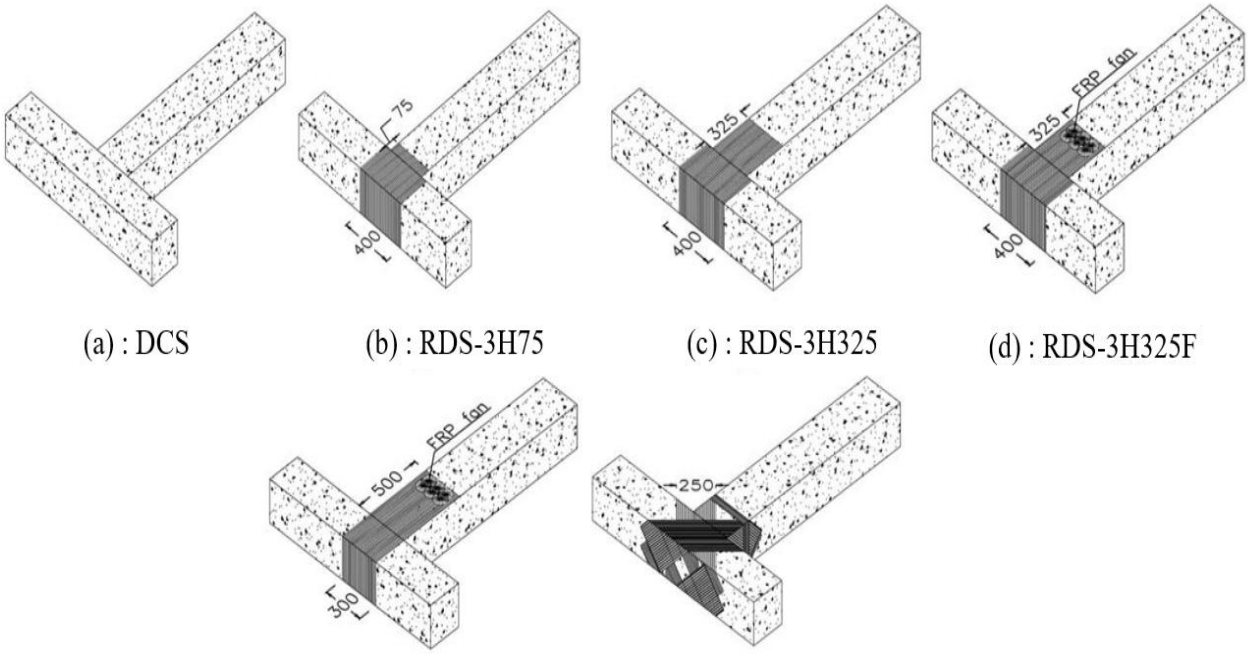

(a) : DCS (b) : RDS-3H75 (c) : RDS-3H325 (d) : RDS-3H325F

(e) : RDS-4H500F (f) : RDS-1X250

Figure II.23. Retrofitting schemes of specimens tested by Mostofinejad and Akhlaghi [24].

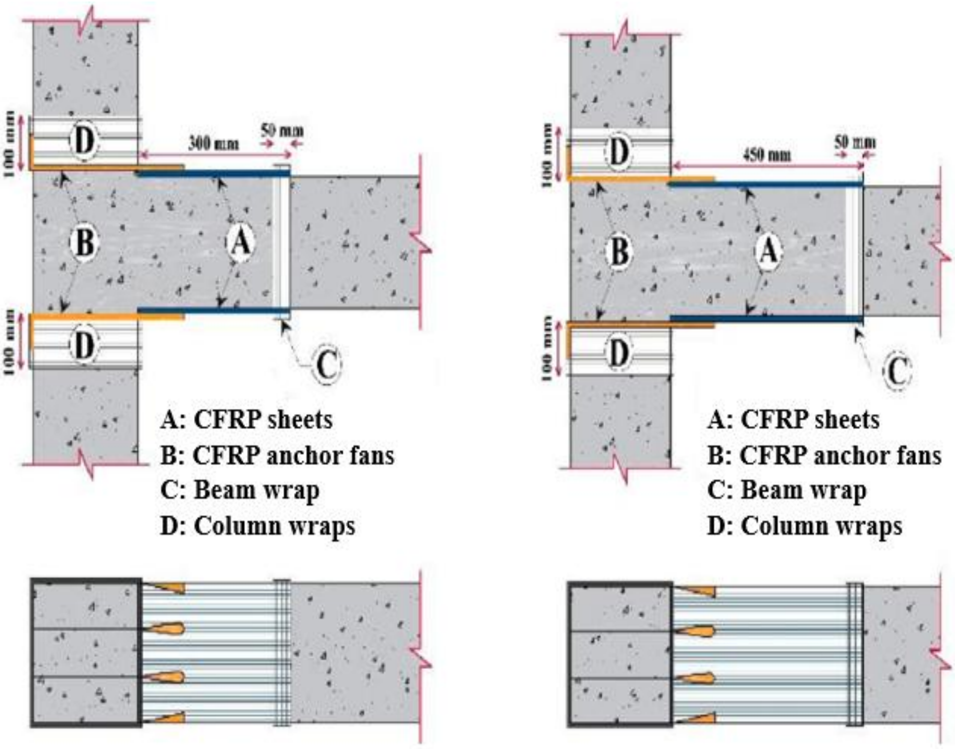

(a) : RS-1H300 (b) : RS-2H450I

Figure II.24. Retrofitting schemes of specimens tested by Mostofinejad and Akhlaghi [25].

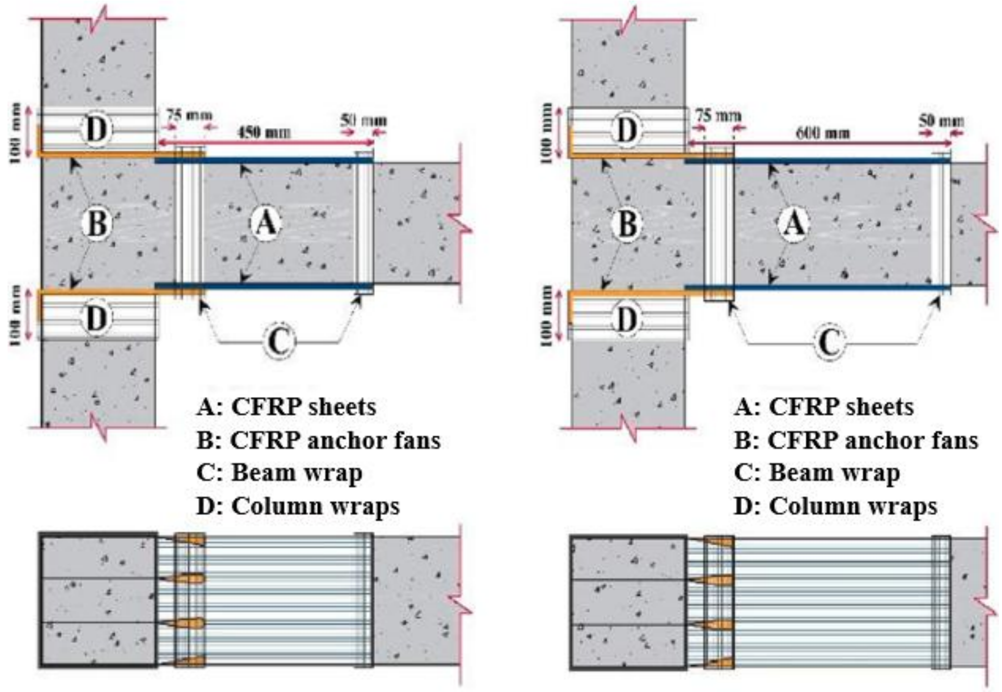

(c) : RS-2H450II (d) : RS-3H600I,II

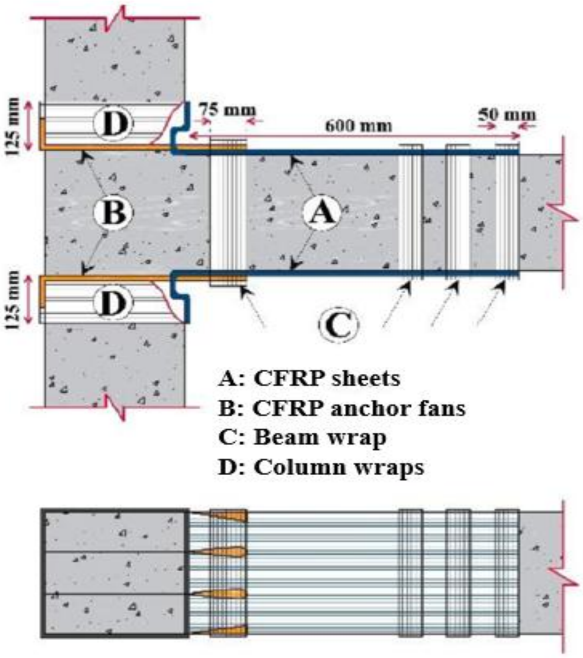

(e) : RS-2L600

Figure II.24. Continued [25].

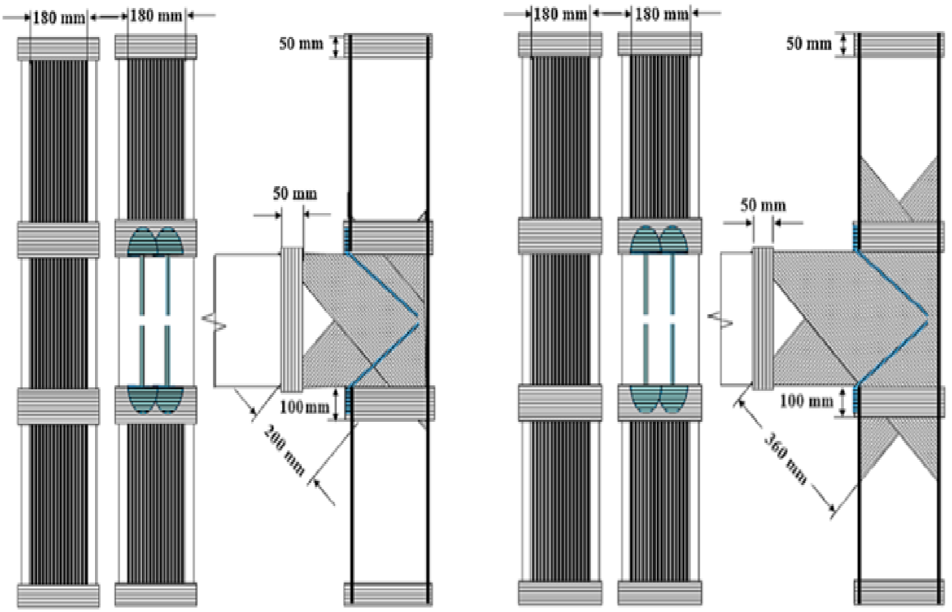

(a) : RS-1V-1X (b) : RS-1V-2X

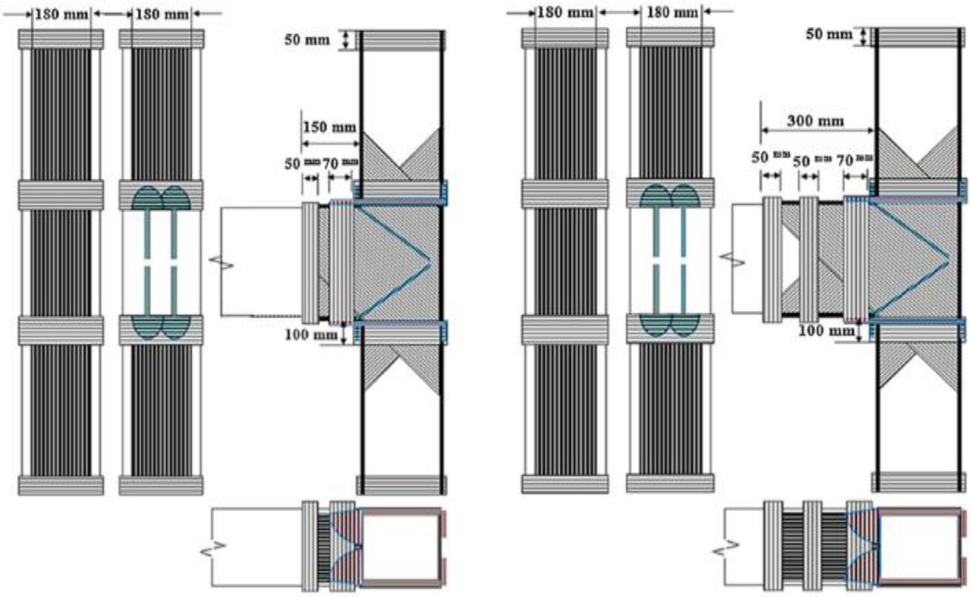

(c) : RS-1V-2X-2H.I (d) : RS-1V-2X-2H-2II

Figure II.25. Retrofitting schemes of specimens tested by Ilia and Mostofinejad [26].

II.8.3 RELATED STUDIES REVIEW

Mostofinejad and Akhlaghi [24] explored the effectiveness of the EBROG method in shear retrofitting of seismically-deficient BCJs which lacked shear reinforcement in the joint core under cyclic loading. They tested six specimens, including a control (DCS) and five CFRP-retrofitted models with varied sheet configurations (Figure II.23). The retrofitted specimens were named using templates “RDS-nHlF” and “RDS-nXl “. n stand the number of FRP layers; H and X stand to the retrofitting patterns with U and X-shaped respectively; L is length of CFRP sheets; and F denotes the presence of FRP fans. Most of the retrofitted samples used U-shaped CFRP sheets around the joint area with different lengths, while one (RDS-1X250) featured an X-shaped sheet pattern. For additional reinforcement, some sheets were secured with FRP fan anchors. The load-displacement envelope hysteretic curves are shown in Figure II.26.

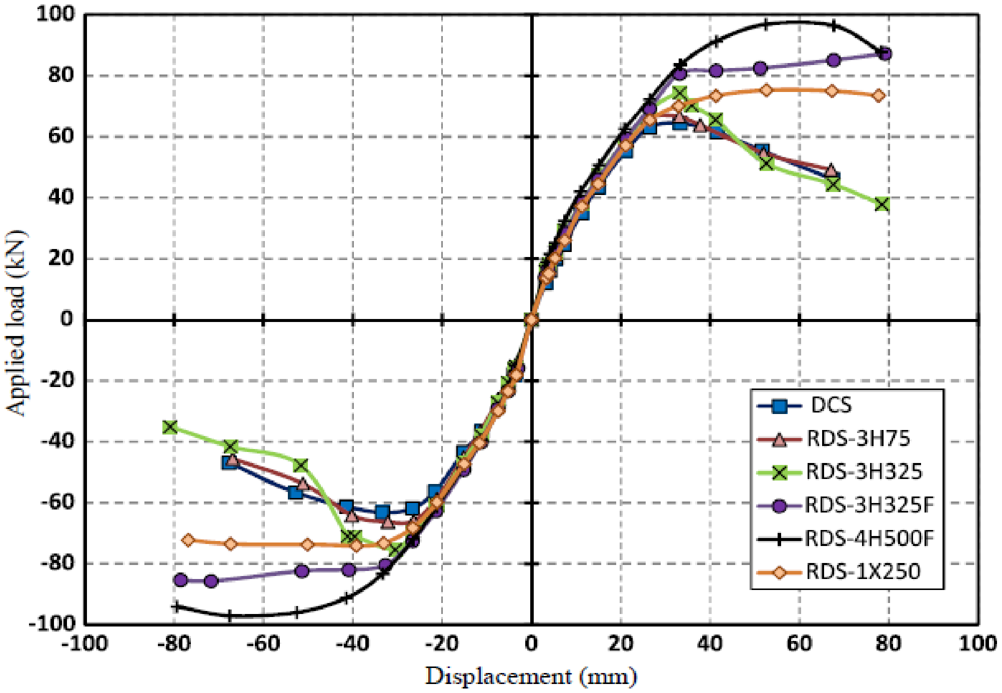

Figure II.26. Load-displacement envelope curves of specimens tested by Mostofinejad and Akhlaghi [24].

The results indicated that the control specimen (DCS) failed in brittle shear failure with substantial X-shaped cracks observed in the panel zone due the absence of shear reinforcement in this zone. The maximum recorded load for this specimen was 63.8 kN. In contract, the RDS-3H75 and RDS-3H325 joints exhibited maximum load increases of 4.2% and 17.4% respectively, compared to the DCS joint. A substantial X-shaped cracks in the panel zone was also observed in retrofitted specimens RDS-3H75 and RDS-3H325 due to the delamination of the CFRP composites with pronounced reduction in strength. Afterward, the specimens displayed behavior nearly identical to that of the control [24].

The ends of the CFRP composites were anchored using FRP fans in the RDS-3H325F and RDS-4H500F joints, resulting in peak load increases of 35.6% and 52.0%, respectively, compared to the DCS joint. These specimens exhibited nearly identical behavior. The results demonstrated the superior performance of the EBROG in preventing CFRP delamination. Additionally, the FRP fan anchorage successfully prevented the splitting failure of the concrete cover. Instead of shear failure in the panel zone, the observed failure mode was a flexural plastic hinge in the beam. Finally, the RDS-1X250 specimen exhibited a peak load increase of 17% compared to the DCS joint. It was also observed that no significant delamination occurred in the panel zone of this specimen, further confirming the effectiveness of the EBROG technique in eliminating the delamination phenomenon.

In another study, Mostofinejad and Akhlaghi [25] investigated the behavior of code-compliant exterior BCJs strengthened with CFRP composites through EBROG combined with FRP fan anchors, focusing on beam flexural strengthening in areas prone to plastic deformation. In flexural strengthening, CFRP composites are most effective when installed on the top and bottom sides of the beam. A total of seven specimens, comprising one control specimen (CS) and six strengthened specimens, were tested under reverse cyclic loading. The strengthened specimens were designated as RS-nHl and RS-nLl, where n denotes the number of CFRP layers. Lowercase l indicates the length of the longitudinal CFRP sheets, while uppercase L represents the L-shaped configuration of the longitudinal CFRP composites. and H denotes to the longitudinal CFRP composites

In each specimen, four FRP fans were used to anchor the longitudinal CFRP composites at the beam-column interface, with different volume fractions. To prevent concrete cover separation, 50-mm-wide CFRP wraps were applied at the cut-off point of the longitudinal CFRP composites. Additionally, CFRP wraps were applied at the column interface as additional anchorage for the longitudinal composites in some specimens. The strengthening patterns of the specimens are illustrated in Figure II.24.

The load-displacement hysteretic envelopes for the tested specimens are depicted in Figure II.27. The non-strengthened CS specimen achieved a maximum load of 48.4 kN, with the flexural plastic hinge forming at the beam’s column face.

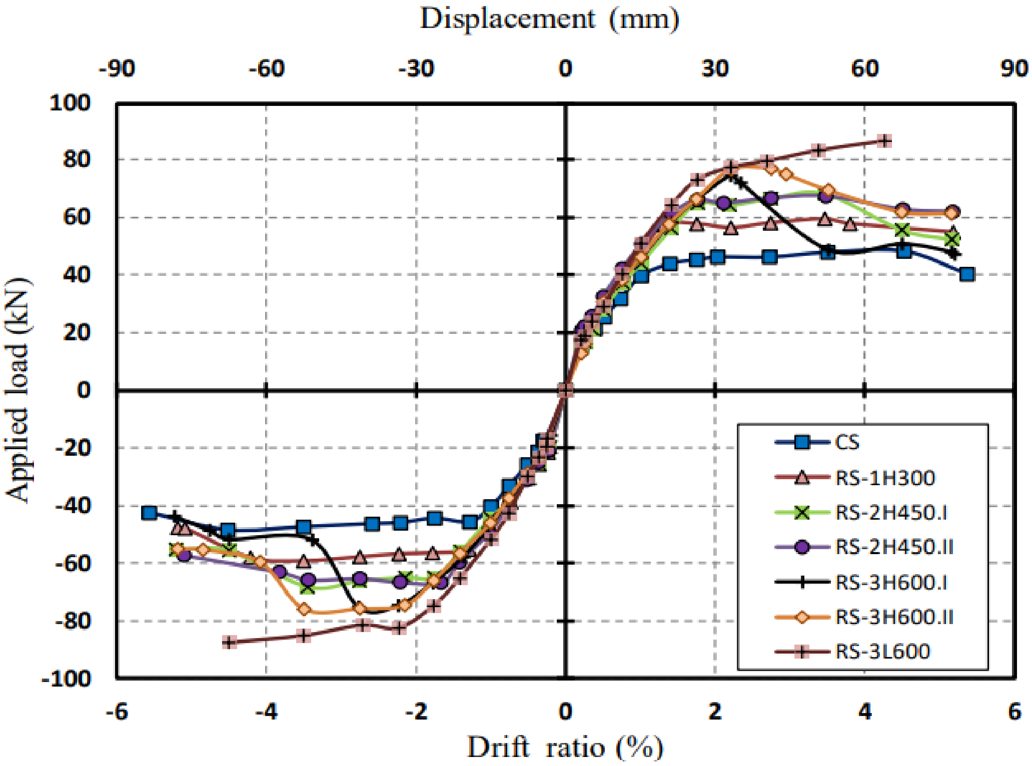

Figure II.27. Load-displacement envelope curves of specimens tested by Mostofinejad and Akhlaghi [25].

In the RS-1H300 joint, the flexural plastic hinge was shifted after the cut-off point (termination point) of the FRP composites along the beam. resulting in a 32.7% increase in peak load compared to CS. Concrete cover separation was observed at the last stage of loading due the single layer of CFRP wraps applied at the cut-off point of the longitudinal CFRP composites. By increasing the number and the length of the CFRP layers in the RS-2H450.I specimen, the plastic hinge shifted back to the same position as in CS specimen as a result of weaknesses of the FRP fans anchors. the maximum load for this specimen was increased by 41.1%. specimen RS-2H450II was identical to RS-2H450.I one except that three layers of CFRP wraps were added on the FRP fans anchors. the flexural beam plastic hinge near to the column face was avoided for this specimen and relocated at the cut-off point of the longitudinal CFRP composites due the improved anchorage. This specimen recorded 38.4% gain in capacity compared to CS one. Specimen RS-3H600II was identical to RS-3H600I, except for an increase in the fans anchor fiber area in the RS-3H600II specimen. The maximum recorded loads were increased compared to CS by 58.1% and 54.7% respectively. RS-3H600I failed with the plastic hinge in beam at the column interface combined with CFRP fans rupture due to the increased length of the longitudinal CFRP composites. by increasing the fans anchor area for specimen RS-3H600II the plastic hinge was relocated away from the column interface in strengthened part of the beam. To address the drawbacks observed in previous specimens, such as the formation of the plastic hinge in the beam near the column face or within the strengthened portion of the beam, as well as concrete cover separation at the cut-off point of the longitudinal CFRP composites, the RS-3L600 specimen was specifically designed. For this specimen the hinge was completely relocated in the non-strengthened part of the beam and the peak load was increased by 79.9% compared to CS specimen.

Furthermore, Ilia and Mostofinejad [26] conducted experimental research to evaluate the influence of the EBROG technique in retrofitting seismically deficient exterior BCJs. For this purpose, five half-scale specimens were tested under reversed cyclic loading. The specimens were designed with inadequate shear reinforcement in the joint region and followed the concept of a strong beam-weak column, with a column-to-beam flexural capacity ratio of around 0.85, representing a weak column design. The control specimen was named CS, while the four retrofitted specimens were labeled with the code names RS-nV-mX-kH. Here, n represents the number of vertical CFRP layers installed on the two opposite sides of the column. And the letter m denotes to the number of X-shaped CFRP layers installed in the joint core, rotated at an inclination of 45° relative to the horizontal axis of the beam as well as grooves. The latter k indicates the number of the longitudinal CFRP layers used to strengthen the beam on their top and bottom faces. In each sample, two FRP fan anchors with single spike were inserted into diagonal holes and fanned out on the vertical layers of the column as illustrated in Figure II.25. Additionally, two FRP fans with two spikes each were used to anchor the longitudinal layers of the beam at the beam-column interface. And some CFRP wraps were used as additional anchors for the different configurations. All the retrofitting details are illustrated in Figure II.25.

The envelope curves are shown in Figure II.28. The control specimen (CS) reached a maximum load of 28.4 kN. This specimen failed due to joint shear failure and flexural hinging in the column, as expected by the authors [26]. For specimen RS-1V-1X, no flexural plastic hinge occurred in the column. The failure pattern for this specimen was characterized by the rupture of the FRP X-shaped composite, followed by shear failure in the joint core. The maximum load was enhanced by 50.9% compared to the CS. No debonding of the CFRP was observed, attributed to the strong bond achieved through the EBROG technique.

In specimen RS-1V-2X, the number and width of X-shaped layers were increased, which led to a higher load-carrying capacity compared to the CS joint, with an increase of approximately 64.1%. The failure mode for this specimen also occurred in the X-shaped layers, resulting in brittle joint shear failure.

To prevent the undesired failure modes observed in the previous specimens, RS-1V-2X-2H.I and RS-1V-2X-2H.II were designed. These specimens were reinforced with additional longitudinal CFRP layers on the top and bottom sides of the beam, with varying numbers and widths of layers. This strategy effectively prevented the flexural cracks in the beam near the column face, which were previously transferred to the joint core. Consequently, in these specimens, the plastic hinge was fully transferred to the termination points of the longitudinal CFRP composites. This resulted in further load-carrying capacity gains of 57.1% and 73.3% compared to the CS joint, respectively. Additionally, no significant reduction in strength was observed during the final loading stages, in contrast to the behavior of other retrofitted specimens, as illustrated in Figure II.28.

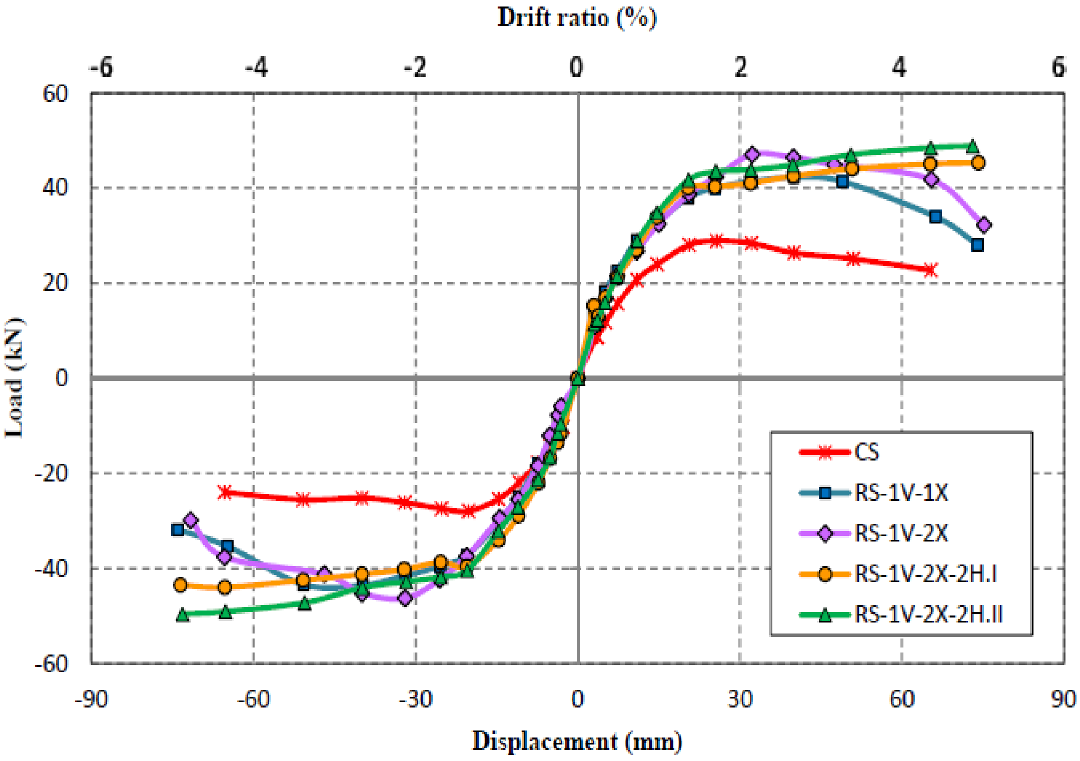

Figure II.28. Load-displacement envelope curves of specimens tested by Ilia and Mostofinejad [26].

Davodikia et al [27] conducted a comparative study on retrofitting seismically deficient exterior BJs using the conventional EBR technique and the innovative EBROG method. Four specimens were tested under reversed cyclic loading. Two specimens, NS and S, served as controls: the NS specimen lacked seismic details, while the S specimen was designed according to current seismic regulations to include seismic details. The other two specimens, R1NS and R2NS, were designed without seismic details and retrofitted with CFRP composites using the EBR and

EBROG techniques, respectively. A detailed description of the experimental setup is provided in the next chapter to validate the numerical analysis.

The envelope curves of the tested specimens are shown in Figure II.29. The average peak loads for the NS, S, R1NS, and R2NS specimens were 45.80, 43.33, 54.18, and 54.73 kN, respectively. The NS specimen exhibited brittle failure, with damage concentrated mainly in the joint core area and severe diagonal shear cracks. The failure was attributed to insufficient joint shear strength, leading to a significant drop in load-carrying capacity during the final loading stages. In contrast, the S specimen demonstrated ductile behavior, with the plastic hinge forming in the beam rather than in the joint core. No significant reduction in load-carrying capacity was observed.

The R1NS specimen, retrofitted using the EBR technique, showed an improvement in load-carrying capacity compared to NS. However, the behavior remained brittle, with shear failure in the joint region and a noticeable reduction in post-peak strength. This was primarily due to the debonding of CFRP from the concrete surface, a common challenge with the EBR method. Conversely, the R2NS specimen, retrofitted using the EBROG technique, exhibited ductile behavior. The strong adhesion between CFRP and concrete prevented shear failure in the joint core, relocating the plastic hinge to the beam. This resulted in sustained strength without a significant drop in load-carrying capacity.

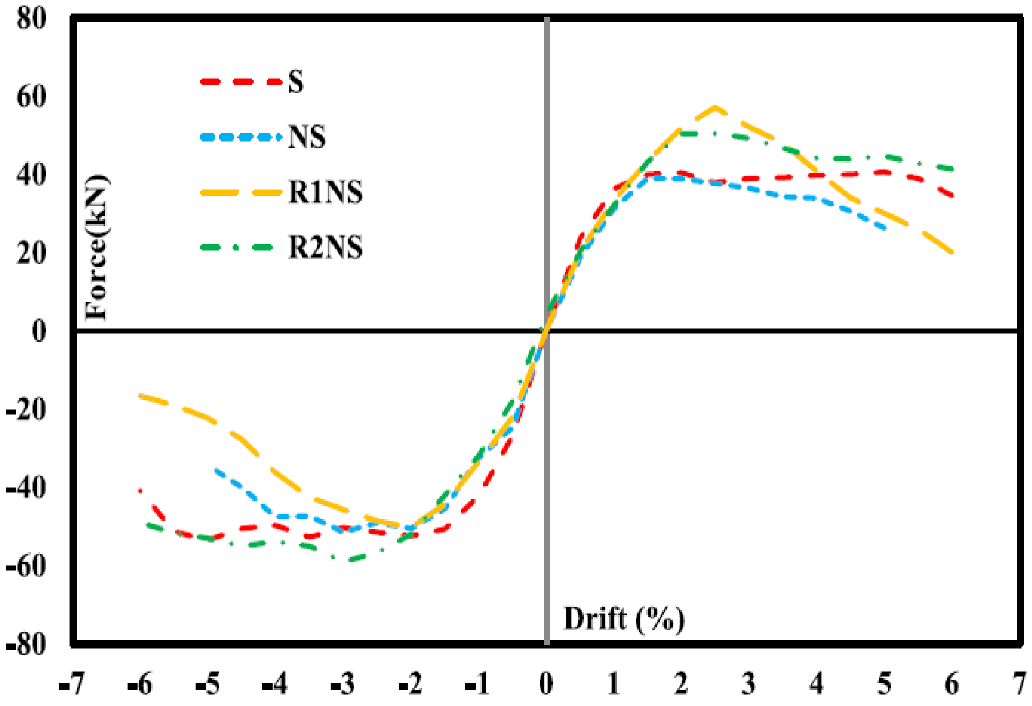

Figure II.29. Load-displacement envelope curves of specimens tested by Davodikia et al [27].

II.9 NUMERICAL MODELLING

The finite element method (FEM) is widely recognized as an effective computational approach for analyzing various engineering challenges, especially in evaluating the deformation and stress responses of structural components. Continuous advancements in computer technology and computer-aided design (CAD) systems have made it possible to model complex structural behaviors with greater accuracy and efficiency. This progress allows engineers to explore multiple design alternatives through simulation. Numerous finite element software programs, including Vector2, DIANA, ANSYS, ATHENA, and ABAQUS, have been developed to simplify model creation and analysis.

This section provides an in-depth review of existing numerical models designed to simulate the performance of exterior BCJs retrofitted with CFRP composites. Special attention is given to modeling strategies, material behavior models, failure mechanisms, validation processes, and the parameters examined in these simulations.

II.9.1 REVIEW OF PREVIOUS MODELS

Saad A.G. et al. [28] conducted a two-dimensional FE analysis using ABAQUS to examine the shear behaviour of exterior BCJs retrofitted with CFRP composites. Their numerical investigation was validated against experimental results from four retrofitted specimens using EBR technique, specifically CS, HSG, NS5, and NS1R, all subjected to cyclic loading. A monotonic loading approach was adopted in the FE analysis as a reasonable approximation. The concrete was simulated using the CDP model, while the CFRP was treated as a linear isotropic elastic material. Steel reinforcement was modelled with a bilinear elastic–plastic behaviour. To realistically capture the debonding mechanism, an adhesive interface layer was introduced between the CFRP sheets and the concrete substrate, and a bond-slip relationship was implemented to represent the CFRP–concrete interaction. An example of the validation for the NS5 specimen is shown in Figure II.30, highlighting the correlation of load–displacement behaviour and failure patterns. Based on the validated FE model, a parametric study was carried out to assess the influence of various parameters such as the column-to-beam flexural strength ratio, concrete compressive strength, and axial load on the performance of CFRP-retrofitted joints. Furthermore, the authors proposed new design formulations to predict the shear capacity of retrofitted joints, incorporating the contribution of the CFRP–concrete bond interface. These equations were substantiated through both experimental data and numerical simulations.

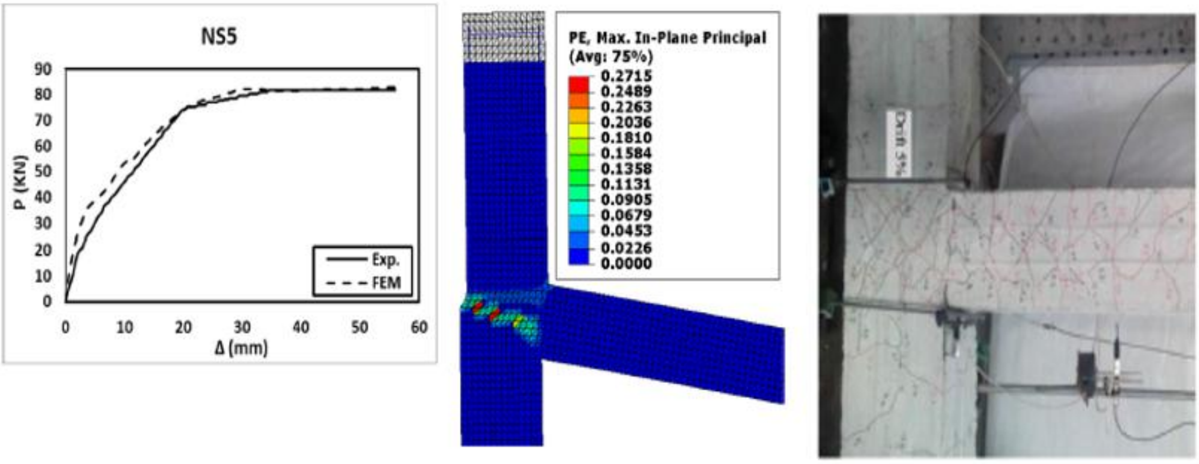

Figure II.30. Numerical validation of the NS5 specimen modeled by Saad. A. G et al [28].

Baji et al [29] conducted a FE investigation using the VecTor2 program to evaluate the effectiveness of retrofitting BCJs with EBR using FRP composites. Two retrofitting configurations were examined: web-bonded and flange-bonded schemes. The numerical model was first validated against a series of experimental tests conducted in their study, as well as additional tests selected from the literature. The FE results were compared with experimental findings in terms of load-displacement curves, failure modes, and plastic hinge locations.

Figure II.31 illustrates the material constitutive models used for different components in the numerical model. Concrete in compression was modeled in two phases: the pre-peak behavior was defined using the Hognestad model [30], while the post-peak response was captured using the modified Kent and Park model [31]. In contrast, the modified Bentz model [32] was employed to represent the tension stiffening of concrete. The steel reinforcement was modeled with a bilinear behavior, whereas the FRP material was assumed to follow a linear elastic model.

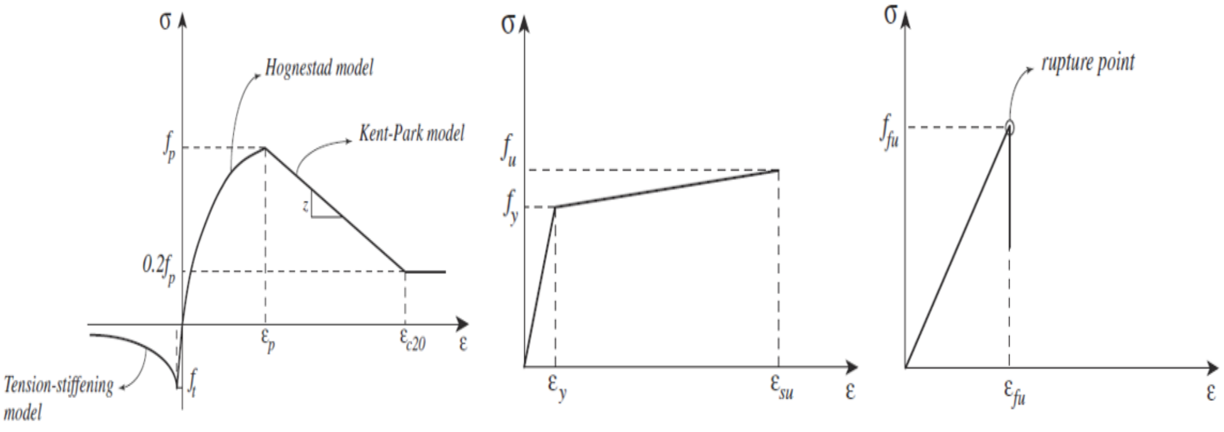

(a) Concrete model (b) Steel model (c) FRP model

Figure II.31. Material models used in the numerical analysis with VecTor2 [29].

For simplicity, the authors assumed a perfect bond between the FRP and concrete, as no significant debonding was observed in the experimental study. Figure II.32 presents the validation of specimen HSG, showing the load-displacement curve and failure mode. According to the authors' findings, both web-bonded and flange-bonded CFRP retrofitting schemes effectively relocated the plastic hinge zone away from the column face, shifting it further into the beam. Additionally, the numerical model accurately predicted the plastic hinge relocation, closely matching the experimental observations.

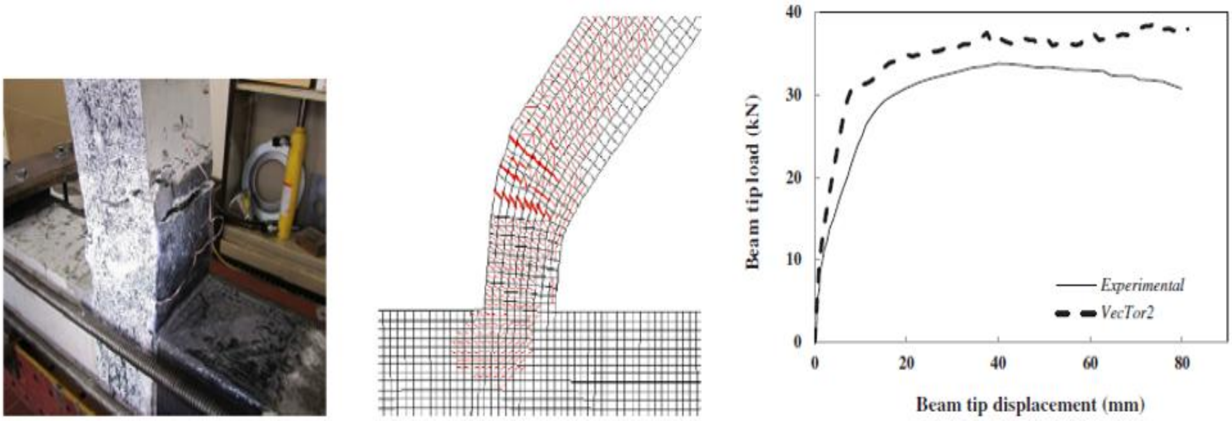

Figure II.32. Numerical validation of the HSG specimen modeled by Baji et al [29].

In another numerical study, Abu Tahnat YB et al [33] explored the influence of CFRP wrapping around the beam member of exterior BCJs, considering various structural parameters. These parameters included the beam-to-column relative inertia, steel reinforcement content in the joint core, transverse reinforcement in the beam, and the role of CFRP wrapping. The CFRP layout was modeled as a single-layer wrap around the beam member in all models, as illustrated in Figure II.33.

The numerical parametric study was conducted after validating the FE model against eight experimental specimens. The analysis was performed using the ABAQUS software, with the Concrete Damage Plasticity (CDP) model employed to simulate the nonlinear behavior of concrete. The steel reinforcement was represented with a bilinear stress-strain relationship, while CFRP was modeled as an orthotropic linear elastic material. To account for potential debonding and slip at the CFRP-concrete interface, a cohesive contact approach was implemented, requiring both separation-traction and force-slip constitutive laws. An example validation of specimen J0, in terms of load-displacement behavior and failure mode, is presented in Figure II.34.

According to the authors' findings, CFRP wrapping around the beam effectively transformed brittle failure modes into ductile ones. However, its influence was limited in cases where the beam was already well-confined by transverse reinforcement or when failure occurred within the joint core rather than in the beam. On the other hand, the CFRP wrapping significantly improved the performance of models exhibiting shear-dominated beam failure.

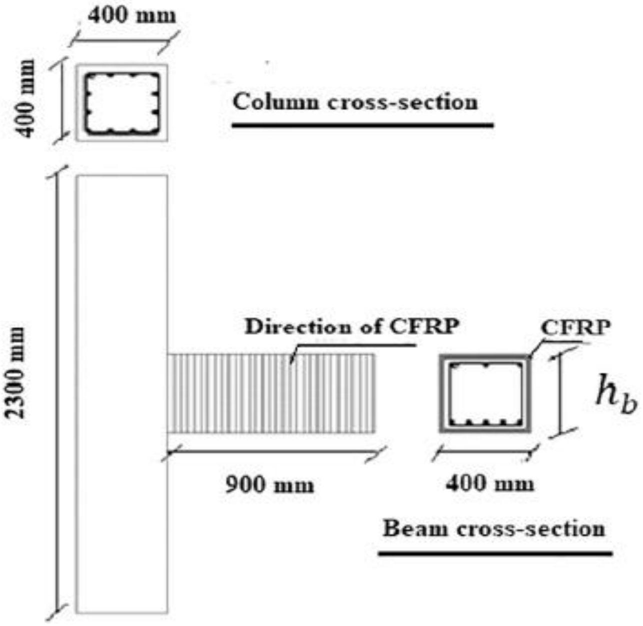

Figure II.33. Wrapping arrangement of CFRP studied by Abu Tahnat YB at al [33].

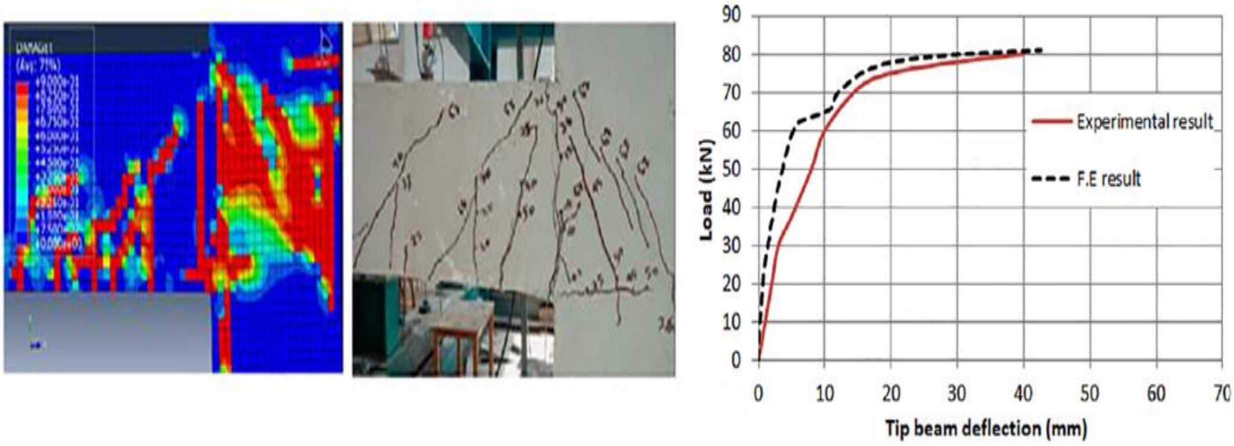

Figure II.34. Numerical validation of the J0 specimen modeled by Abu Tahnat YB at al [33].

II.10 CONCLUSION

This chapter has presented a comprehensive review of the existing literature on the performance of deficient BCJs and their retrofitting using CFRP composites through various methods. Among these, the GM has shown significant potential for enhancing bond strength and overall joint performance. However, a detailed understanding of how key parameters influence the behavior of joints retrofitted with this method remains limited. Existing studies primarily focus on individual parameters or alternative retrofitting techniques.

Furthermore, a critical gap in the literature is the limited validation of numerical models, particularly those utilizing the CDP model in ABAQUS, against experimental results for joints retrofitted with the GM. Most numerical models have concentrated on the EBR technique, while numerical modeling specific to the GM remains underexplored, especially in terms of bond behavior and failure mechanisms.

To bridge these gaps, this thesis numerically investigates the performance of BCJ retrofitted with CFRP composites using the GM under various parameters. The study employs a finite element model developed in ABAQUS, which is validated through comparisons with experimental load-displacement curves, peak loads, and failure modes. Given the strong bond strength resulting from the GM, a perfect bond assumption is adopted in the numerical simulation to eliminate bond-slip effects. Additionally, a parametric study is conducted to examine the influence of key parameters on joint shear capacity, load-displacement response, and damage indices. The findings from this investigation aim to provide deeper insights into the effectiveness of the GM for retrofitting BCJs and contribute to the refinement of numerical modeling approaches.

*Chapter **III**:*

Modelling and Validation

Chapter III: Modelling and Validation

III.1 INTRODUCTION

Finite Element (FE) modelling is a powerful computational technique that plays a critical role in the analysis of concrete structural members. It offers significant advantages over traditional laboratory testing methods, including increased efficiency, cost-effectiveness, and the ability to simulate complex structural behaviors under a variety of conditions. By leveraging advanced computational tools such as ABAQUS software, researchers can gain deeper insights into the performance and failure mechanisms of structural components, facilitating the design of safer and more resilient structures.

This chapter provides a comprehensive overview of the FE modelling approach employed in this study. It begins with a review of recently published experimental work conducted on retrofitted BCJ with CFRP composites, which serves as a basis for validating the FE models. Following this, the chapter delves into the methodology and implementation of FE modelling using ABAQUS software. Key aspects covered include the geometric representation of structural members, detailed material modelling, the application of loading and boundary conditions, meshing and the verification of FE analysis results against experimental data.

By integrating these elements, the chapter aims to demonstrate the robustness and accuracy of FE modelling in capturing the complex nonlinear behavior of retrofitted BCJ. The insights gained from this modelling approach not only validate the computational models but also enhance our understanding of the structural performance of these components under various parameters.

III.2 SUMMARY OF EXPERIMENTAL PROGRAM

III.2.1 GEOMETRIC AND DIMENSIONS

The experimental program was selected from the literature to rigorously validate the precision of numerical simulations by investigating BCJs retrofitted with CFRP composites and subjected to cyclic loading conditions. Three specimens were chosen for this purpose: S (Seismically designed), NS (Non-Seismic), and R2NS (Retrofitted Non-Seismic), all referenced from a recent study by Davodikia et al [27]. These specimens, originally part of the third floor of a five-story structure, were carefully scaled down by a factor of ½ for the experiment.

The S specimen served as the control and was designed in accordance with ACI Committee 318M-14 [34]. The two non-seismically designed specimens, NS (Control) and R2NS

(Retrofitted), were deliberately constructed without transverse reinforcement in the joint panel and included wider stirrup spacing in the beams and columns. This approach aimed to replicate the inadequate shear strength commonly found in older, non-seismic BCJs. However, it is important to note that the longitudinal reinforcements for both beams and columns strictly complied with the seismic standards set by ACI Committee 318M-14 [34], except for the transverse reinforcement.

The columns in all sub-assemblages had cross-sectional dimensions of 250 × 250 mm and a height of 2100 mm. The beams had cross-sectional dimensions of 220 × 250 mm and extended 1400 mm from the column face. Figure III.1 illustrates the reinforcement details and precise dimensions of the selected BCJs.

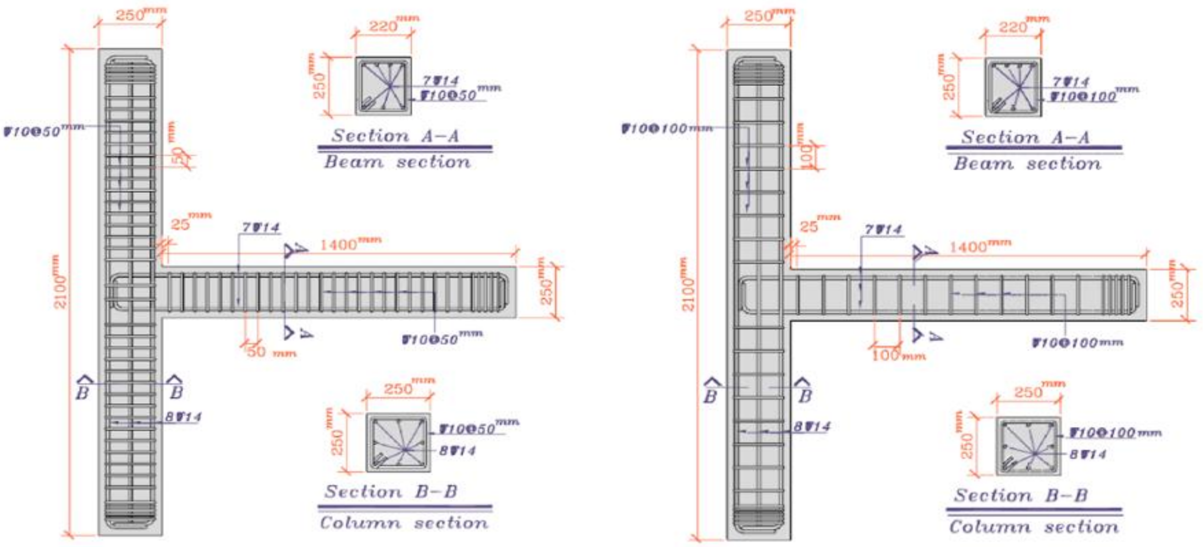

(a) S specimen (b) NS and R2NS specimens

Figure III.1. Dimensions and reinforcement details of the tested specimens [27].

III.2.2 RETROFITTING DETAILS

The R2NS specimen was tested after being retrofitted with CFRP composites in three distinct configurations, as illustrated in Figure III.2(a), which are described as follows:

1) For shear strengthening of the joint panel, two U-shaped sheets were applied with the fiber orientation parallel to the beam axis, extending 400 mm along the beam from the column face.
2) Two layers of sheets, each 750 mm long, were affixed to both sides of the column in the area of the joint panel, with the fiber orientation parallel to the column axis.

3) Two 250 mm wide wrapping layers were placed around the beam section near the column face and around the column sections at the top and bottom of the joint panel.

To install the CFRP sheets, grooves measuring 8 mm in depth and 4 mm in width, with a clear spacing of 30 mm, were cut into the concrete surfaces before applying the initial adhesive layer, as illustrated in Figure III.2(b). These grooves were then filled with a primary adhesive to create a perfectly smooth and uniform surface for the retrofit sheets. Notably, the grooves increase the contact surface area between the adhesive and the concrete, thereby enhancing the adhesion resistance of the CFRP sheets [27].

The grooves were oriented parallel to the sheet fibers to optimize adhesion and bond strength. This alignment ensures consistent stress transfer between the grooves and fibers, resulting in improved stress distribution among the grooves, adhesive, and fibers [27].

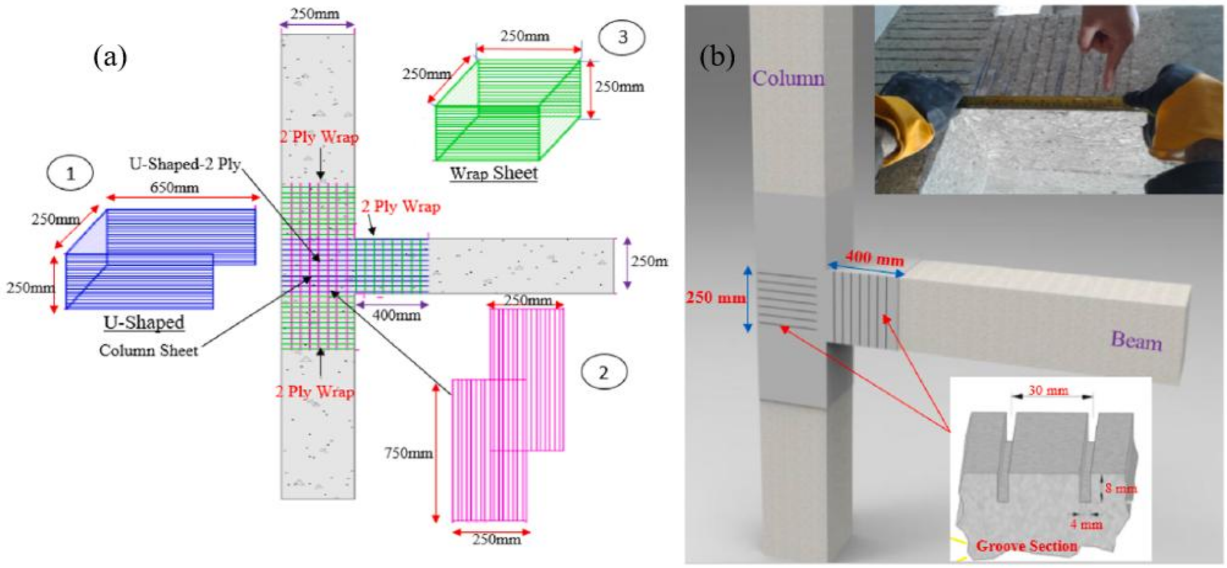

Figure III.2. Details of retrofitting for the R2NS specimen: (a) Configuration of layers, (b) Grooves created in the concrete surfaces [27].

III.2.3 EXPERIMENTAL SETUP

The BCJs were subjected to comprehensive testing conditions: lateral reversed cyclic loading applied to the beam tip to simulate seismic loading conditions, along with a constant compressive axial load applied to the top surface of the column to replicate the gravitational forces typically experienced in building structures. Figure III.3 provides a detailed schematic of the loading setup, illustrating the comprehensive testing configuration.

The boundary conditions at both ends of the column were defined as pinned supports, allowing free rotational movement. The testing procedure began with a 300-kN capacity hydraulic jack applying a consistent axial load of 175 kN to the top of the column, which remained unchanged throughout the tests. Subsequently, a hydraulic actuator with a capacity of 600 kN was used to apply the lateral cyclic load at the beam's end. The lateral load at the beam's free end was accurately measured using an S-shaped load cell. Additionally, a displacement sensor capable of recording up to 150 mm was employed to monitor the displacement of the beam's end throughout the loading cycles.

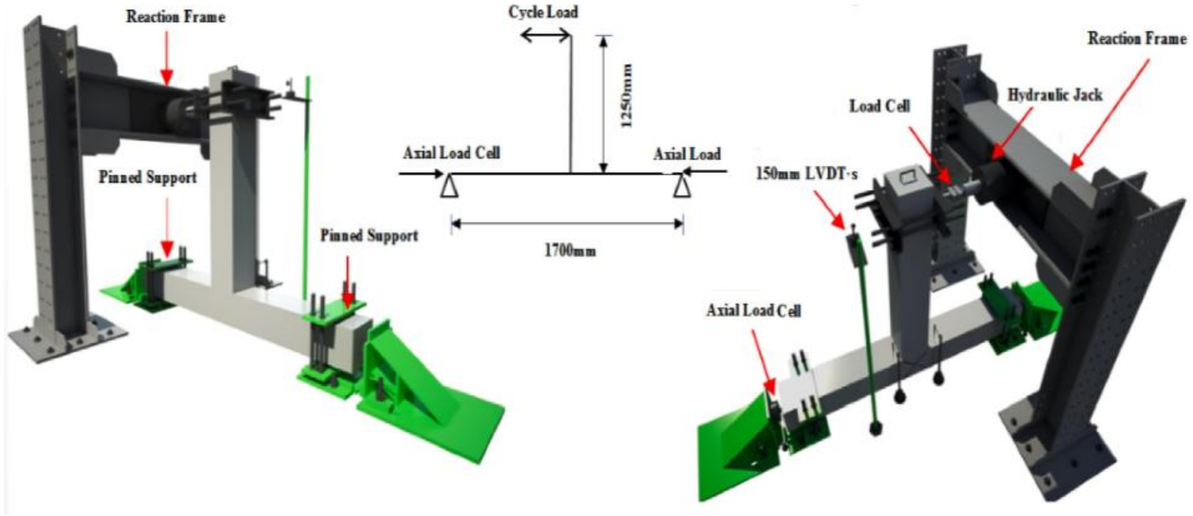

Figure III.3. Experimental setup and boundary conditions for BCJ Testing [27].

III.2.4 LOADING PROTOCOL

The cyclic loading history was applied using a displacement control method, as shown in Figure III.4. Each lateral drift level consisted of three repeated cycles to ensure consistent loading behavior. The drift ratio, a critical parameter, was determined by dividing the horizontal displacement at the loading point (*Δ*) by the distance from the load point to the column face (*h*=1250 mm). The loading protocol progressed with drift ratios ranging from 0.5% to 6%, increasing incrementally by 0.5% per step.

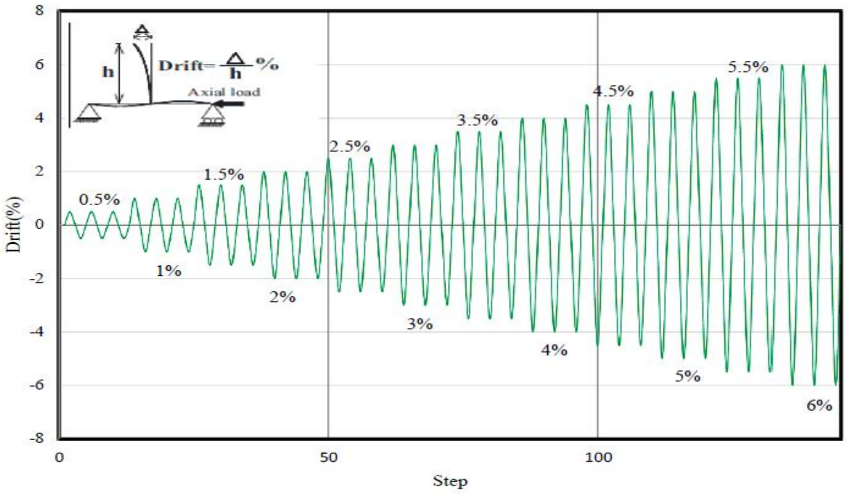

Figure III.4. Loading protocol applied in the experiment [27].

III.3 NUMERICAL MODELLING

In this study, ABAQUS software is employed to develop a 3D finite element (FE) model for simulating both the control and retrofitted exterior BCJs. The FE model accurately represents the geometric properties of the test specimens, material nonlinearity, axial loads applied to the column, and the interactions between structural components.

To simulate the behavior of shear-retrofitted BCJs under cyclic loading, a monotonic FE analysis was adopted as a simplified and computationally efficient approach. Monotonic FE analysis involves applying the load in one direction, gradually increasing it without any reversals or cycles. This method simplifies the simulation by focusing on the joint's response to increasing load, rather than replicating the cyclic loading behavior. Although it does not fully capture the back-and-forth loading of seismic events, it still provides useful insights into the material's behavior under increasing stress and helps predict failure mechanisms.

In this context, the beam load was smoothly applied to simulate the quasi-static condition, which provides acceptable accuracy in localizing strength drops during loading. This loading condition can effectively represent the envelope of the hysteresis curve typically seen in cyclic loading [35-37]. By smoothly applying the load, the model is able to capture critical points of strength reduction, closely following the general behavior observed under real cyclic loading without the complexity of full cyclic reversals.

The following sections provide a comprehensive overview of the modelling process, detailing key aspects such as solver selection, the constitutive models of the materials, interaction definitions, loading conditions, boundary conditions, and meshing strategies.

III.3.1 SOLVERS IN ABAQUS

ABAQUS, developed by Dassault Systèmes, is a widely recognized finite element analysis (FEA) software suite renowned for its robust capabilities in simulating complex structural, thermal, and mechanical behaviors. It is extensively used in civil engineering, particularly for modeling nonlinear and dynamic responses of structures such as reinforced concrete (RC) under diverse loading conditions.

The software provides two primary solvers, implicit and explicit, enabling users to choose the appropriate solver based on the specific requirements of the analysis. The choice of solver is critical for achieving accurate results and maintaining computational efficiency, particularly in nonlinear quasi-static problems.

This thesis investigates retrofitted BCJs with CFRP composites, employing nonlinear quasi-static analysis to evaluate structural responses under controlled loading conditions. Nonlinear quasi-static simulations require specialized algorithms to account for equilibrium states under slow, progressive loading.

This section provides a detailed overview of these solvers, focusing on their methodologies and applications in quasi-static analysis, particularly in the context of the retrofitted BCJs studied in this research.

III.3.1.1 IMPLICIT (STANDARD) SOLVER

The implicit solver is primarily designed for static equilibrium problems, where the system's response is calculated incrementally, and the equilibrium is satisfied at each step through iterative solutions. In ABAQUS, the implicit solver uses the Newton-Raphson method for solving nonlinear problems. This method is based on the principle of force equilibrium, ensuring that the internal forces (F_{int}) balance the external forces (F_{int}) at every increment as shown in Eq. III-1:

$$R = F_{ext} - F_{int} = 0 \qquad \text{III-1}$$

This equilibrium condition is solved incrementally and iteratively, making the implicit solver well-suited for quasi-static problem.

Incremental Approach

The solution process begins with dividing the simulation into increments (Δ_t), representing discrete steps in time or load. These increments allow for gradual application of loading conditions. ABAQUS uses an adaptive increment strategy, which adjusts the increment size dynamically based on the complexity of the solution. For example:

- In regions with mild nonlinearities, larger increments are used to enhance computational efficiency.
- Near points of high nonlinearity or instability, the increment size is reduced to improve solution accuracy and convergence.

Iterative Process

Within each increment, the solver uses an iterative method to refine the solution until the residual forces (R) are minimized to within a predefined tolerance. This is typically achieved using the Newton-Raphson method, which iterates as follows:

Residual force calculation: The imbalance between external and internal forces is calculated:

$$R = F_{ext} - F_{int} \tag{III-2}$$

Tangent stiffness matrix: The nonlinear force-displacement relationship is linearized by computing the tangent stiffness matrix (K_{tang}):

$$R = K_{tang} \times \Delta u \tag{III-3}$$

Displacement correction: The displacement vector is updated using:

$$\Delta u = K_{tang}^{-1} \times R \tag{III-4}$$

Force update: The internal forces (F_{int}) are recomputed based on the corrected displacements, and the residual is recalculated.

Convergence check: If the norm of the residual vector ($\| R \|$) falls below a specified tolerance, the solution is accepted, and the solver proceeds to the next increment. If not, iterations continue.

This iterative process ensures high accuracy, but it may be computationally intensive, especially for models with complex nonlinearities.

III.3.1.2 EXPLICIT SOLVER

The explicit solver is designed for dynamic problems that involve high-speed transients, where equilibrium is updated at each time increment without requiring iteration. Instead of solving the equilibrium equations incrementally through iterations, the explicit solver directly integrates the equations of motion over small-time increments (Δ_t). A central difference scheme is employed to explicitly integrate the equations of motion through time [38], updating the displacement, velocity, and acceleration at each time step. The term "explicit" refers to the fact that the system’s state at the end of an increment is determined using the values (displacements, velocities, accelerations) available at the beginning of the increment [38]. The governing equation for the explicit solver in terms of dynamic equilibrium is expressed as:

$$M\ddot{u} = P - I \tag{III-5}$$

Where:

M: is the nodal mass matrix;

$\ddot{u}$: is the nodal acceleration;

P: is the externally applied force;

I: is the internal element force;

Incremental approach

In the explicit method, the model's state is advanced through small time increments to accurately capture the analysis solution. These increments must remain below a stability limit to prevent numerical instability and convergence issues. If the time increment exceeds this limit, the solution may become unreliable or fail.

The stability limit, $\Delta stable$, can be estimated using the smallest element length L_{min} in the mesh and the material wave speed c_d, as expressed in the following equation:

$$\Delta stable = \frac{L_{min}}{c_d} \qquad \text{III-6}$$

The wave speed c_d is defined as:

$$c_d = \sqrt{E/\rho} \qquad \text{III-7}$$

where E is the Young's modulus and ρ is the material density. Ensuring that the time increment is sufficiently small maintains numerical stability and avoids convergence problems. ABAQUS/Explicit optimizes computational efficiency by automatically selecting time increments as close as possible to the stability limit without exceeding it. This time incrementation process is fully automated and requires no user intervention [38].

Direct integration without iteration

Unlike the implicit solver, the explicit solver avoids iterations by directly updating the system's state at each increment:

1. Acceleration calculation: The solver calculates the acceleration at time t based on the external and internal forces. Since the explicit procedure uses a diagonal mass matrix (with mass distributed at the nodes), there is no need to solve a system of equations [38]. The accelerations are determined by the mass and the forces acting on the nodes, as expressed by:

$$\ddot{u}(t) = M^{-1}\big(P(t) - i(t)\big) \qquad \text{III-8}$$

2. Velocity update: The accelerations are integrated over time using the central difference method, which assumes constant acceleration within each small-time increment (Δ_t). The change in velocity is added to the velocity at the middle of the previous increment to determine the velocity at the middle of the current increment [38]:

$$\dot{u}\big(t + (\Delta t/2)\big) = \dot{u}\big(t - (\Delta t/2)\big) + \left(\frac{\Delta t_{(t-\Delta t)} + \Delta t_{(t)}}{2}\right) \times \ddot{u}_{(t)} \qquad \text{III-9}$$

3. Displacements update: Velocities are integrated over time and combined with the initial displacements at the beginning of the increment to calculate the displacements at the end of the increment [38] as depicted in Eq. III-10:

$$u(t + \Delta t) = u(t) + \Delta t \times \dot{u}(t + \Delta t/2) \qquad \text{III-10}$$

4. Compute element strain increment, d_{ε}, based on the strain rate (rate of change of strain over time) $\dot{\varepsilon}$.

5. Once the strain increments are calculated, the next step is to compute the stress increments using the materials constitutive relationships.

$$\sigma(t + \Delta_t) = f\left(\sigma_{(t)}, d_{\varepsilon}\right) \qquad \text{III-11}$$

III.3.1.3 ALGORITHM SELECTION

The Table III-1 presents the key differences between the standard and explicit solvers. A comparative study conducted by Benham et al [39] to model the behavior of RC wide beam-column joints using both the standard and explicit solvers. In the explicit analysis, two different displacement application velocities were investigated. The results, presented in Figure III.5, indicate that both solvers produce closely matching curves when compared to the experimental backbone curves. However, as the loading rate decreased in the explicit analysis, the difference between the standard and explicit solutions also diminished.

In our study, the behavior of concrete exhibits significant nonlinearity, characterized by a severe reduction in strength after reaching the peak load and the development of damage. Consequently, the use of ABAQUS/Standard may encounter several convergence issues, as achieving equilibrium requires multiple iterations in each increment. To overcome these challenges, the explicit analysis was adopted in this study to avoid the common issues typically associated with ABAQUS/Standard.

Table III-1. Comparison of the implicit and explicit solver.

Aspect	Implicit solver	Explicit solver
Increment size	Large, adaptive increments	Small increments governed by stability conditions.
Iterations	Iterative process (Newton-Raphson) to ensure convergence with each increment.	No iterations, directly updates using explicit integration.
Convergence	Guaranteed convergence if increments are small enough.	Relies on small increments and damping to approximate equilibrium.
Efficiency	Computationally efficient for moderate nonlinearities but costly for highly nonlinear systems.	Suitable for highly nonlinear problems but requires significant computational resources.
Stability for Quasi-static problems	Ideal due to its ability to ensure force equilibrium.	Viable only when inertial effects are minimized, and artificial damping is introduced.

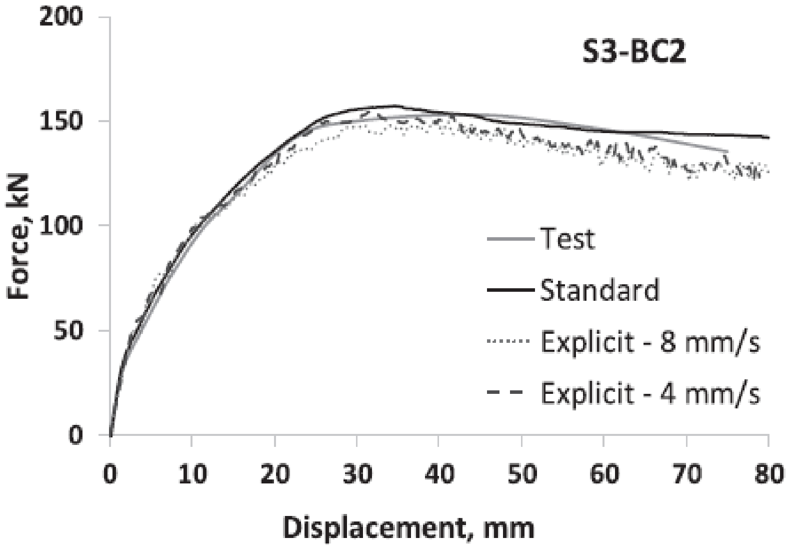

Figure III.5. Force-Displacement Comparison: Standard vs. Explicit Solvers [39].

III.4 LOADING RATE SELECTION

In explicit analysis, the equation of motion accounts for the mass of the system, which introduces inertial forces that may lead to an unbounded solution. To mitigate the effects of these inertial forces, the applied load should be introduced as slowly as possible. In this context, the loading rate, defined as the ratio of the applied displacement to the loading time, must be carefully selected. A high loading rate can result in significant inertial forces, leading to unrealistic numerical solutions. Conversely, an excessively low loading rate may substantially increase computational time, making the analysis inefficient. Therefore, it is crucial to find a suitable loading rate that ensures both solution accuracy and computational efficiency.

A commonly used criterion to ensure that the loading rate is sufficiently small, allowing inertial forces to be neglected, is to monitor the kinetic energy of the entire model. It is recommended that the kinetic energy remains significantly lower than the internal energy throughout the analysis [38]. A numerical study on flat slab-column connections found that when the kinetic energy was less than 1% of the internal energy, the model produced reliable results [40].

In this study, the loading rate was examined under various velocities. Figure III.6 presents the comparison between the kinetic and internal energy during the analysis of the three modeled specimens at a loading rate of 6.5 mm/s. In all analyses, the kinetic energy was found to be lower than 0.5% of the internal energy. Therefore, it can be concluded that inertial forces and dynamic effects are negligible at this loading rate. Consequently, a loading rate of 6.5 mm/s was adopted for the subsequent analyses.

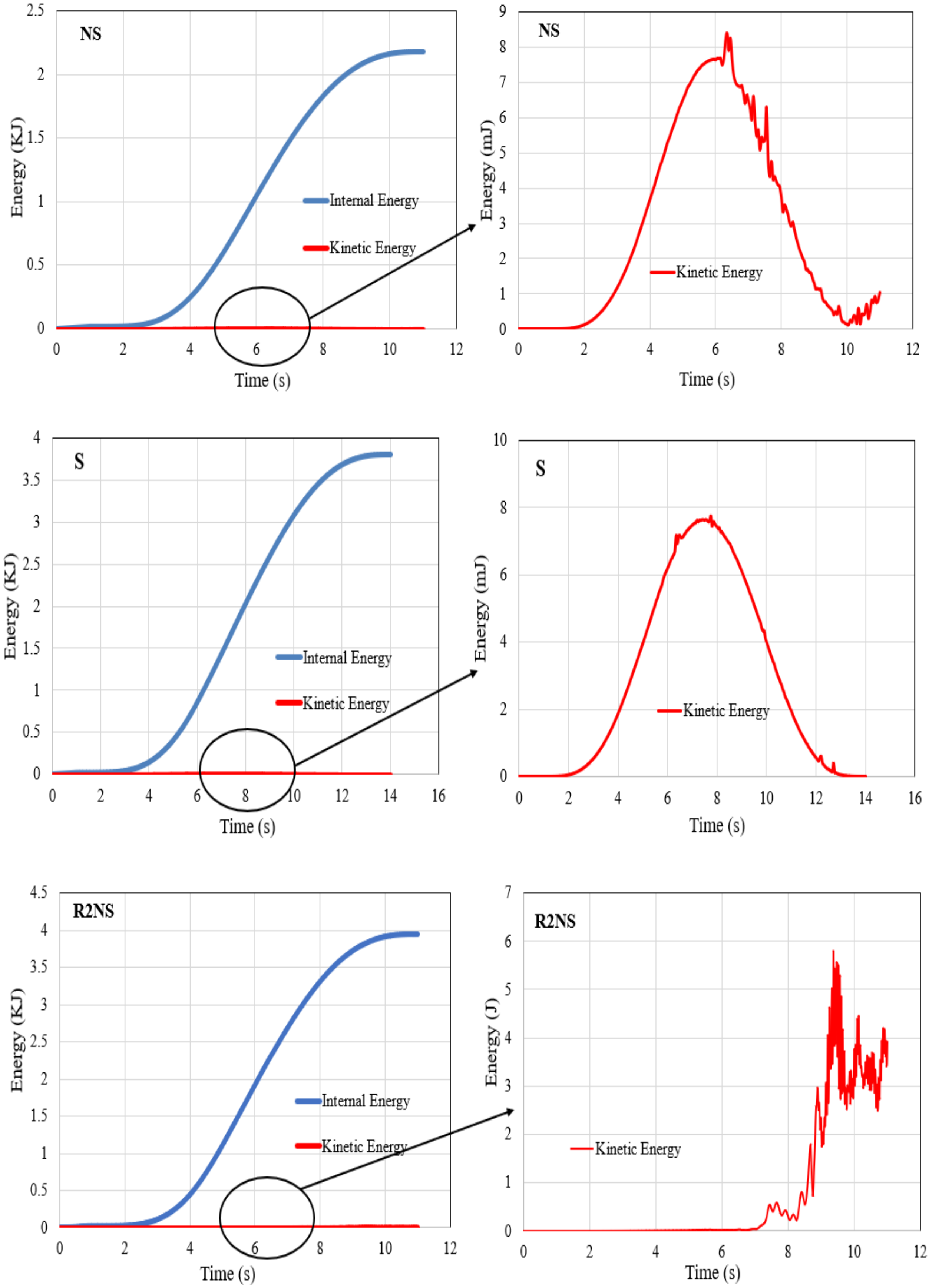

Figure III.6. Comparison of the kinetic and internal energy of the modeled specimens at a loading rate of 6.5 mm/s.

III.5 SMOOTH STEP AMPLITUDE

To achieve both accuracy and efficiency in quasi-static analyses, it is crucial to apply the loading in a gradual and smooth manner. Sudden or abrupt load applications can generate stress waves, potentially leading to noisy or inaccurate results. Ensuring a smooth load application involves minimizing changes in acceleration between successive increments. When acceleration varies smoothly, the resulting velocity and displacement also exhibit smooth transitions, enhancing numerical stability. In this study, the smooth step amplitude function available in ABAQUS, as illustrated in Figure III.7, was employed to impose displacement. This function automatically generates a smooth loading pattern, helping to maintain quasi-static conditions by preventing wave generation that may arise from abrupt changes in the loading rate.

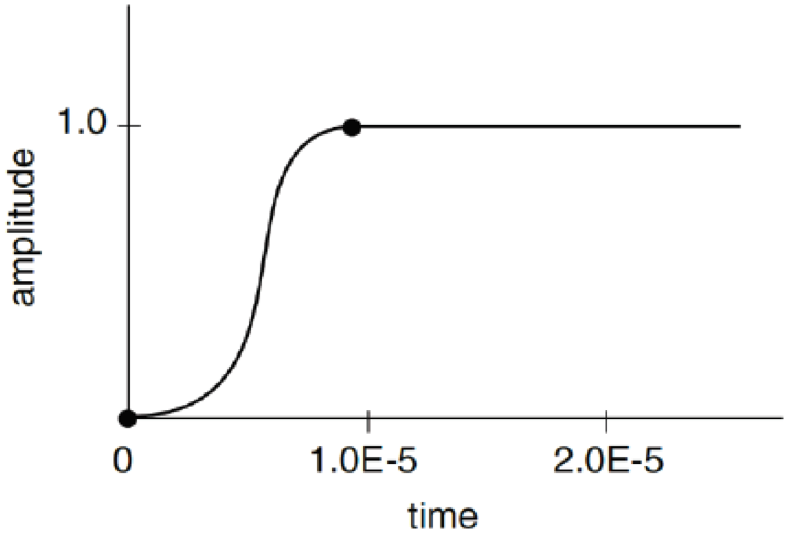

Figure III.7. Example illustration of the smooth step amplitude function [41].

III.6 MATERIAL CONSTITUTIVE MODELS

III.6.1 CONCRETE MODELLING

ABAQUS provides several constitutive models for simulating the nonlinear behavior of concrete, including the Smeared Crack Model (SCM), the Brittle Cracking Model (BCM), and the Concrete Damage Plasticity (CDP) model. The SCM, available only in ABAQUS/Standard, is suitable for modeling tensile cracking behavior. The BCM assumes that concrete behaves in a linear elastic manner under compression and is typically used when tensile cracking dominates [38]. In contrast, the CDP model effectively captures the nonlinear behavior of concrete and reinforced concrete under both tensile and compressive loads, making it ideal for modeling damage progression. Due to its demonstrated accuracy in numerous studies [42-44], the CDP model was chosen for this study.

The CDP model is a continuum, plasticity-based damage model designed to simulate the progressive failure of concrete structures under monotonic or cyclic loading [38]. It captures both tensile cracking and compressive crushing, which are common in reinforced concrete components. Implementing the CDP model requires defining specific material parameters, including:

1. Plasticity parameters;
2. Uniaxial stress-strain relationship under compression and tension;
3. Damage scalar parameters d_c and d_t under compression and tension respectively;

III.6.1.1 STRESS-STRAIN RELATIONSHIP

The CDP model is based on a plasticity framework that incorporates two scalar damage variables: d_c for compression and d_t for tension. These variables represent the extent of material degradation under uniaxial loading. As shown in Figure III.8, the material's response upon unloading is weaker in both compression and tension due to the reduction in elastic stiffness. This stiffness degradation is directly controlled by the damage variables, which range from 0 (no damage) to 1 (complete loss of strength).

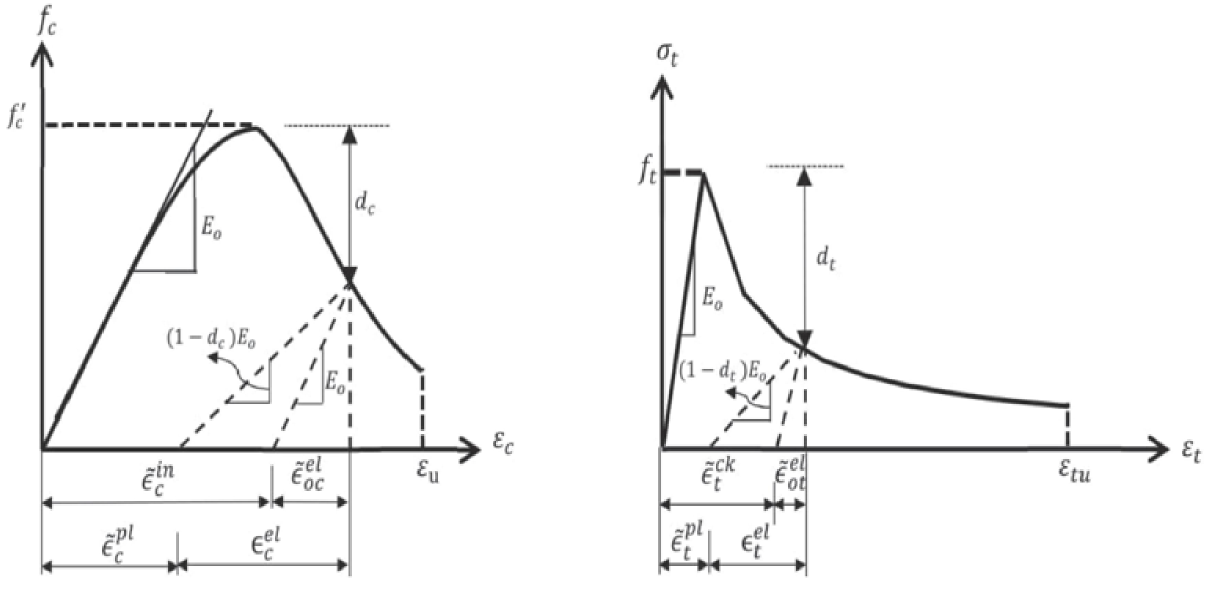

(a) (b)

Figure III.8. Concrete material response. (a): In compression; (b): In tension [45].

By progressively reducing the material stiffness as loading increases, the CDP model effectively simulates the degradation of concrete. The stress-strain relationships according to this model under multiaxial loading are expressed as:

$$\sigma = (1-d)D_0^{el}:(\varepsilon - \varepsilon^{pl}) = D^{el}:(\varepsilon - \varepsilon^{pl}) \qquad \text{III-12}$$

Where D_0^{el} is the initial (undamaged) elastic stiffness of the material; $D^{el} = (1-d)D_0^{el}$ is the degraded elastic stiffness. ε and ε^{pl} are the total and plastic strain respectively. $\bar{\sigma}$ is the effective stress. And the Cauchy stress σ is related to the effective stress $\bar{\sigma}$ through the scalar degradation relation shown in Eq. III-13.

$$\sigma = (1-d)\bar{\sigma} \tag{III-13}$$

III.6.1.2 YIELD CRITERION

The CDP model utilizes a yield condition based on the yield function proposed by Lubliner et al [46], incorporating modifications by Lee and Fenves [47] to account for the differing evolution of strength under tension and compression. In terms of effective stresses, the yield function is expressed as illustrated in Eq. III-14:

$$F = \frac{1}{1-\alpha}\left(\bar{q} - 3\alpha\bar{p} + \beta(\tilde{\varepsilon}^{pl})\langle\bar{\sigma}_{max}\rangle - \gamma\langle\bar{\sigma}_{max}\rangle\right) - \bar{\sigma}_c\left(\tilde{\varepsilon}_c^{pl}\right) \leq 0 \tag{III-14}$$

Where

- α, β and γ are dimensionless material constants which need to be defined in Eqs. III-(15)-(17);
- $\bar{p}$ is the effective hydrostatic pressure;
- $\bar{q}$ is the equivalent von mises stress;
- $\bar{\sigma}_{max}$ is the algebraically maximum eigenvalue of tensor $\bar{\sigma}_c$.

$$\alpha = \frac{(\sigma_{b0}/\sigma_{c0})-1}{2(\sigma_{b0}/\sigma_{c0})-1} \tag{III-15}$$

$$\beta(\tilde{\varepsilon}^{pl}) = \frac{\bar{\sigma}_c\left(\tilde{\varepsilon}_c^{pl}\right)}{\bar{\sigma}_t\left(\tilde{\varepsilon}_t^{pl}\right)}(1-\alpha) - (1+\alpha) \tag{III-16}$$

$$\gamma = \frac{3(1-K_c)}{2K_c-1} \tag{III-17}$$

The yield surface is governed by the relationship between effective stresses and the parameters that define the material's behavior under various loading conditions. The constant α controls the yield surface shape under biaxial stress states. The ratio $(\sigma_{b0}/\sigma_{c0})$, representing the ratio of biaxial compressive yield stress to uniaxial compressive yield stress, significantly influences the yield surface in a plane stress state. Experimental values of this ratio typically range from 1.10 to 1.16, leading to values of α between 0.08 and 0.12 [46].

The effective tensile and compressive cohesion stresses, $\bar{\sigma}_c(\tilde{\varepsilon}_c^{pl})$ and $\bar{\sigma}_c\left(\tilde{\varepsilon}_t^{pl}\right)$, respectively, are used to describe the yield conditions under tensile and compressive stress states. The coefficient γ is introduced only for triaxial compression stress states. It can be determined by comparing the yield conditions along the tensile meridian (TM) and the compressive meridian (CM), ensuring the yield surface appropriately represents the material behavior under various stress states.

Furthermore, the parameter K_c is used to define the shape of the deviatoric cross-section of the yield surface, as shown in Figure III.9. Part (a) of the figure shows typical yield surface under plane stress conditions, while part (b) illustrates the shape in the deviatoric plane.

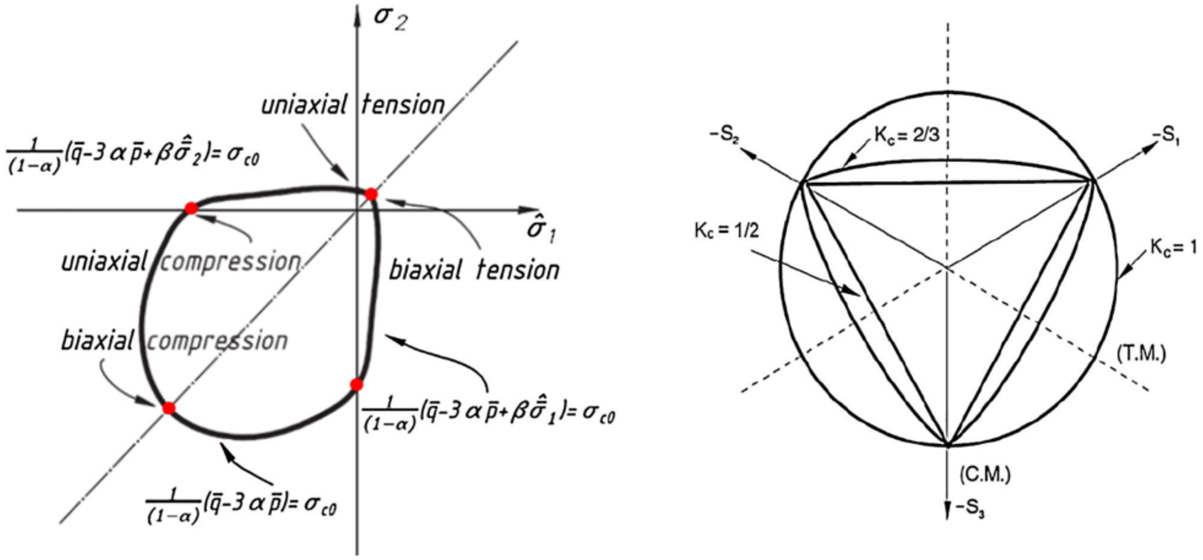

(a) (b)

Figure III.9. Shape of the yield surface. (a) in the plane stress; (b) in the deviatoric plane [39].

III.6.1.3 FLOW RULE

In non-associative plasticity, the direction of plastic flow is determined by a potential function, G, which differs from the yield function, F. The potential function governs the flow direction and is often described by a hyperbolic formulation based on the Drucker-Prager model. This formulation is particularly suitable for modeling materials such as concrete, which experience complex stress states under high triaxial loading conditions. The potential function used to define the plastic flow direction in non-associative plasticity is expressed as illustrated in Eq. III-18:

$$G = \sqrt{(\varepsilon\sigma_{t0}\tan\psi)^2 + \bar{q}^2} - \bar{p}\tan\psi \qquad \text{III-18}$$

In Eq. III-18:

- ψ is the dilation angle, controlling the inclination in the $p - q$ meridional plane, representing the material volumetric dilation tendency;
- σ_{t0} is the uniaxial tensile stress at failure;

- ε is the eccentricity parameter, that defines the rate at which the function approaches the asymptote;

The potential function G is graphically represented as a curve in the $p - q$ plane, which defines the direction of plastic flow, as illustrated in Figure III.10. The dilation angle ψ plays a crucial role in determining the slope of this flow direction, indicating the material's propensity to expand or contract under plastic deformation.

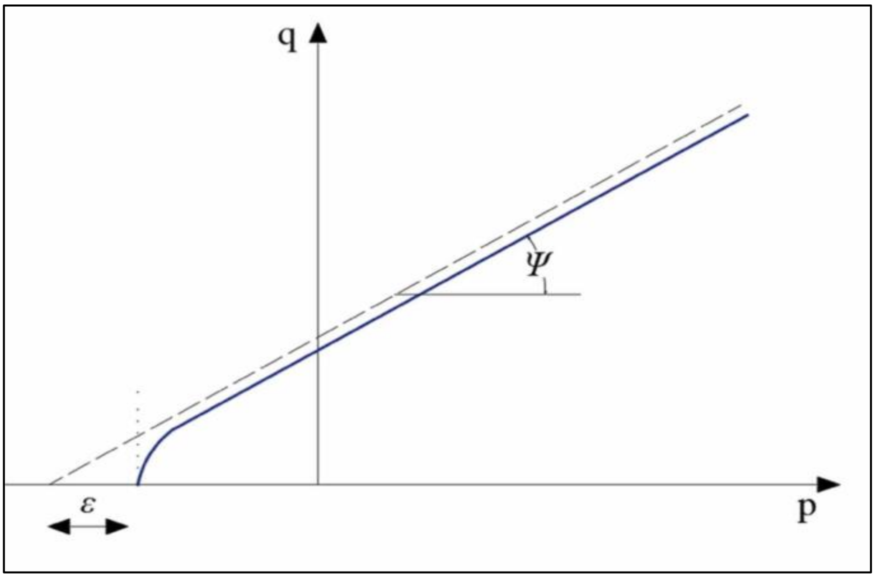

Figure III.10. Plastic flow representation in the meridian (p-q) plane [48].

III.6.1.4 DEFINING THE COMPRESSIVE BEHAVIOR

In this research, the compressive behavior of concrete under uniaxial compressive stress was represented through a two-phase stress-strain model. The initial phase corresponds to the elastic response of the material, where the stress increases linearly with strain up to a predefined yield stress, σ_{c0}. Following this elastic phase, the nonlinear response captures both hardening and softening behavior, which describes the material's plastic deformation and eventual failure. The yield stress, σ_{c0}, was assumed to be $0.4f_c'$, as is typical in such models [30,31].

The nonlinear stress-strain behavior of concrete in compression was modeled using the formulation proposed by Saenz [49], which offers an accurate representation of concrete's response under compressive loads. The governing mathematical expressions are presented in Eqs. III-(19)– (25), incorporating critical parameters such as the peak compressive strength (f_c'), the strain at peak stress (ε_0), and the ultimate strain (ε_f). To improve numerical convergence, the ultimate strain was conservatively set to a relatively high value of 0.035 [39].

The compressive strength of concrete, f_c', was determined from experimental results [27], while the modulus of elasticity (E_C) was calculated in accordance with the ACI 318-19 standard [50], as given in Eq. III-25. A Poisson's ratio of 0.2 was adopted to define the elastic behavior of the material.

To model the nonlinear stress-strain curve, the following equations were used:

$$\sigma_C = \frac{E_C \times \varepsilon_C}{1+(R+R_E-2)\left(\frac{\varepsilon_C}{\varepsilon_0}\right)-(2R-1)\left(\frac{\varepsilon_C}{\varepsilon_0}\right)^2+R\left(\frac{\varepsilon_C}{\varepsilon_0}\right)^3} \tag{III-19}$$

$$R = \frac{R_E(R_\sigma-1)}{(R_\varepsilon-1)^2} - \left(\frac{1}{R_\varepsilon}\right) \tag{III-20}$$

$$R_E = \frac{E_c}{E_0} \tag{III-21}$$

$$R_\sigma = \frac{f_c'}{\sigma_f} \tag{III-22}$$

$$R_\varepsilon = \frac{\varepsilon_f}{\varepsilon_0} \tag{III-23}$$

$$E_0 = \frac{f_c'}{\varepsilon_0} \tag{III-24}$$

$$E_c = 4700\sqrt{f_c'} \tag{III-25}$$

In these equations, ε_c is the strain under a given stress level (σ_c), ε_0 represents the strain at the peak stress, and ε_f is the strain at failure, E_0 is the secant modulus of concrete, σ_f compressive stress at failure. R, R_E, R_σ, and R_ε are parameters that's control the shape of the stress-strain curve.

To introduce the behavior of concrete in compression in the software, the input data were defined in terms of inelastic strain (crushing stain), $\tilde{\varepsilon}_c^{in}$, instead of plastic strain, $\tilde{\varepsilon}_c^{pl}$, the compressive inelastic strain is defined as the total strain, ε_c, minus the elastic strain, ε_{0c}^{el}, as shown in Eq. III-26, this is corresponding to the undamaged material. And the software automatically converts the inelastic strains to plastic strains considering the provided data for damage under compression according to Eq. III-27.

$$\tilde{\varepsilon}_c^{in} = \varepsilon_c - \varepsilon_{0c}^{el} = \varepsilon_c - \frac{\sigma_c}{E_C} \tag{III-26}$$

$$\tilde{\varepsilon}_c^{pl} = \tilde{\varepsilon}_c^{in} - \frac{d_c}{(1-d_c)}\frac{\sigma_c}{E_C} \tag{III-27}$$

The unloading response of the compressive stress-strain behavior is modeled in ABAQUS using the compressive damage curve, d_c versus $\tilde{\varepsilon}_c^{in}$. The damage parameter is introduced in the strain-softening region of the stress-strain curve, as defined in Eq. III-28 [51]:

$$d_c = 1 - \frac{\sigma_c}{f_c'} \qquad \text{III-28}$$

To ensure a precise characterization of concrete behavior, it is important to consult Figure III.11, which provides vital data for defining the material model. In particular, Figure III.11(a) illustrates the relationship between compressive stress and inelastic strain, while Figure III.11(b) shows the relation between the compression damage parameter and inelastic strains. This comprehensive data representation is instrumental in accurately capturing the behavior of concrete under compressive loading within the CDP model.

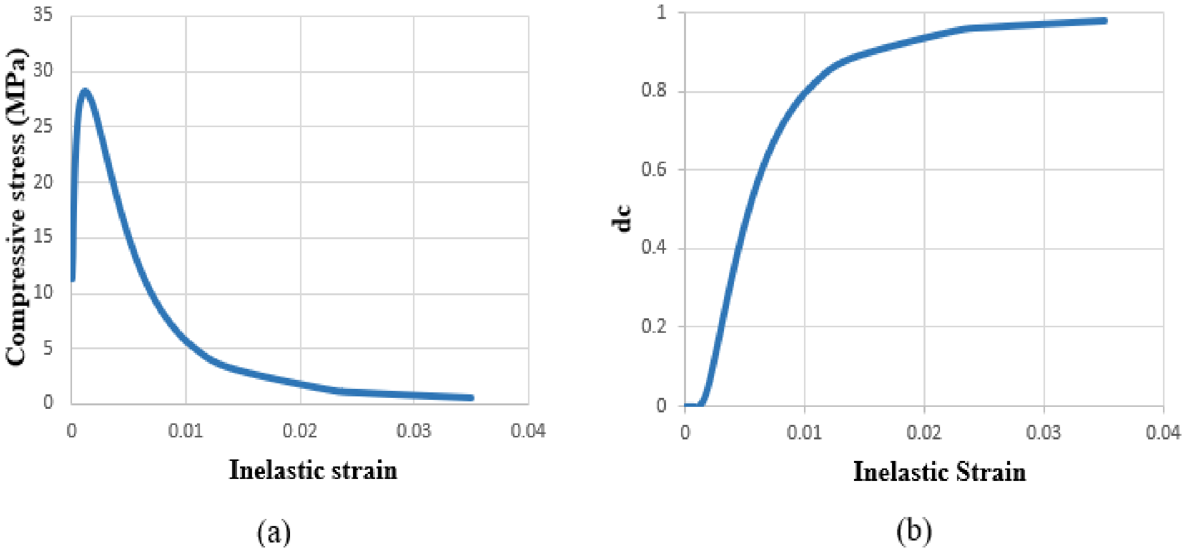

Figure III.11. Representation the compressive response of concrete in the CDP model: (a) stress versus inelastic strain; (b) Damage parameter versus inelastic strain.

III.6.1.5 DEFINING THE TENSILE BEHAVIOR

The tensile response of concrete under uniaxial loading initially follows a linear elastic relationship until the material reaches its tensile strength (f_t). At this point, micro-cracking begins to develop, signifying the transition from elasticity to the softening phase. This softening behavior, commonly referred to as *tension stiffening*, reflects the capacity of cracked concrete to sustain stress due to aggregate interlock and bond with reinforcement.

Modeling the post-cracking tensile behavior of concrete can be approached in two primary ways:

1. Using a post-failure stress-strain relationship.
2. Adopting a fracture energy criterion.

In finite element analyses, regions of concrete with limited reinforcement or severe localized cracking often exhibit significant mesh sensitivity when a post-failure stress-strain approach is applied [38]. In the current study, the joint region of the non-seismically modeled specimens does not contain any transverse reinforcement, and the un-retrofitted NS specimen exhibited shear failure with pronounced localized shear cracks. To address these challenges and ensure numerical stability, the fracture energy criterion was employed.

The fracture energy (G_f) represents the energy required to propagate a crack per unit area and serves as a critical parameter for modeling the post-cracking behavior. Instead of relying on a stress-strain relationship, the fracture energy approach defines the tensile softening behavior using a stress–cracking displacement ($\sigma - \omega$) relationship. The model proposed by Hilleborg et al [52] was utilized in this study, with the fracture energy represented as the area under the stress–cracking displacement curve (Figure III.12). The fracture energy can be quantified using Eq. III-29 [53]:

$$G_f = G_{f0}((f_c' + 8)/f_{cmo})^{0.7} \qquad \text{III-29}$$

Where, $f_{cmo} = 10\ MPa$ and G_{f0} is the base fracture energy, which depends on the maximum concrete aggregate size, d_{max}. for $d_{max} = 12mm$, the base fracture energy is $G_{f0} = 0.03\ N/mm$ [53]. The tensile strength of concrete f_t was calculated in accordance with ACI 318-19 standards [50], as expressed in Eq. III-30:

$$f_t = 0.33\sqrt{f_c'} \qquad \text{III-30}$$

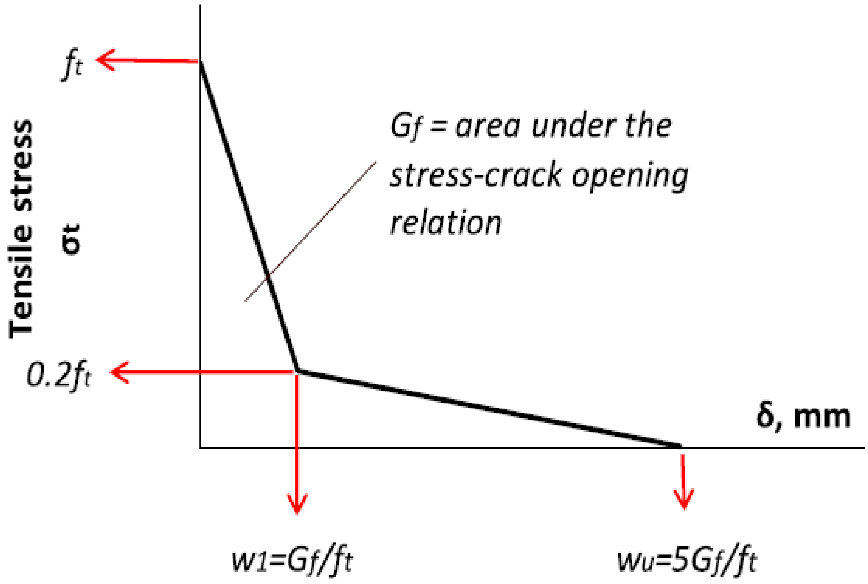

Figure III.12. Correlation between uniaxial stress and crack width [39].

The damage parameter in tension (d_t) was assumed to attain a value of 0.8 when the material's tensile strength diminished by 80%, and its highest value, 0.95, reflected a 95% loss of strength.

In ABAQUS, the tensile behavior of concrete is typically defined using the cracking displacement (u_t^{ck}) as input. However, the CDP model requires this to be represented as plastic displacement (u_t^{pl}). To address this, ABAQUS automatically performs a conversion based on the damage parameter (d_t) using Eq. III-31:

$$u_t^{pl} = u_t^{ck} - \frac{d_t}{(1-d_t)} \frac{\sigma_t l_0}{E_0} \qquad \text{III-31}$$

Where $l_0 = 1$ (unit length).

Figure III.13 illustrates the input data used to define the tensile behavior of concrete in the CDP model. Figure III.13(a) shows the tensile stress-cracking displacement curve, while Figure III.13(b) presents the relationship between the tensile damage parameter and the cracking displacement.

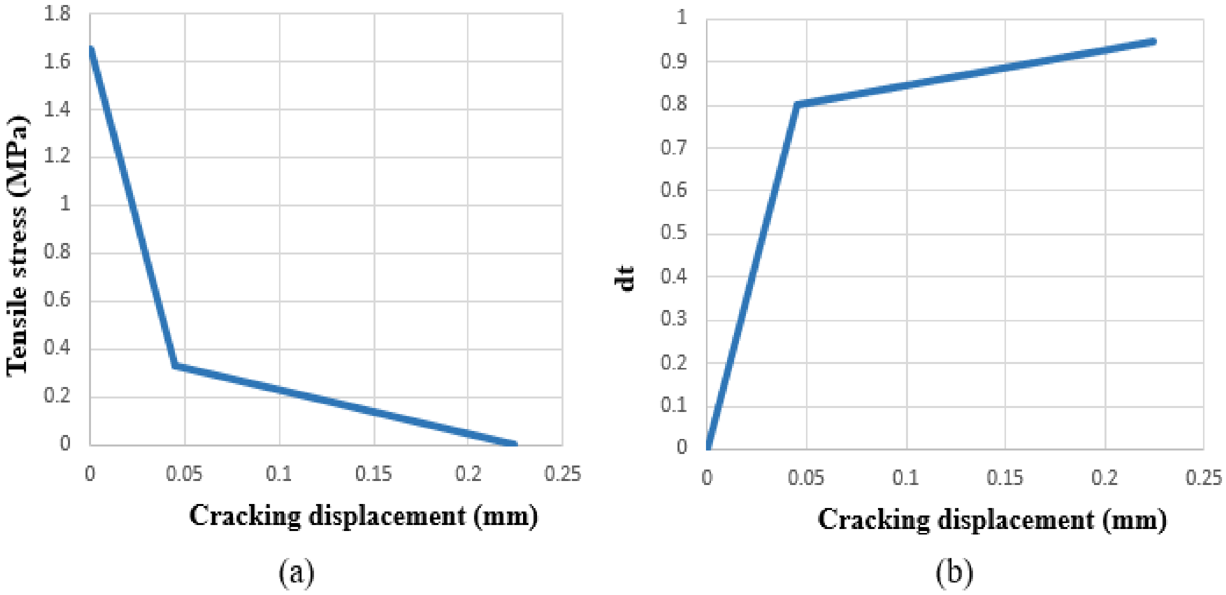

Figure III.13. Representation of the tensile response of concrete in the CDP model: (a) stress versus displacement; (b) Damage parameter versus displacement.

III.6.1.6 PLASTICITY PARAMETERS SELECTION

To accurately define the CDP model, four critical plasticity parameters need to be specified: the dilation angle (ψ), eccentricity (ε), the factor K_c, and the ratio of initial biaxial compressive stress to initial uniaxial compressive stress (σ_{c0}/σ_{b0}). This section provides a comprehensive investigation of the effects of these parameters, aiming to identify the most suitable and optimal values. Initially, the un-retrofitted NS specimen model was employed to examine the influence of each parameter. The optimal values obtained from this analysis were subsequently applied to S and R2NS specimen models. Based on recommendations from the ABAQUS User Guide [38], the initial values for ψ, ε, K_c, and σ_{c0}/σ_{b0} were set to 36°, 0.1, 0.67, and 1.16, respectively. Sensitivity analyses were conducted by varying each parameter independently to assess its impact, as described in the subsequent sections.

Effect of dilation angle

In the CDP model, the dilation angle (ψ) defines the slope of the failure surface relative to the hydrostatic axis on the meridian plane (see Figure III.10). Prior research by Genikomsou et al [42] suggests using a dilation angle between 31° and 42° for accurately modeling concrete behavior. This study assessed the impact of four dilation angles, 36°, 38°, 40°, and 42° on the load-displacement performance of the NS model. As depicted in Figure III.14, the load-bearing capacity is sensitive to changes in the dilation angle, with larger angles generally leading to increased peak loads. These trends are consistent with findings reported in the literature [42].

A smaller dilation angle of 36° resulted in an underestimation of the peak load by 7.13%, whereas a larger angle of 42° led to a slight overestimation of 5.44%. Notably, the dilation angle of 40° provided the most accurate correlation with the experimental load-displacement curve, overestimating the peak load by only 2.65%. Therefore, a dilation angle of 40° was selected for all subsequent analyses due to its optimal balance between numerical prediction and experimental validation.

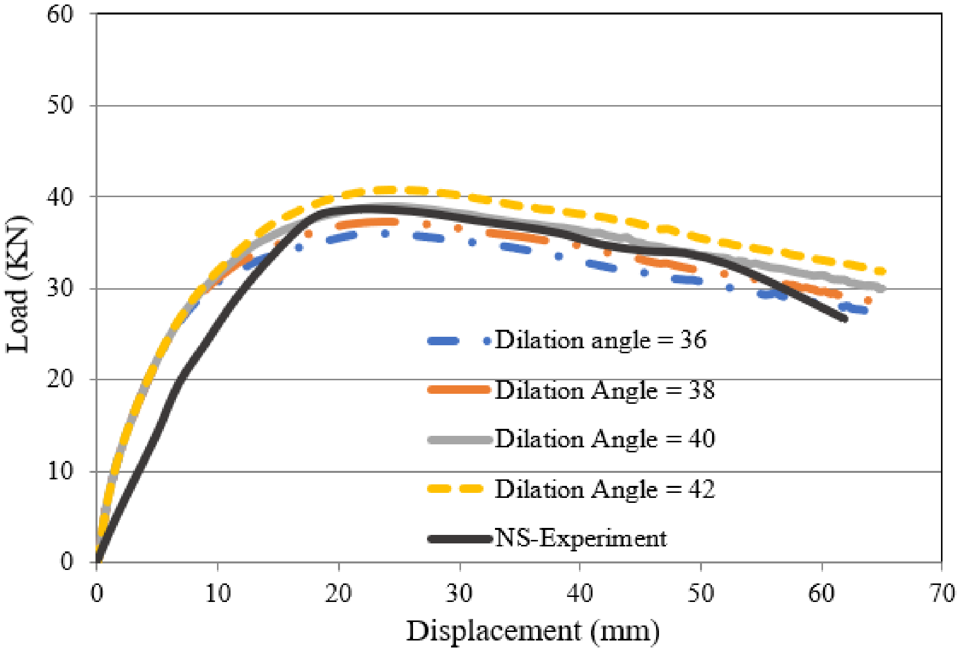

Figure III.14. Sensitivity analysis of the dilation angle on load displacement behavior.

Effect of K_c parameter

The coefficient K_c, which represents the ratio of the second stress invariant on the tensile meridian to that on the compressive meridian, significantly affects the shape of the yield surface in the deviatoric plane, as illustrated in Figure III.9. To ensure compliance with the initial yielding criterion, $0.5 \leq K_c \leq 1.0$ must be satisfied. A value of $K_c = 1$ corresponds to a circular yield surface, following the Drucker-Prager criterion, while $K_c = 2/3$ results in a yield surface composed of three tangent ellipses. The results presented in Figure III.15 highlight the influence of K_c on the load-displacement response under various values, particularly in the post-peak range. Numerical analyses reveal that $K_c = 1$ and $K_c = 0.8$ tend to underestimate residual strength, whereas $K_c = 0.5$ overestimates the joint's capacity. Among the tested values, $K_c = 0.667$ provides the closest match to experimental data, effectively capturing both peak and post-peak behavior. Therefore, $K_c = 0.667$ is adopted in subsequent analyses to achieve a realistic representation of joint performance.

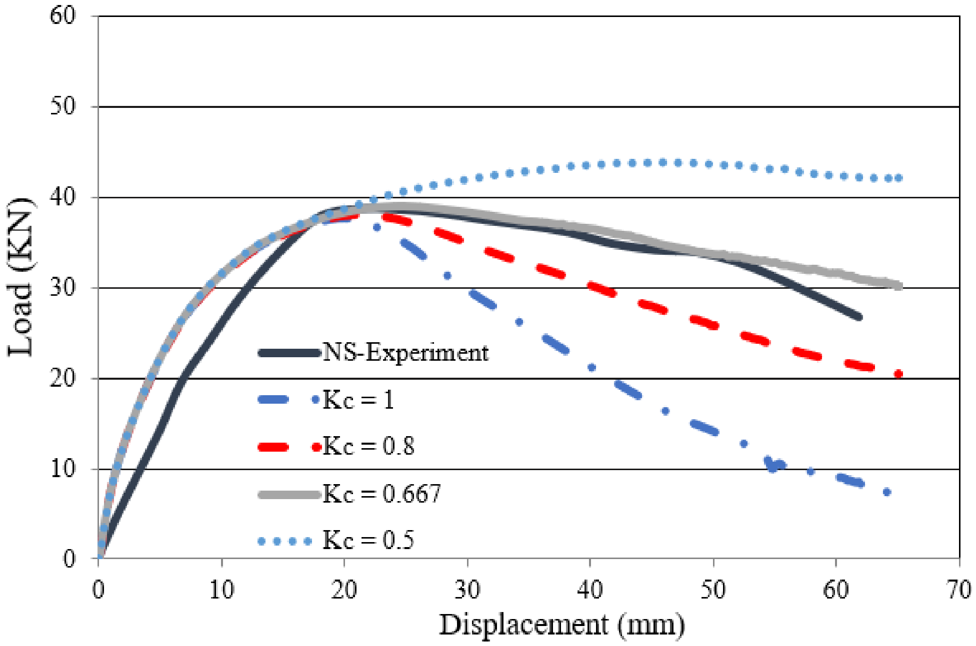

Figure III.15. Impact of parameter K_c on load displacement behavior.

Effect of σ_{c0}/σ_{b0} ratio and eccentricity ε

The ratio of biaxial to uniaxial concrete compressive strength is a crucial parameter in the CDP model, as it significantly influences under biaxial stress conditions. This parameter varies depending on the concrete material properties, with a standard default value of 1.16. To assess the suitability of this default setting, a sensitivity analysis was conducted using values of 1.06, 1.16, and 1.36.

The results revealed that this parameter primarily affects the softening region of the load-displacement response. Specifically, increasing the ratio to 1.36 enhanced the residual shear strength, indicating improved post-peak performance and ductility. In contrast, lower values (1.06 and 1.16) led to more pronounced strength degradation after peak load, with both curves (see Figure III.16) closely aligning with the experimental results in the softening range.

Given that the default value of 1.16 produced a response consistent with the experimental data while maintaining a realistic representation of concrete behavior, this value was deemed appropriate and adopted for the subsequent analyses.

Furthermore, a sensitivity analysis was performed to determine the appropriate value for the eccentricity (ε), considering values of 0.05, 0.08, 0.1, and 0.14. The results indicated that variations in eccentricity had a negligible effect on the overall response. Therefore, the default value of 0.1 was selected for use in the subsequent analyses.

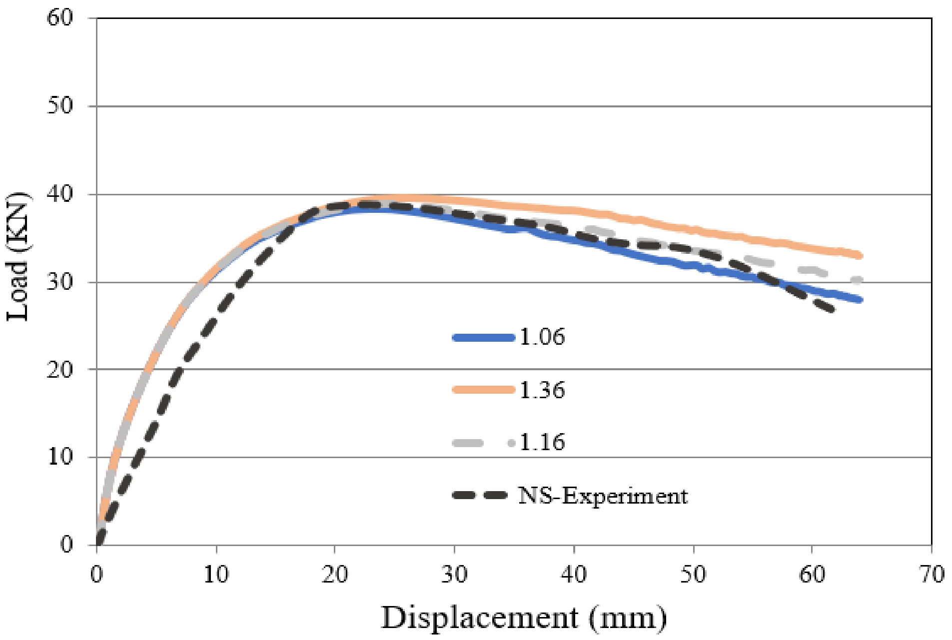

Figure III.16. Effect of σ_{c0}/σ_{b0} ratio on load displacement behavior.

The sensitivity analysis revealed that, of all the CDP model parameters examined, the dilation angle and K_c have the most significant influence and should be carefully calibrated for accurate results. however, using the default for K_c produced better outcomes. In contrast, the other parameters have a lesser impact and can be kept at their default settings. The final selected values for each parameter, as determined in this study, are summarized in Table III-2.

Table III-2. Summary of selected plasticity parameters of the CDP model.

Material parameter	Value
Dilation angle (ψ)	40° (calibrated)
$\boldsymbol{K_c}$	0.667 (default)
$\boldsymbol{\sigma_{c0}/\sigma_{b0}}$	1.16 (default)
eccentricity ε	0.1 (default)

III.6.2 CFRP COMPOSITE MODELLING

III.6.2.1 ELASTIC BEHAVIOR

CFRP composites are inherently anisotropic materials due to their heterogeneous structure, which consists of continuous carbon fibers embedded within a polymer matrix. This anisotropy results in directional dependence of their mechanical properties. Figure III.17 illustrates a schematic representation of a unidirectional lamina, serving as the fundamental unit in composite modeling. The coordinate system used for modeling aligns with the principal material axes:

- **Direction 1** corresponds to the fiber direction, which exhibits the highest stiffness and strength due to the continuous alignment of fibers.
- **Directions 2 and 3** Orthogonal to Direction 1, representing the transverse and through-thickness directions, respectively.

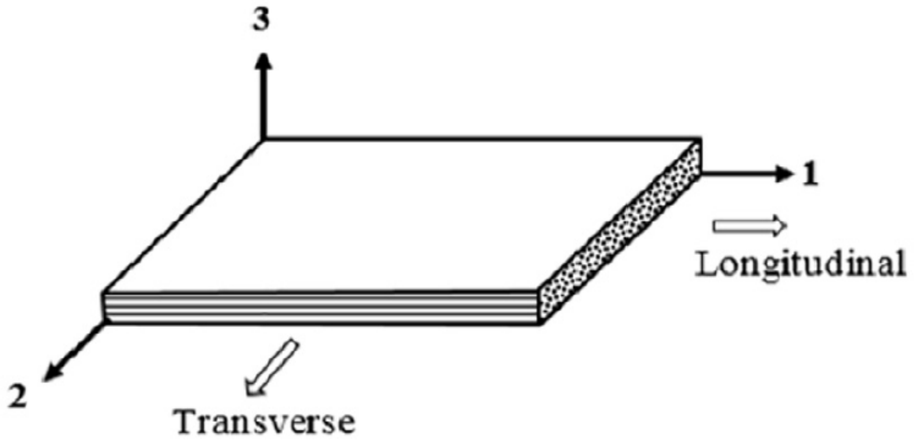

Figure III.17. Schematic of unidirectional FRP lamina [33].

Unidirectional CFRP composites are classified as transversely isotropic materials. This classification means that while mechanical properties vary significantly along the fiber direction (Direction 1), they remain isotropic within the plane normal to the fiber direction (the 23-plane).

In ABAQUS, several approaches are available for defining the elastic behavior of CFRP materials:

1. **Lamina Option**: Defines an orthotropic material under plane stress conditions.
2. **Engineering Constants Option**: Defines an orthotropic material in a 3D stress state.
3. **Direct Stiffness Matrix Specification**: Involves directly specifying the elastic stiffness matrix.

For the engineering constants approach, the inverse form of Hooke's law relates strain components to stress components via the compliance matrix [S], is depicted in Eq. III-32. In many structural analyses involving thin CFRP laminates, a plane stress condition is assumed. This simplification neglects the out-of-plane stress component ($\sigma_{33} = 0$), which is valid when the laminate thickness is small relative to its other dimensions. Under plane stress conditions, the compliance matrix reduces as shown in Eq. III-33. The required elastic properties are the longitudinal modulus (E_1), transverse modulus (E_2), major Poisson's ratio (ν_{12}), and in-plane shear modulus (G_{12}). The shear moduli (G_{13} and G_{23}) may also be necessary to model transverse shear deformation, particularly when using shell elements that account for out-of-plane effects [38].

$$\begin{Bmatrix} \varepsilon_{11} \\ \varepsilon_{22} \\ \varepsilon_{33} \\ \gamma_{12} \\ \gamma_{13} \\ \gamma_{23} \end{Bmatrix} = \begin{bmatrix} 1/E_1 & -\nu_{21}/E_1 & -\nu_{31}/E_1 & 0 & 0 & 0 \\ -\nu_{12}/E_2 & 1/E_2 & -\nu_{32}/E_2 & 0 & 0 & 0 \\ -\nu_{13}/E_3 & -\nu_{23}/E_3 & 1/E_3 & 0 & 0 & 0 \\ 0 & 0 & 0 & 1/G_{12} & 0 & 0 \\ 0 & 0 & 0 & 0 & 1/G_{13} & 0 \\ 0 & 0 & 0 & 0 & 0 & 1/G_{23} \end{bmatrix} \begin{Bmatrix} \sigma_{11} \\ \sigma_{22} \\ \sigma_{33} \\ \sigma_{12} \\ \sigma_{13} \\ \sigma_{23} \end{Bmatrix} \qquad \text{III-32}$$

In this study, the Lamina option in ABAQUS was utilized to define the elastic behavior of the CFRP material. The mechanical properties were specified in the local coordinate system defined by the user, as discussed earlier. The mechanical properties of the cured laminate (a combination of dry CFRP sheets and epoxy adhesive) were determined through tensile coupon tests conducted on cured laminates, with the results summarized in Table III-3 [54]. Additionally, the mechanical properties of basalt FRP, examined in the parametric study is also summarized in Table III-3 [54].

$$\begin{Bmatrix} \varepsilon_{11} \\ \varepsilon_{22} \\ \gamma_{12} \end{Bmatrix} = \begin{bmatrix} 1/E_1 & -\nu_{12}/E_1 & 0 \\ -\nu_{21}/E_2 & 1/E_2 & 0 \\ 0 & 0 & 1/G_{12} \end{bmatrix} \begin{Bmatrix} \sigma_{11} \\ \sigma_{22} \\ \sigma_{12} \end{Bmatrix} \qquad \text{III-33}$$

Table III-3. Orthotropic mechanical properties of cured CFRP and BFRP laminates used in this study [54].

Property	Young's modulus (GPa)			Poisson's ratio			Shear modulus (GPa)		
Designation	E_1	E_2	E_3	ν_{12}	ν_{13}	ν_{23}	G_{12}	G_{13}	G_{23}
Value (CFRP)	46.053	3.224	3.224	0.28	0.28	0.42	1.259	1.259	1.135
Value (BFRP)	24.981	1.749	1.749	0.15	0.15	0.21	0.760	0.760	0.723

III.6.2.2 CFRP DAMAGE MODELLING

CFRP composites typically exhibit an elastic-brittle behavior, meaning they fail suddenly without significant plastic deformation. Consequently, plasticity effects can be neglected in their failure modeling. In this study, damage initiation and evolution in CFRP were modeled using the Hashin failure criteria [55], which are readily available in ABAQUS.

The Hashin failure criteria are widely used to predict different damage modes in FRP composites, including CFRP. This model differentiates between fiber and matrix failures, providing a more detailed and realistic representation of damage mechanisms. In ABAQUS, the Hashin damage model can be directly implemented via the graphical user interface (GUI), simplifying its application in finite element analysis.

The Hashin model is based on two key concepts:

- **Damage Initiation** refers to the onset of material degradation under specific local stress states.
- **Damage Evolution** describes how damage progresses once initiated, often based on energy dissipation or degradation of stiffness.

The Hashin criteria classify damage into four distinct failure modes:

Fiber tension: $(\hat{\sigma}_{11} \geq 0)$;

$$F_f^t = \left(\frac{\hat{\sigma}_{11}}{X^t}\right)^2 + \alpha\left(\frac{\hat{\tau}_{12}}{S^l}\right)^2 \qquad \text{III-34}$$

Fiber compression: $(\hat{\sigma}_{11} < 0)$;

$$F_f^c = \left(\frac{\hat{\sigma}_{11}}{X^c}\right)^2 \qquad \text{III-35}$$

Matrix tension : $(\hat{\sigma}_{22} \geq 0)$;

$$F_m^t = \left(\frac{\hat{\sigma}_{22}}{Y^t}\right)^2 + \left(\frac{\hat{\tau}_{12}}{S^l}\right)^2 \qquad \text{III-36}$$

Matrix compression : $(\hat{\sigma}_{22} < 0)$;

$$F_m^c = \left(\frac{\hat{\sigma}_{22}}{2S^t}\right)^2 + \left[\left(\frac{Y^c}{2S^t}\right)^2 - 1\right]\left(\frac{\hat{\sigma}_{22}}{Y^c}\right) + \left(\frac{\hat{\tau}_{12}}{S^l}\right)^2 \qquad \text{III-37}$$

In the above equations:

X^t, X^c : Tensile and compressive strengths in the fiber direction.

Y^t, Y^c: Tensile and compressive strengths perpendicular to the fiber direction.

S^l, S^t: longitudinal and transverse shear strengths.

α : is a coefficient that determines the contribution of the shear stress to the fiber tensile initiation criterion was taken 1 as suggested by Hashin. Z [55].

$\hat{\sigma}_{11}$, $\hat{\sigma}_{22}$, and $\hat{\tau}_{12}$ are component of the effective stress tensor, $\hat{\sigma}$, that is used to evaluate the initiation criteria and which is computed from Eq. III-38.

$$\hat{\sigma} = M\sigma \qquad \text{III-38}$$

Here, σ represents the nominal stress, and M denotes the damage operator, as presented in Eq. III-39.

$$M = \begin{bmatrix} \frac{1}{(1-d_f)} & 0 & 0 \\ 0 & \frac{1}{(1-d_m)} & 0 \\ 0 & 0 & \frac{1}{(1-d_s)} \end{bmatrix} \qquad \text{III-39}$$

Here, d_f, d_m, and d_s are internal damage variables representing fiber, matrix, and shear damage, respectively. These variables are derived from the mode-specific damage variables d_f^t, d_f^c, d_m^t, and d_m^c, which correspond to the four failure modes previously discussed, as follows:

$$d_f = \begin{Bmatrix} d_f^t & if\ \hat{\sigma}_{11} \geq 0 \\ d_f^c & if\ \hat{\sigma}_{11} < 0 \end{Bmatrix} \qquad \text{III-40}$$

$$d_m = \begin{Bmatrix} d_m^t & if\ \hat{\sigma}_{22} \geq 0 \\ d_m^c & if\ \hat{\sigma}_{22} < 0 \end{Bmatrix} \qquad \text{III-41}$$

$$d_s = 1 - \left(1 - d_f^t\right)\left(1 - d_f^c\right)(1 - d_m^t)(1 - d_m^c) \qquad \text{III-42}$$

Figure III.18 presents a comparison between the experimental and numerical results for cases with and without the Hashin failure criteria. The simulation without Hashin criteria shows relatively good agreement with the experiment in terms of peak load. However, the post-peak response exhibits less degradation compared to the experimental results. The absence of Hashin criteria resulted in no damage occurring in the CFRP composites, leading to an unrealistic solution and an overestimation of the post-peak response. As observed in Davodikia's experimental study [27], significant damage occurred in the CFRP composites during testing, particularly after the peak load. The simulation with Hashin criteria, on the other hand, demonstrates a more pronounced decrease in load after the peak, effectively capturing the initiation and evolution of damage in the CFRP material. Therefore, the Hashin failure criteria were applied in all subsequent analyses to ensure a more accurate representation of the CFRP behavior.

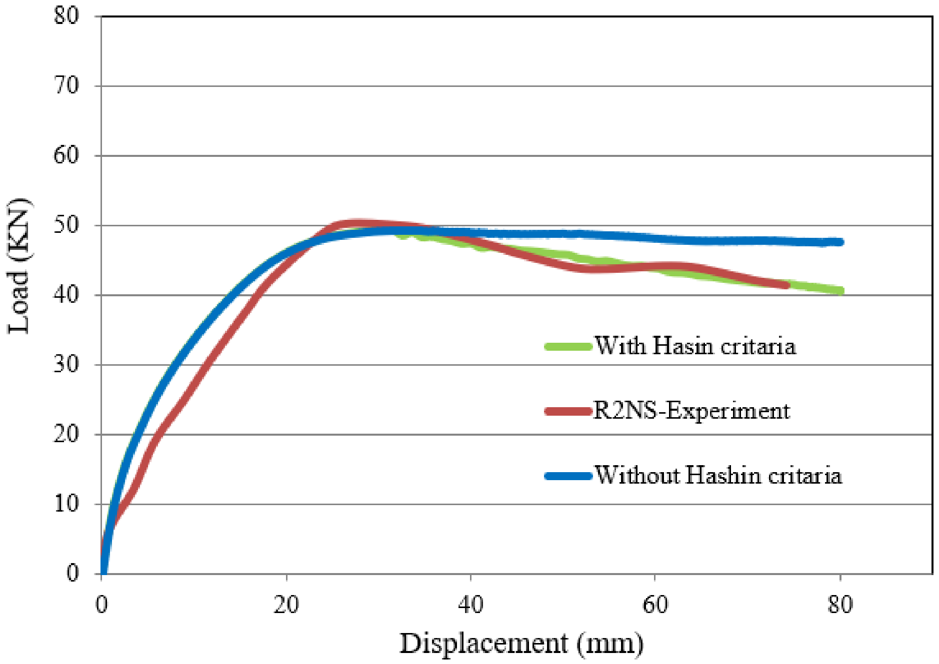

Figure III.18. Comparison of load-displacement curves for experimental and numerical models with and without Hashin failure criteria.

III.6.3 STEEL REINFORCEMENT MODELLING

In this study, an isotropic modelling approach was adopted to represent the steel reinforcement and the loading steel plate. The steel reinforcement was characterized by bilinear stress-strain behavior, with mechanical properties derived from experimental test data (Table III-4 [27]). Key parameters, such as yield strength, ultimate strength, and strain-hardening modulus, were incorporated to capture the material's response under load.

The loading steel plate was modeled as a linear elastic material with a Young's modulus of 200 GPa and a Poisson's ratio of 0.3, reflecting its expected behavior during analysis. Figure III.19 illustrates the bilinear stress-strain behavior of the steel reinforcement, highlighting its yield point and strain-hardening characteristics.

Table III-4. Mechanical properties of steel reinforcement [27].

Bar diameter (mm)	14	10
Density (t/mm^3)	7.8×10^{-9}	7.8×10^{-9}
Poisson's ratio	0.3	0.3
Young's modulus (GPa)	200	200
Yield strength (MPa)	470	405
Ultimate strength (MPa)	690	670
Yield strain (%)	0.2	0.18
Ultimate strain (%)	15	16

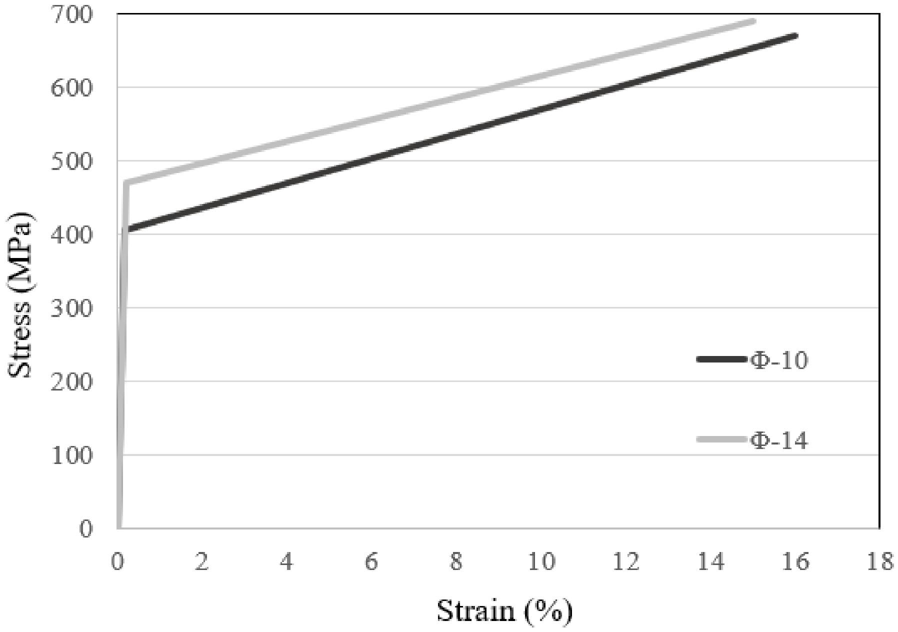

Figure III.19. Bilinear stress-strain behavior of steel reinforcement.

III.6.4 UTILIZED ELEMENTS.

The geometric properties of the model were designed to closely match those of the experimental test specimens. To simulate the different components of the model, various element types were utilized. The concrete components and the steel loading plate were modeled using solid (continuum) elements to accurately capture their three-dimensional geometry and stress distribution. ABAQUS offers various 3D solid elements, including linear and quadratic hexahedral, tetrahedral, and wedge-shaped elements, suitable for modeling concrete structures. In this study, the 4-node linear tetrahedral element (C3D4) was selected for meshing both the concrete and the steel plate. Each node of the C3D4 element has three translational degrees of freedom, enabling displacement along the X, Y, and Z axes. This element type has been shown to effectively model RC beams, providing results that closely align with experimental findings [56].

Steel reinforcement bars are typically modeled using one-dimensional elements due to their relatively small cross-sectional dimensions compared to their length. ABAQUS provides several element types for modeling steel reinforcements, primarily truss and beam elements. Truss elements, such as T3D2 (a 2-node linear displacement truss), are designed to deform solely through axial stretching, making them suitable for modeling reinforcement that primarily resists tensile forces. Alternatively, Timoshenko beam elements like B31 (a linear Timoshenko beam) and B32 (a quadratic Timoshenko beam) account for both bending and transverse shear deformation, providing a more comprehensive representation of flexural behavior.

A study by Gebreyohaness [57] evaluated the performance of these elements for modeling steel reinforcement. The analysis revealed that using beam elements (B31 and B32) significantly overestimated the post-peak response and strength degradation. In contrast, the T3D2 truss element produced more accurate results with lower computational cost. Based on these findings, the T3D2 element was adopted in this study to model the steel reinforcement.

For the CFRP composites, four-node reduced-integration shell elements (S4R) were employed to effectively simulate their behavior. Figure III.20 shows the representation of utilized elements.

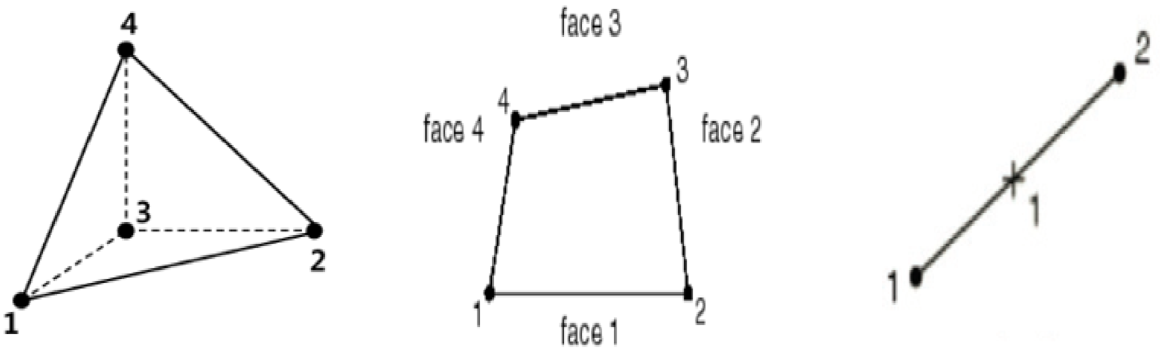

(a) (b) (c)

Figure III.20. Utilized elements. (a) C3D4 4-node linear tetrahedron [38]; (b) S4R 4-node shell element; (c) T2D3 2-node truss element.

III.6.5 INTERACTIONS AND MESHING

This study utilized the embedded element technique to simulate the transfer of forces between the steel reinforcement and the surrounding concrete. This method assumes that the embedded region (steel reinforcement) moves and deforms with the host region (concrete). Consequently, the translational degrees of freedom of the embedded nodes are constrained to the interpolated values of the corresponding degrees of freedom of the host elements. This approach represents a perfect bond at the interface, thereby simplifying the interaction by neglecting bond-slip effects.

Given the high bond strength achieved through the grooving method, the interaction between the CFRP composites and the concrete substrate was assumed to be a perfect bond. To simulate this interaction, a tie constraint was applied to ensure no relative movement between the two surfaces. Similarly, the interface between the steel loading plate and the concrete was also modelled using the same perfect bond assumption.

A 45 mm thick steel plate was used at the beam tip to apply the load. Following a detailed mesh sensitivity analysis, a global mesh size of approximately 50 mm was adopted for the concrete and steel reinforcements, while a finer mesh size of 25 mm was applied to the CFRP composites to capture their detailed response accurately.

III.6.6 LOADING AND BOUNDARY CONDITIONS

Figure III.21 illustrates the geometric configuration of the R2NS model used for verification analysis. To accurately replicate the boundary conditions of the experimental setup, reference points were established at both ends of the column. These points were coupled to the column surfaces using a coupling constraint to ensure consistent boundary interactions.

Boundary conditions were applied to represent realistic test scenarios. The top surface of the column was restrained in the X and Z directions ($U_X = U_Z = 0$), mimicking a roller support, while the bottom surface was fixed in the X, Y, and Z directions ($U_X = U_y = U_z = 0$) to simulate a pinned support. Additionally, to eliminate lateral movement, the beam's free end was restricted in the Z direction.

The loading process involved two stages. Initially, a uniform axial pressure of 2.8 MPa, equivalent to an axial force of 175 KN, was applied to the column's upper surface and sustained throughout the analysis. Subsequently, a monotonic vertical displacement was imposed at the beam's free end through a reference point positioned at the center of the steel loading plate. By applying monotonic rather than cyclic loading, the analysis was streamlined, focusing solely on the primary response of the structure. This simplification aligns with methodologies frequently adopted in previous numerical studies on RC beam-column joints [58-61].

The setup and details of the boundary conditions and loading sequence are illustrated in Figure III.21.

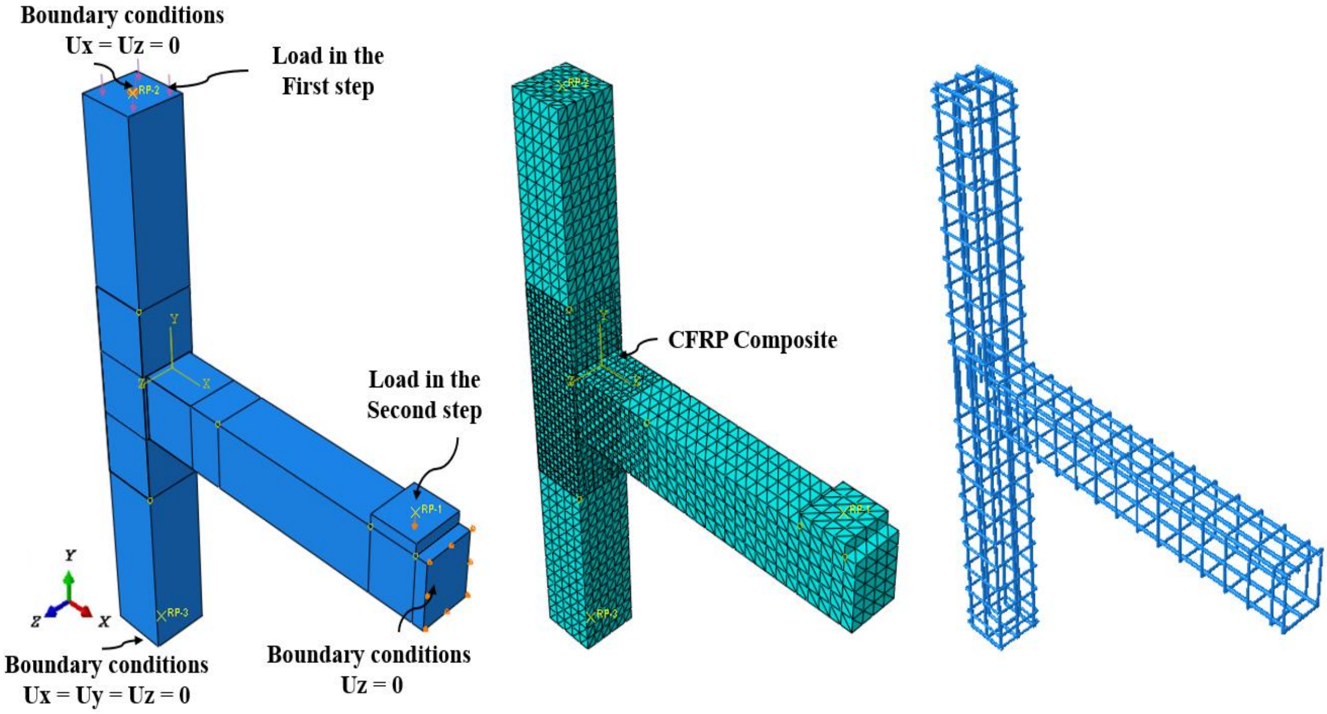

(a): Applied loads (b): Meshing (c): Reinforcement

Figure III.21. Details and geometric representation of R2NS model.

III.7 ANALYSIS VERIFICATION

Finite Element (FE) analyses were conducted on all test specimens after calibrating the model with representative experimental data. This calibration involved identifying optimal mesh sizes, material parameters, and loading rates through a series of iterative simulations. The accuracy of the numerical model was validated by comparing its predictions with experimental results in terms of peak loads, load-displacement responses, and observed failure modes.

The experimental hysteresis curves were converted into envelopes, commonly referred to as pushover curves. These envelopes were compared with the beam load-displacement curves derived from numerical simulations. A detailed comparison of the load-displacement responses for three selected specimens (S, NS, and R2NS) is presented in Figure III.22. The numerical analysis predicted peak loads of 49.60 kN, 39.01 kN, and 49.15 kN for the S, NS, and R2NS specimens, respectively. These values were compared to the experimental peak loads of 52.67 kN, 38.00 kN, and 50.46 kN for the same specimens. The resulting percentage errors in predicting the peak loads were calculated as 6.18%, 2.65%, and 2.66% for S, NS, and R2NS, respectively. These results demonstrate the ability of the numerical model to accurately replicate experimental behavior, particularly in terms of peak loads. Table III-5 presents a comparison between the predicted numerical and experimental peak loads for the three modeled specimens

Overall, the load-displacement curves produced by the FEA showed strong agreement with the experimental data, especially in the nonlinear phase where the model effectively captured the post-peak strength degradation as lateral displacement increased. However, the numerical initial stiffness obtained for the NS and R2NS specimens was slightly higher than that observed experimentally. This discrepancy is acceptable when considering minor differences between the input and measured material properties, such as Young's modulus of concrete and steel reinforcement, which were estimated based on empirical equations rather than direct measurements. Moreover, the assumption of a perfect bond between concrete and steel reinforcement, along with possible material inconsistencies during the experimental process, may have contributed to the observed discrepancies in the results [45,61].

Table III-5. Comparison of Experimental and numerical peak loads.

Specimen	Experimental (kN)	Numerical (kN)	Difference (%)
NS	38.00	39.01	2.65
S	52.67	49.60	6.18
R2NS	50.46	49.15	2.66

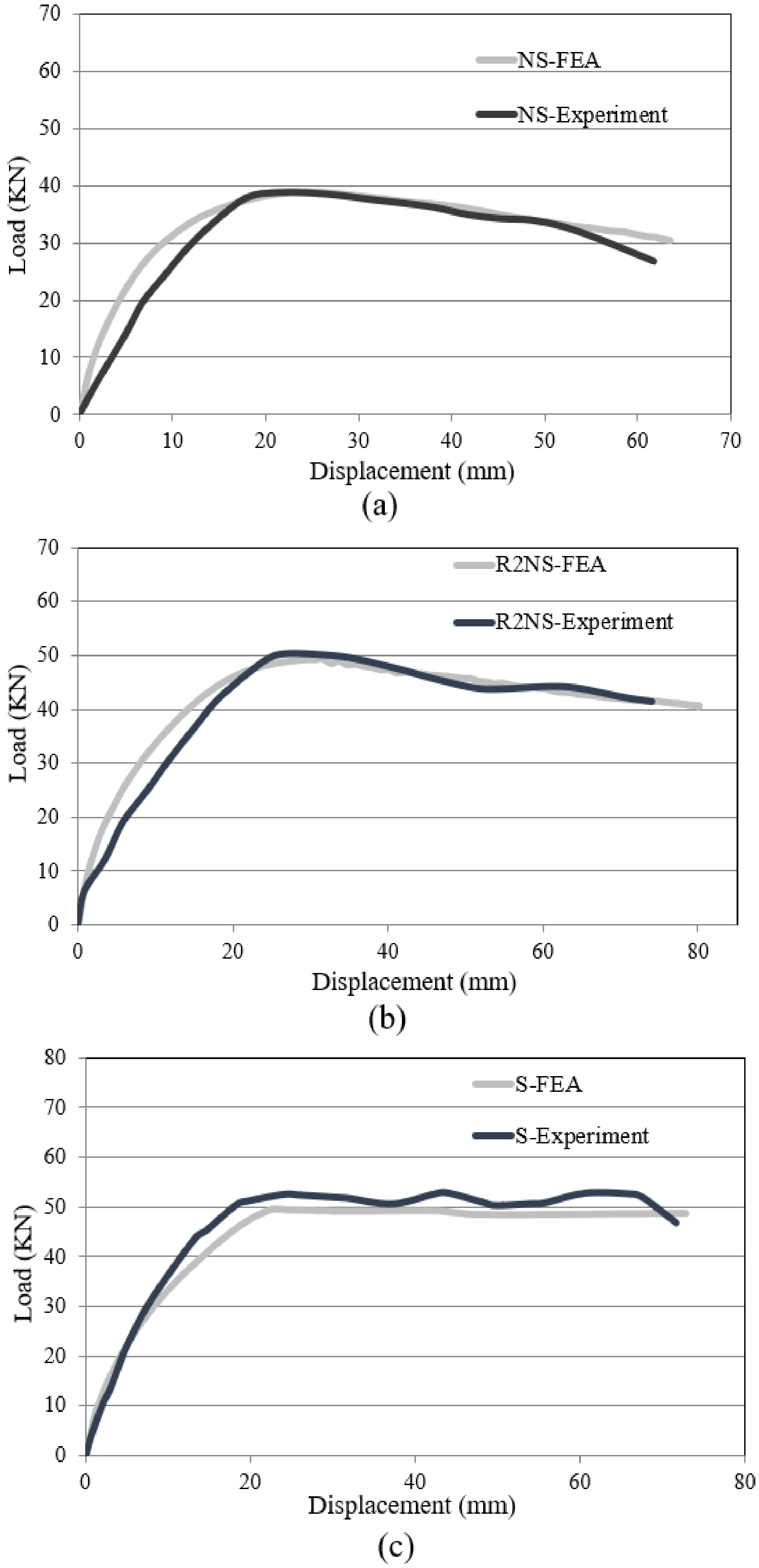

Figure III.22. Comparison of the beam load displacement curves. Numerical analysis vs. Experimental test.

Figure III.23 compares the crack patterns of numerical and experimental specimens at peak loads. The tensile damage distribution in the numerical model serves as a key indicator for evaluating failure mechanisms [58].

For the NS (bare) specimen, the FE results show that flexural cracks first develop in the beam and then extend into the joint core, where diagonal shear cracks begin to form. As loading increases, the number of shear cracks grows, leading to brittle failure due to the lack of horizontal reinforcement in the joint core. This failure mode is consistent with experimental observations.

In the S (seismically detailed) specimen, the first flexural cracks appear in the beam near the column face. Some cracks propagate into the joint core, but their width remains smaller compared to the NS specimen. With increasing load, additional bending-induced cracks develop in the beam. The specimen ultimately fails with plastic hinge formation in the beam, indicating improved ductility.

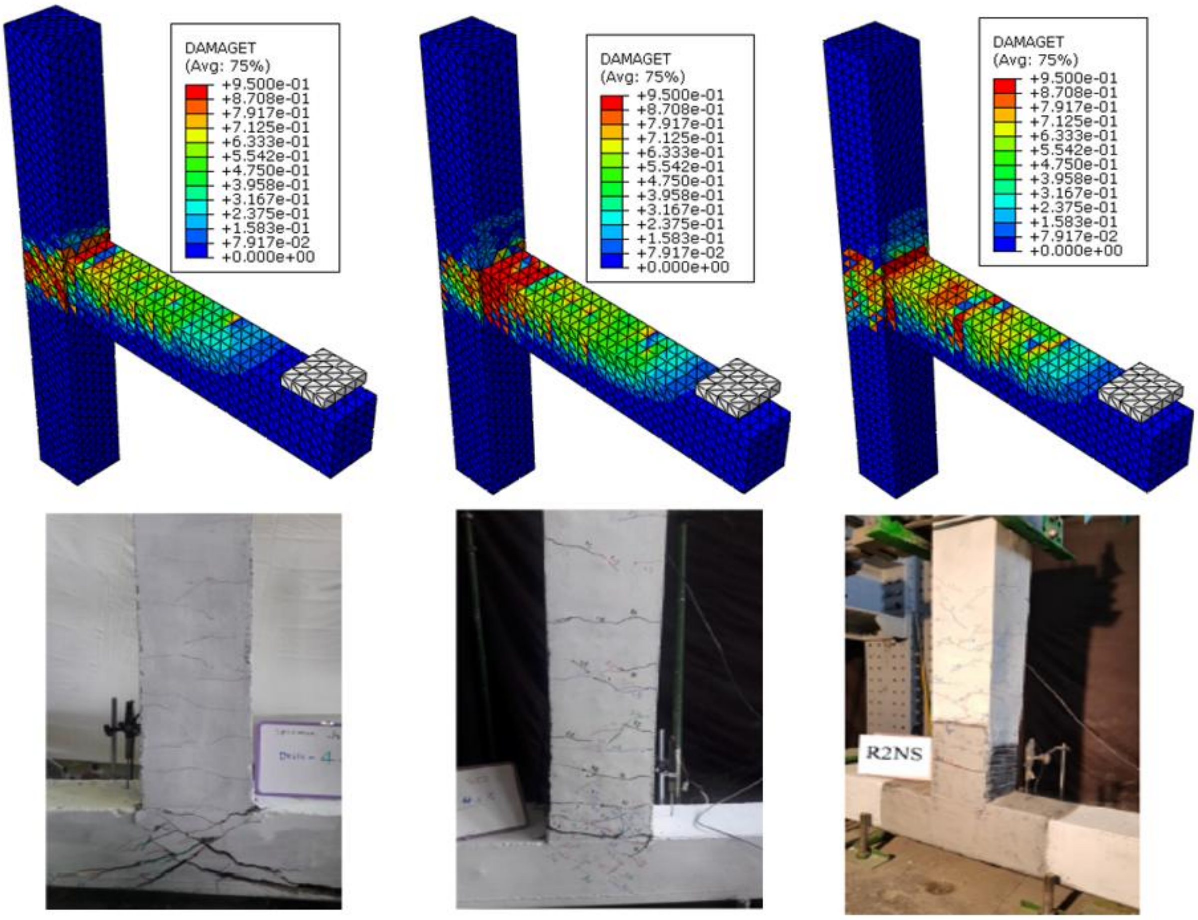

(a): NS (b): S (c): R2NS

Figure III.23. Comparison of crack patterns in modeled specimens: Numerical vs. Experimental results.

For the R2NS (retrofitted) specimen, joint core damage is significantly reduced due to CFRP strengthening. Instead, cracks are more distributed along the beam, particularly near the column face and near the CFRP cut-off point. This suggests that CFRP retrofitting enhances shear resistance and shifts damage away from the critical joint region.

Overall, the FE model accurately predicts the crack patterns and damage distribution observed in the experiments, demonstrating its reliability in simulating the failure behavior of RC BCJs.

III.8 CONCLUSION

This chapter presented a detailed numerical validation of non-seismically designed RC BCJs retrofitted with CFRP composites using the GM. The FEA was conducted using the explicit solver in ABAQUS, which was chosen to effectively handle the nonlinear behavior of the joints while avoiding the convergence issues commonly encountered in implicit solver. The modeling approach accounted for material nonlinearities, contact interactions, and progressive damage mechanisms, ensuring an accurate representation of structural response.

The numerical models demonstrated good agreement with experimental findings in terms of load-displacement behavior, stiffness, peak load, and failure modes. However, minor discrepancies were observed in the predicted initial stiffness, primarily due to differences between the assumed and actual material properties, such as the Young’s modulus of concrete and steel reinforcement, which were estimated using empirical equations. Despite these variations, the overall numerical predictions successfully captured the key behavioral characteristics of the retrofitted joints. Therefore, the validated FE model can be reliably used to conduct a parametric study investigating the effects of various parameters on the behavior of retrofitted joints.

Chapter ***IV****:*

Parametric Study

Chapter IV: Parametric Study

IV.1 INTRODUCTION

The behavior of BCJs is governed by several structural and material parameters, which play a critical role in defining their response under loading. This is particularly significant for retrofitted joints, where these parameters influence both the performance and the efficiency of the adopted retrofitting technique. Understanding the interaction between these factors is essential to optimize retrofitting strategies for RC joints, especially those with deficiencies.

This chapter presents a comprehensive parametric study that evaluates the effects of key parameters on the retrofitting technique investigated in this research, the use of CFRP composites bonded to the concrete substrate through the grooving method. The validated numerical model is employed to systematically analyze the influence of four critical parameters: column axial load ratio, beam longitudinal reinforcement ratio, and joint aspect ratio in conjunction with joint transverse reinforcement. These parameters were selected due to their substantial impact on the mechanical behavior of RC joints, particularly in terms of load-carrying capacity, shear strength of the joint, and failure mechanisms.

IV.2 EFFECT OF COLUMN AXIAL LOAD RATIO

The column axial load ratio measures the proportion of the axial load applied to a column relative to its nominal axial load capacity. This parameter significantly affects the structural performance of BCJs, particularly in retrofitted systems. The column axial stress, σ_N, was calculated by dividing the applied axial load by the column cross-sectional area. The investigated axial stress values ranged from 0, 2.83, 5.66, and 8.49 MPa, corresponding to axial load ratios of 0, $0.1A_g f_c'$, $0.2A_g f_c'$, and $0.3A_g f_c'$, where A_g is the column cross-sectional area, and f_c' is the compressive strength of concrete. These ratios were chosen because they are known to induce shear failure in un-retrofitted joints, making them suitable for evaluating the effectiveness of retrofitting techniques. A total of eight models were analyzed in this section for both retrofitted and un-retrofitted joints.

Figure IV.1 depicts the relationship between the lateral force and displacement of the beam under different axial load ratios. Meanwhile, Table IV-1 provides a detailed summary of the numerical results, including the peak load (P_u), the corresponding displacement at peak load (Δ_u), and the computed joint shear strength (ν_j) for each axial load ratio.

Table IV-1: Numerical results for varying axial load level.

Ratio	(P_u) **kN**		$(\varDelta_u)$ **(mm)**		ν_j **(MPa)**		**Increase in** P_u **(%)**
	Control	**Retrofitted**	**Control**	**Retrofitted**	**Control**	**Retrofitted**	
0.0	37.39	47.35	30.32	33.42	4.27	5.41	26.64
0.1	39.01	49.15	24.85	31.08	4.46	5.62	25.99
0.2	42.06	51.52	21.63	25.41	4.80	5.89	22.49
0.3	47.00	54.82	17.05	23.52	5.37	6.26	16.63

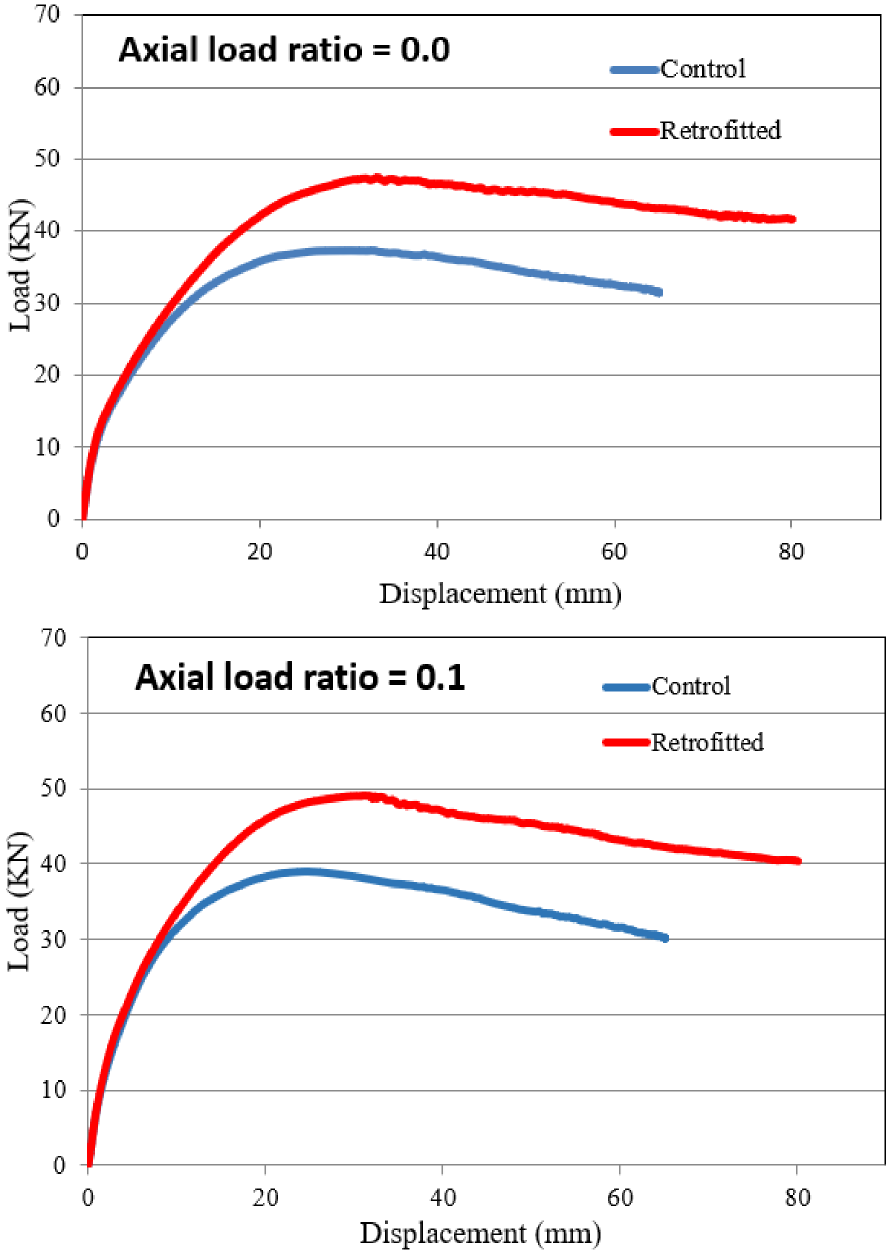

Figure IV.1. The influence of varying column axial load ratios on the load-displacement behavior.

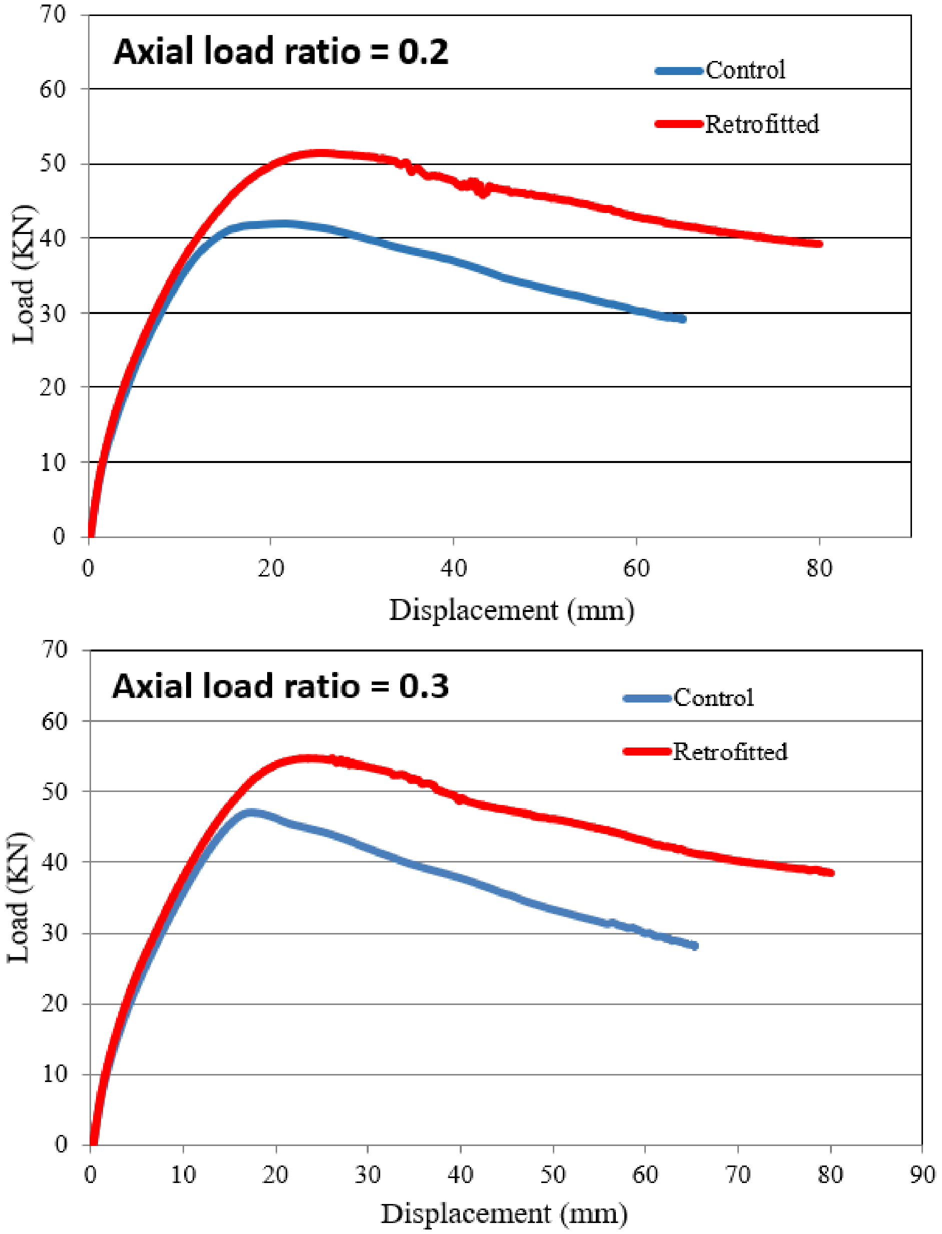

Figure IV.1. Continued.

An analysis of Figure IV.1 and Table IV-1 highlights key trends in the behavior of retrofitted joints under varying axial load conditions. The results indicate that increasing the axial load ratio from 0.0 to 0.3 leads to an approximate 25% rise in the load-carrying capacity of the control joints, suggesting that the axial load contributes to enhancing the shear strength of the joint core. In the case of CFRP-retrofitted specimens, the increase in load-carrying capacity is relatively lower, around 16%, which implies that the additional confinement provided by the CFRP sheets enhances shear strength and reduces the impact of axial loads.

Furthermore, the comparison of peak loads between retrofitted and control specimens shows an increase of 26.64%, 25.99%, 22.49%, and 16.63% for axial load ratios of 0.0, 0.1, 0.2, and 0.3, respectively. These findings suggest that CFRP composites play a significant role in enhancing shear performance; however, their effectiveness diminishes with higher axial loads. This trend can be attributed to the axial load's contribution to joint strength, which limits the additional gains provided by CFRP retrofitting. It is important to note that these observations are based on control specimens that primarily failed due to joint shear failure.

The most significant improvement in peak load (26.64%) was observed in the absence of axial load, highlighting the critical role of CFRP composites in shear retrofitting. Under these conditions, the CFRP fully engaged in resisting shear forces within the joint core without the supplementary confinement provided by axial load. This effect was particularly pronounced in joints with lower initial shear strength, where CFRP retrofitting played a crucial role in confining the panel zone against lateral shear forces.

These findings emphasize the importance of CFRP composites in retrofitting applications where the existing shear capacity is insufficient. Without axial load, the CFRP contribution to shear resistance becomes more pronounced, making it an effective strengthening solution for non-seismically designed joints.

The lower percentage increase in peak load observed in retrofitted joints at higher axial load (16.63% at 0.3) suggests a diminishing effect of CFRP retrofitting as the axial load increases. As the axial load increases, the joint's shear strength naturally improves, reducing the dependence on the additional confinement and tensile reinforcement provided by the CFRP.

Figure IV.2 presents the tensile damage contours of retrofitted joints under different axial load levels. The figure illustrates that as the column axial load increases, the distribution of tensile damage shifts from the joint region to the beam. This redistribution suggests that higher axial loads provide greater confinement, effectively restricting the formation of diagonal shear cracks within the joint core. In contrast, when no axial load is applied, as shown in Figure IV.2 (a), extensive diagonal shear cracks develop in the joint area. This indicates that, in the absence of axial load, the CFRP composites play a crucial role in reinforcing the joint by fully engaging in resisting shear forces and improving structural integrity.

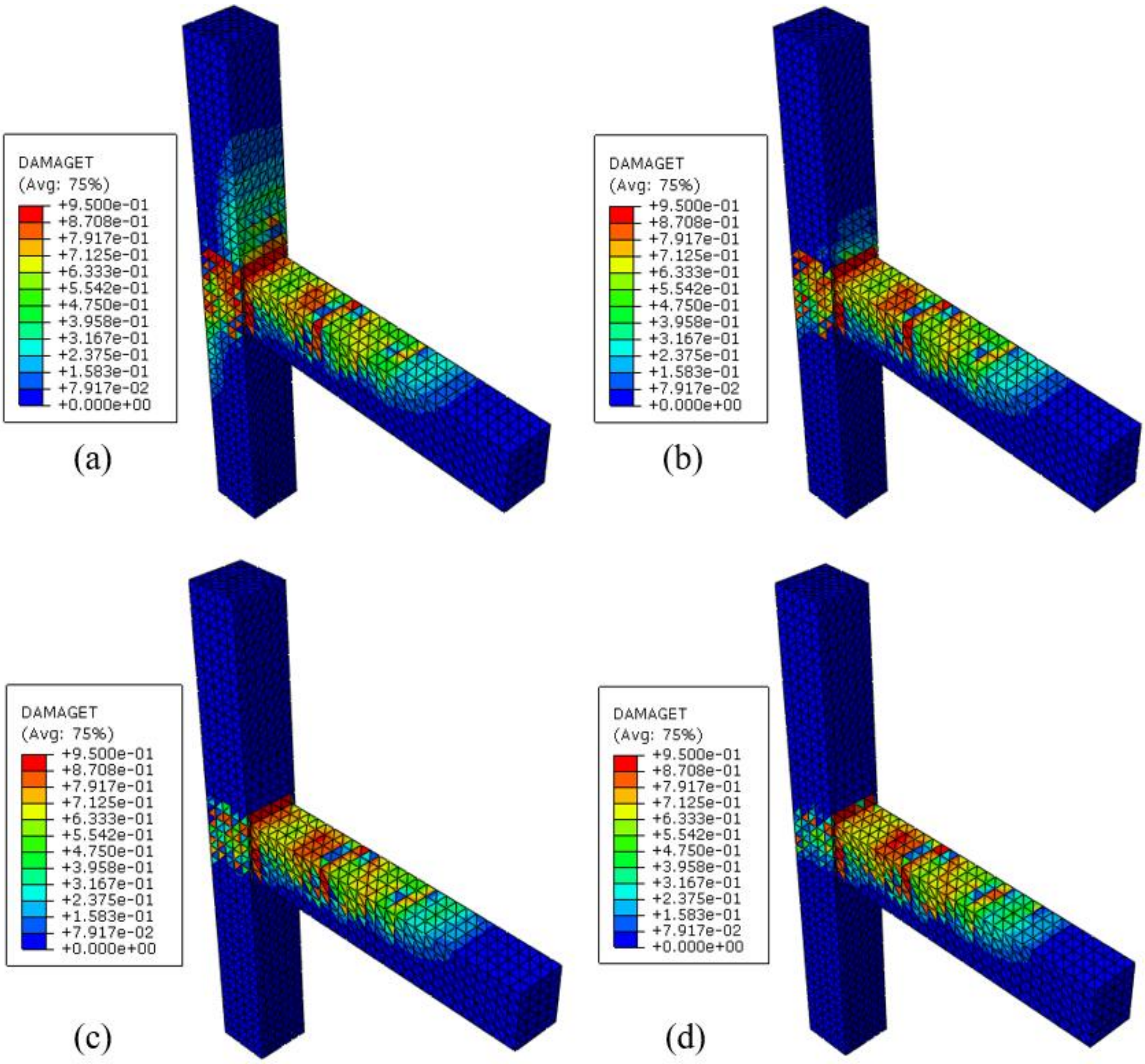

Figure IV.2. Tensile damage patterns in joints under varying column axial load ratios.

IV.3 EFFECT OF BEAM LONGITUDINAL REINFORCEMENT RATIO

In addition to the column axial load ratio, this section investigates the effect beam longitudinal reinforcement ratio (ρ_b), which were varied as 0.99%, 1.44%, 1.95%, and 2.55%. The variation in (ρ_b) was achieved by using rebars with the same mechanical properties but different diameters.

A total of eight BCJ specimens were analyzed in this section, as summarized in Figure IV.**3.** Continued.

Table IV-2. Figure IV.3 depicts the relationship between the lateral force and displacement of the beam under different beam reinforcement ratios. Meanwhile, Figure IV.**3.** Continued.

Table IV-2 provides a detailed summary of the numerical results.

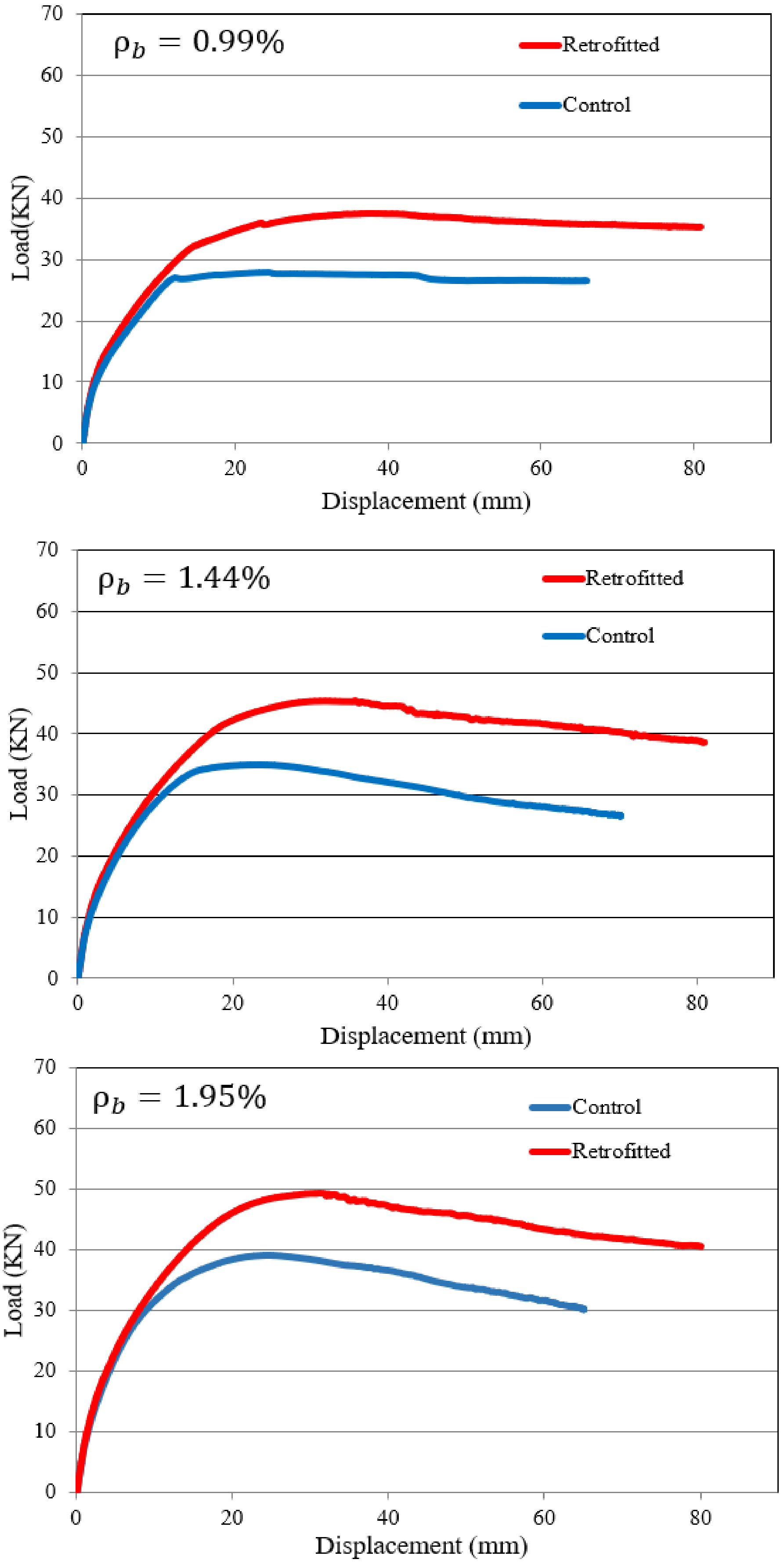

Figure IV.3. The influence of varying beam longitudinal reinforcement ratios on the load-displacement behavior.

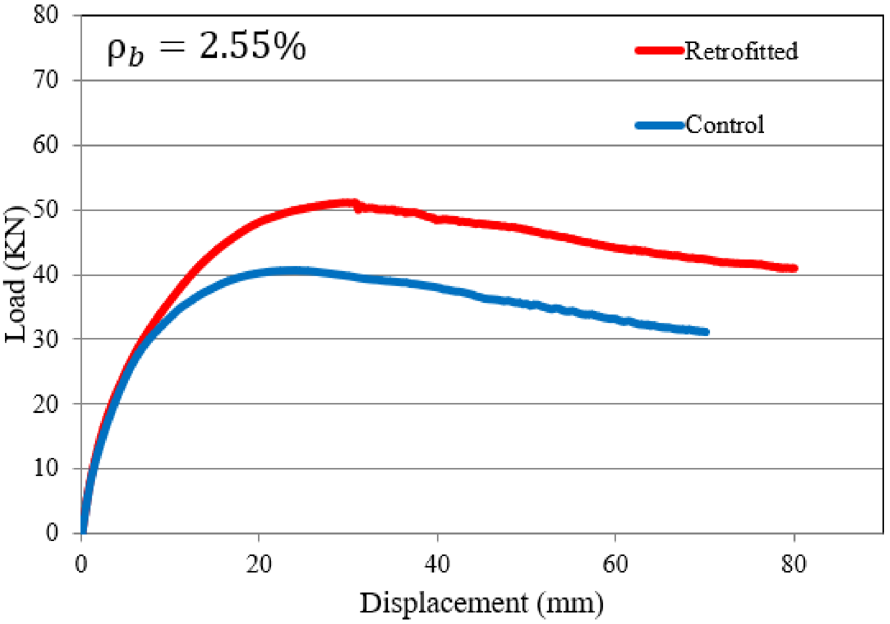

Figure IV.3. Continued.

Table IV-2. Numerical results for varying beam longitudinal reinforcement ratio.

$\rho_b(\%)$	(P_u) kN		(Δ_u) (mm)		ν_j (MPa)		Increase in P_u (%)
	Control	**Retrofitted**	**Control**	**Retrofitted**	**Control**	**Retrofitted**	
0.99%	27.87	37.54	24.51	38.03	3.18	4.29	34.69
1.44%	35.01	45.33	23.62	32.07	4.00	5.18	29.47
1.95%	39.01	49.15	24.85	31.07	4.46	5.62	25.99
2.55%	40.70	51.03	24.06	29.60	4.65	5.83	25.38

The analysis of Figure IV.3 and Figure IV.**3.** Continued.
Table IV-2 indicates a significant improvement in the load-carrying capacity of un-retrofitted joints as the beam reinforcement ratio (ρb) increases from 0.99% to 2.55%, resulting in an approximate gain of 46%. This enhancement is primarily attributed to the increased flexural strength of the beam, allowing it to sustain higher loads. As the reinforcement ratio increases, the beam's resistance to bending moments improves, leading to a substantial increase in overall load capacity. This effect is particularly evident in cases where flexural failure was observed at lower reinforcement ratios.

In contrast, joints retrofitted with CFRP composites exhibited a slightly lower increase in load-carrying capacity, approximately 36%. This suggests that while both scenarios experienced improvements, the effect of increasing ρb was less pronounced in retrofitted joints because the CFRP composites already enhance the beam's flexural capacity.

Moreover, the peak load of the retrofitted joints increased by 34.69%, 29.47%, 25.99%, and 25.38% compared to the control joints, corresponding to reinforcement ratios of 0.99%, 1.44%, 1.95%, and 2.55%, respectively. Notably, the lowest percentage increases (25.38% and 25.99%) occurred at the highest reinforcement ratios (2.55% and 1.95%). This can be attributed to the shear failure observed in control joints at these high ρb values, where CFRP composites primarily acted as shear reinforcement, confining the joint core and mitigating brittle shear failure.

Conversely, the highest improvement in peak load (34.69%) was observed at the lowest beam reinforcement ratio ($\rho b = 0.99\%$), where flexural failure occurred in the control joint rather than joint shear failure. This was confirmed by the ductility observed in the load-displacement curve (Figure IV.3 ($\rho b = 0.99\%$)), indicating that beam flexural failure is more ductile than joint shear failure. In this case, the CFRP composite primarily functioned as a flexural strengthening material, effectively confining the beam and delaying the propagation of flexural cracks.

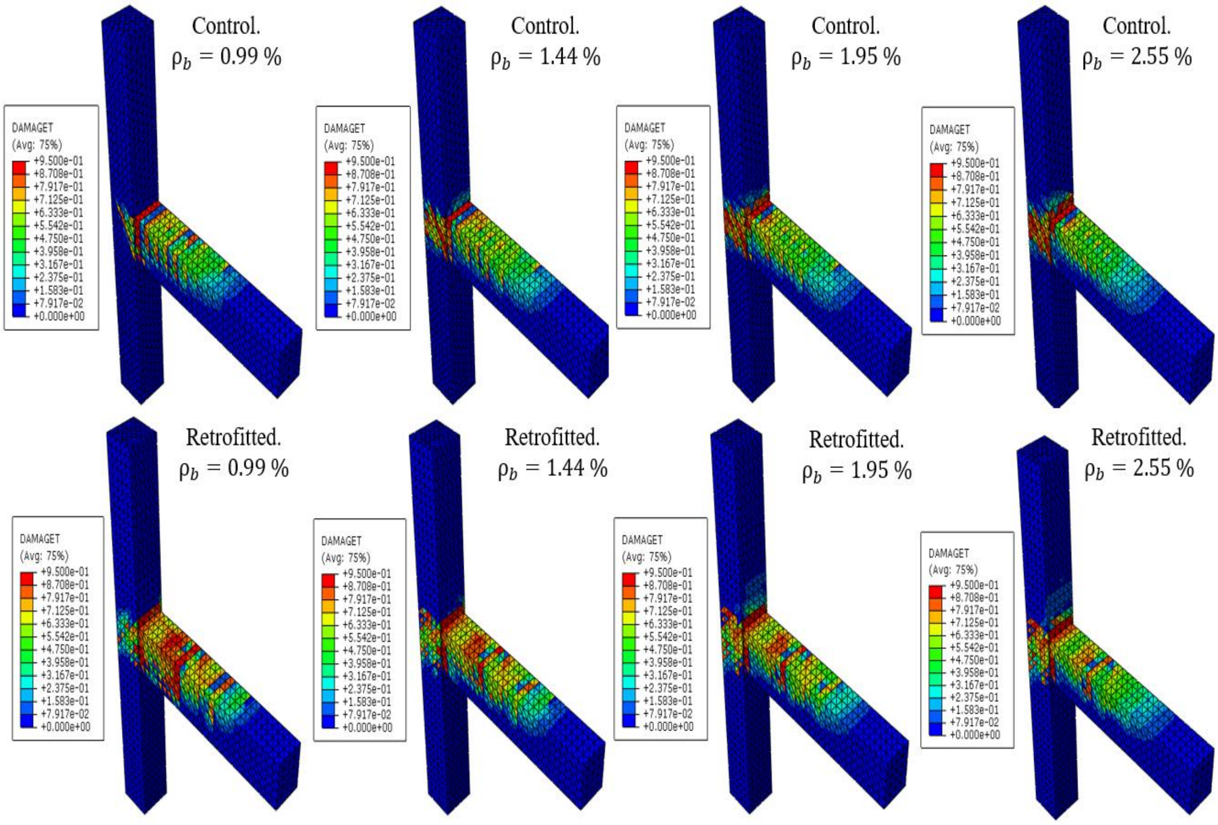

Figure IV.4. Crack patterns in numerically simulated BCJ units for different beam reinforcement ratios.

Figure IV.4 illustrates the damage distribution and crack patterns in the numerically simulated BCJ units for different beam reinforcement ratios. In control joints, extensive damage is observed in the beam for the lowest reinforcement ratio ($\rho b = 0.99\%$), indicating flexural failure. As ρb increases (1.44%–2.55%), the damage shifts toward the joint core, where severe diagonal shear cracks develop, signifying a transition from flexural to shear failure. This suggests that CFRP retrofitting primarily enhances joint shear resistance in cases with higher reinforcement ratios (1.44%–2.55%). In retrofitted joints, joint damage remains visible but is notably reduced compared to control specimens, with damage being more concentrated in the beam near the column face and at the CFRP cut-off point. Furthermore, as ρb increases, the intensity of beam damage decreases, demonstrating that the effectiveness of CFRP composites depends on the failure mechanism, whether occurring in the beam or within the joint core.

IV.4 EFFECT OF JOINT ASPECT RATIO

The impact of the joint aspect ratio ($\eta = h_b/h_c$) on the structural performance of retrofitted joints was analyzed through numerical simulations with different aspect ratios: $\eta = 1(h_b = 250\ mm)$, $\eta = 1.2(h_b = 300\ mm)$, $\eta = 1.4(h_b = 350\ mm)$, and $\eta = 1.6\ (h_b = 400\ mm)$. In these models, h_b and h_c represent the beam and column depths, respectively. The analyzed models incorporated transverse reinforcement within the joint core, consisting of two-leg horizontal stirrups placed at 50 mm intervals, complying with the maximum spacing requirements set by ACI 318-19 [50]. In order to maintain consistency in assessing the enhancement of shear capacity across different aspect ratios, all retrofitted joints were retrofitted using three layers of U-jacketing applied around the joint core.

The load displacement curves for the analyzed models are presented in Figure IV.5 with the corresponding numerical results summarized in Table IV-3.

Table IV-3. Numerical results for varying joint aspect ratio.

η	(P_u) kN		(Δ_u) (mm)		v_j (MPa)		Increase in P_u (%)
	Control	**Retrofitted**	**Control**	**Retrofitted**	**Control**	**Retrofitted**	
1.0	49.30	49.08	31.72	26.21	5.64	5.61	No increase
1.2	59.71	61.56	33.12	29.21	5.54	5.62	3.09
1.4	72.05	74.52	32.65	33.80	5.44	5.62	3.43
1.6	78.38	83.62	31.89	29.96	5.00	5.33	6.68

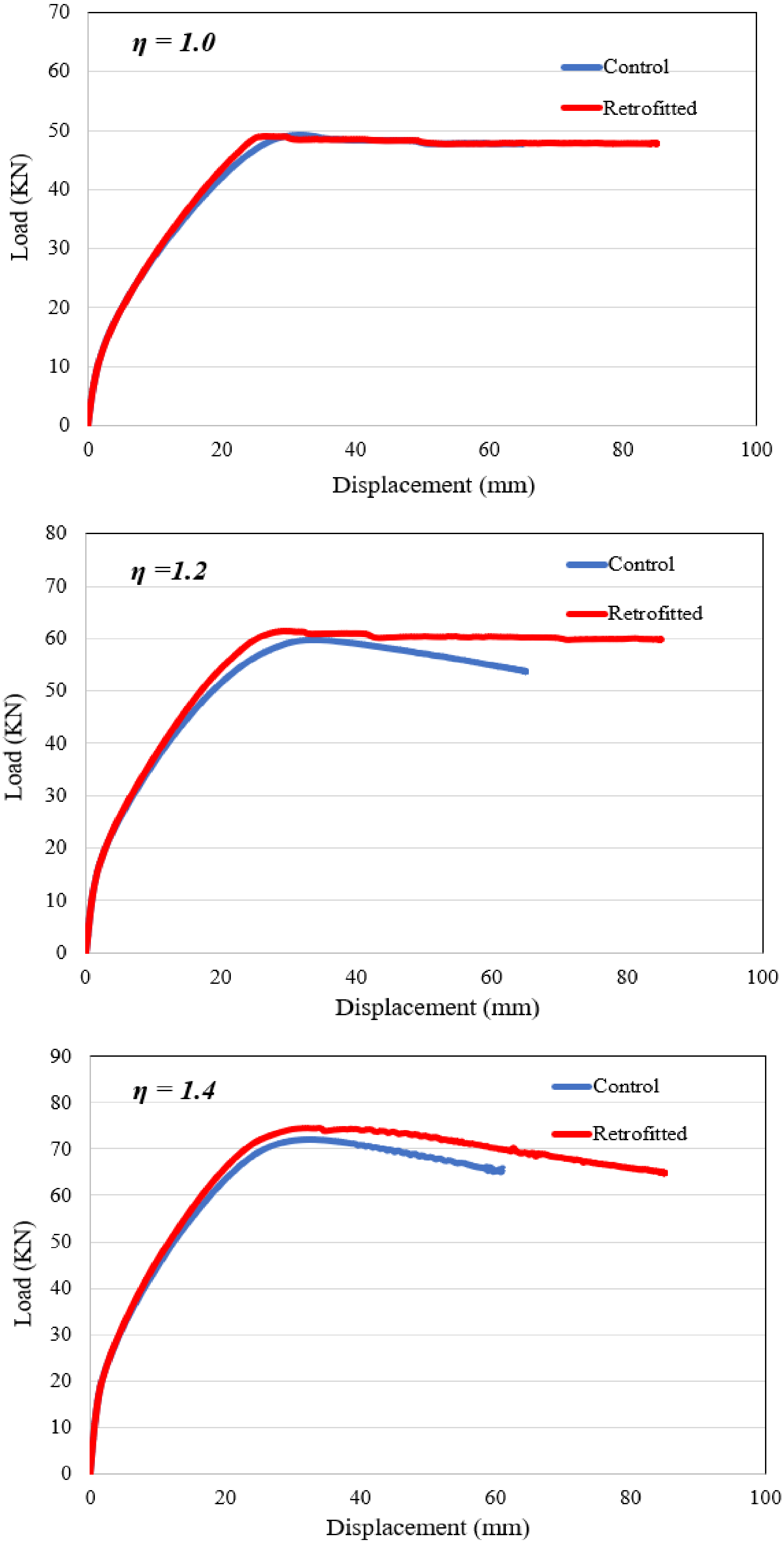

Figure IV.5. Effect of joint aspect ratio on the load displacement curves.

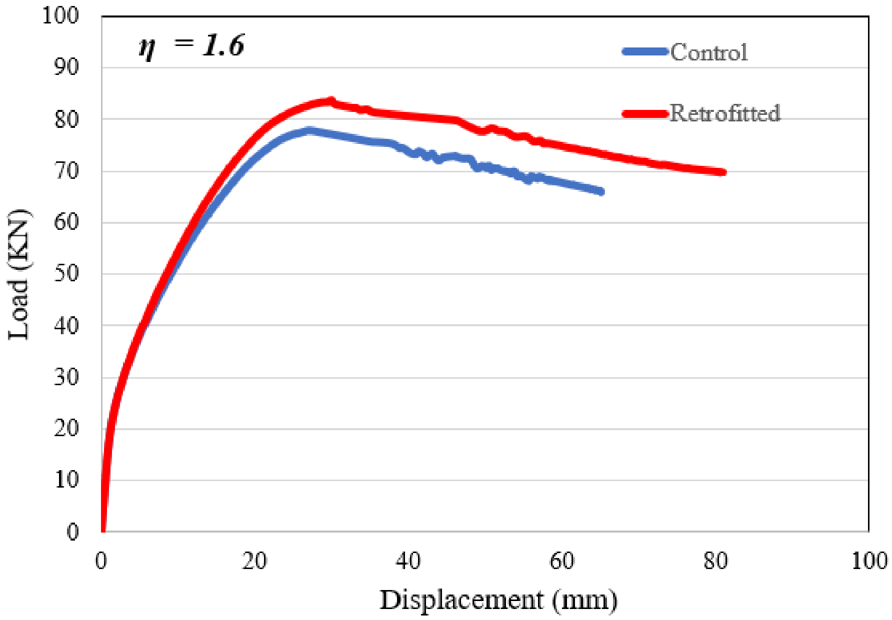

Figure IV.5. Continued.

The results indicate that for a joint aspect ratio of $\eta = 1$, the retrofitted joint does not exhibit any significant improvement in load-carrying capacity, with its load-displacement response closely resembling that of the control joint. This is likely due to the fact that the presence of horizontal stirrups had already enhanced the joint's shear capacity, rendering the U-jacketing CFRP composites ineffective in this scenario. However, for higher joint aspect ratios of $\eta = 1.2$, $\eta = 1.4$, and $\eta = 1.6$, the retrofitted joints demonstrate slight increases in peak load by 3.09%, 3.43%, and 6.68%, respectively. These improvements can be attributed to the role of joint aspect ratio in the overall resistance mechanism. As the aspect ratio increases, the joint's shear strength declines, enabling the CFRP confinement to contribute more effectively to enhancing its shear resistance of the joint.

The Von Mises stress distribution in the CFRP composites for different joint aspect ratios is presented in Figure IV.6. The results reveal a significant increase in induced stress intensity as the joint aspect ratio increases, indicating that CFRP composites become more effective in joints with higher aspect ratios. Additionally, Figure IV.6 highlights a noticeable trend of increasing stress concentrations with larger aspect ratios. This suggests that as the joint aspect ratio rises, its ability to distribute loads uniformly diminishes, allowing the CFRP reinforcement to play a more prominent role in enhancing the joint's structural performance.

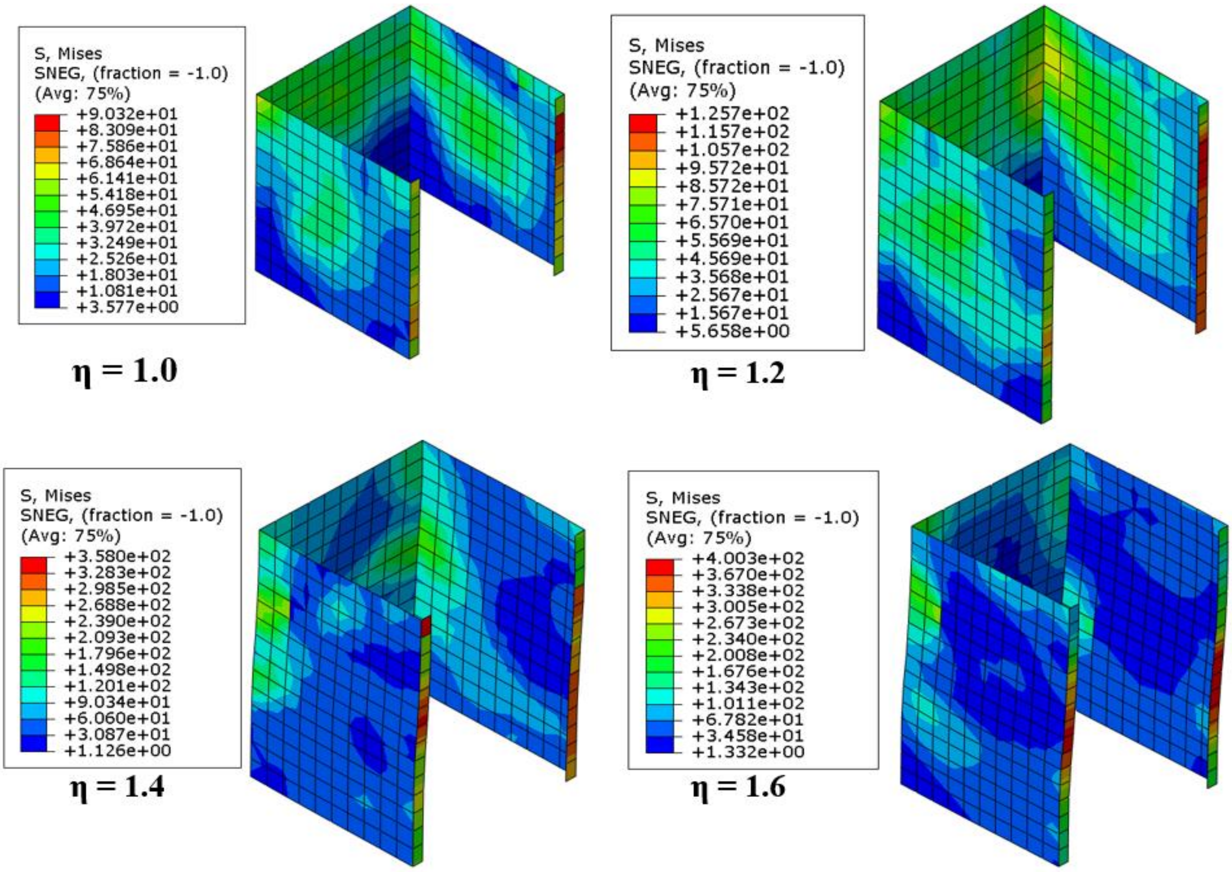

Figure IV.6. Stress variation in CFRP composites across different joint aspect ratios.

IV.5 EFFECT OF FIBER TYPE

This section investigates the effect of fiber type on the behavior of retrofitted BCJs. To this end, basalt fiber reinforced polymer (BFRP), a novel, eco-friendly, inorganic composite, was examined as a retrofitting material and compared with CFRP. To ensure a fair comparison of the influence of CFRP and BFRP composites on the shear capacity of the joint core, three layers of each material were applied using a U-jacketing configuration around the joint core. Furthermore, the comparison was conducted under varying column axial load ratios of 0.0, 0.1, 0.2, and 0.3.

The load-displacement curves for the different models investigated in this section are illustrated in Figure IV.7 , while the corresponding numerical results are presented in Table IV-4. In all cases of axial load ratios, the behavior of joints retrofitted with CFRP and BFRP exhibited a similar trend, with only slight variations in their load-displacement responses. However, CFRP consistently demonstrated the highest load-carrying capacity, outperforming BFRP in all cases. This can be attributed to CFRP’s superior strength and elastic modulus. Additionally, the difference in peak load between CFRP and BFRP decreases as the axial load ratio increases.

This can be explained by the fact that higher axial loads enhance the shear capacity of the joint, reducing the relative contribution of the composites in retrofitting the joint.

At an axial load ratio of 0.3, higher ductility was observed in the CFRP- and BFRP-retrofitted joints. This enhanced ductility is primarily attributed to the high axial load in the column and the confinement effect of the composite materials. In this case, the plastic hinge fully developed in the beam, with no shear cracks observed in the joint region. At the final stages of loading, BFRP-retrofitted joints exhibited significant strength degradation compared to CFRP-retrofitted joints. This reduction in strength is primarily due to damage evolution in the BFRP composite, which likely led to a loss of its reinforcing effectiveness.

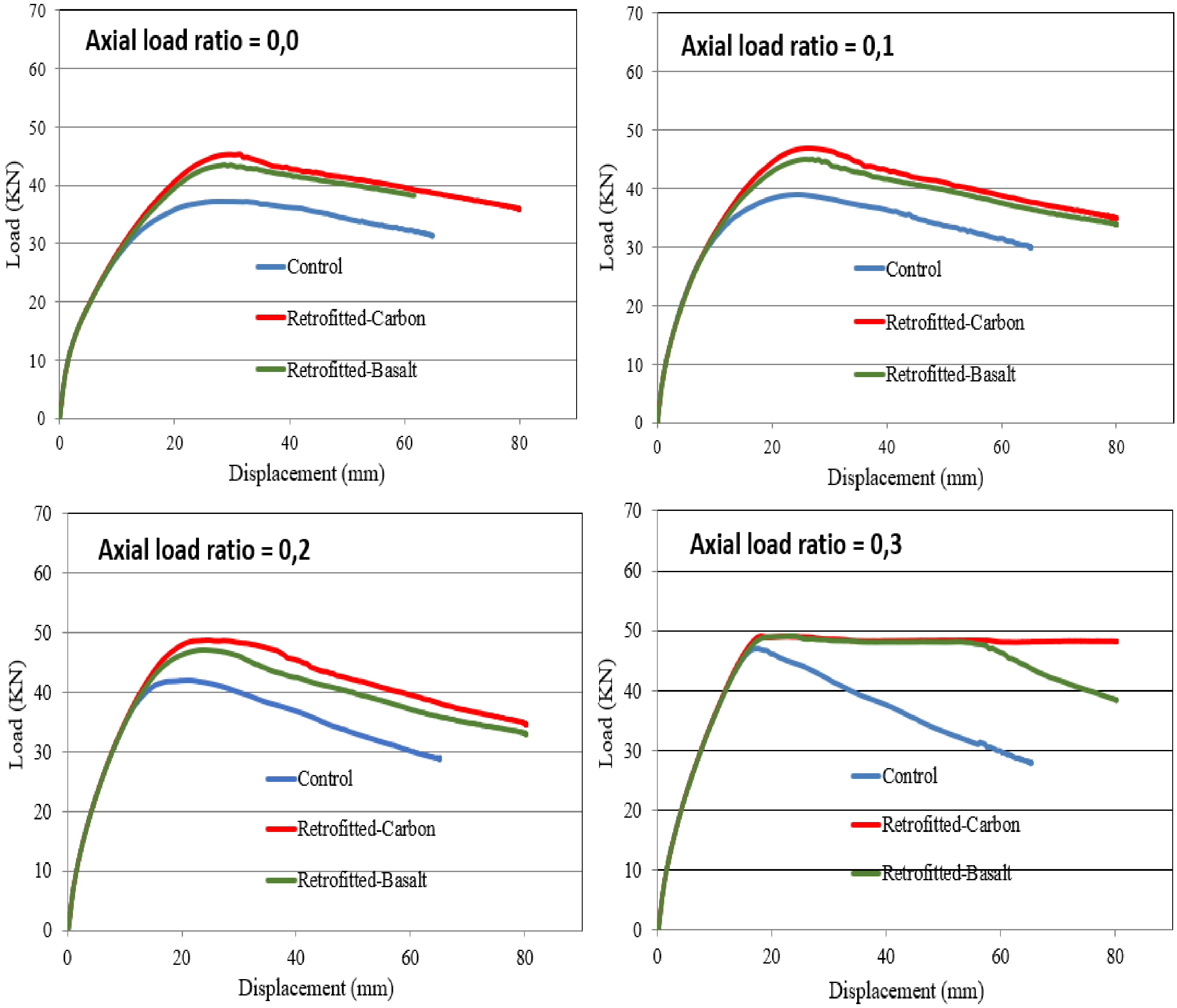

Figure IV.7. Comparative load-displacement response of CFRP and BFRP retrofitted BCJs under different axial load ratios.

Table IV-4. Numerical results showing the effect of fiber type on load capacity at different axial load ratios.

	Column axial load ratio	**(P_u) kN**	**(Δ_u) (mm)**	**Increase in P_u (%)**	**Difference in P_u (%) between CFRP/BFRP**
Control Joints	0.0	37.39	30.32	/	/
	0.1	39.01	24.85	/	/
	0.2	42.06	21.63	/	/
	0.3	47.00	17.05	/	/
Joints retrofitted with 3 layers of U-jacketing CFRP	0.0	45.45	31.42	21.55	4.50
	0.1	46.94	26.56	20.32	4.17
	0.2	48.66	24.53	15.69	3.26
	0.3	49.02	18.16	4.29	0.0
Joints retrofitted with 3 layers of U-jacketing BFRP	0.0	43.49	28.64	16.31	/
	0.1	45.06	26.02	15.50	/
	0.2	47.12	24.01	12.03	/
	0.3	49.00	19.59	4.25	/

General Conclusion

General Conclusion

This thesis presents a numerical study on retrofitting non-seismically designed BCJs using CFRP sheets with the grooving method, an alternative to conventional externally bonded reinforcement. Numerical simulations were conducted in ABAQUS, with results validated against experimental data from a recent study. ABAQUS/Explicit was employed to overcome convergence issues commonly encountered in ABAQUS/Standard due to the high nonlinearity of the problem. The CDP model was employed to simulate the nonlinear behavior of concrete, with sensitivity analyses conducted on its key parameters to assess their impact on the accuracy of numerical predictions. The Hashin failure criteria were applied to model CFRP damage, while the FRP-concrete interface was assumed to be a perfect bond, reflecting the strong adhesion provided by the grooving method. A strong correlation between numerical and experimental results confirms the reliability of the proposed model. Additionally, a parametric study was conducted to evaluate the effects of key design parameters, including column axial load ratio, beam reinforcement ratio, joint aspect ratio, along with joint reinforcement, and fiber type, on the effectiveness of the retrofitting technique.

Key Findings from the Literature Review:

1. RC beam-column joints in buildings constructed before modern seismic codes are prone to shear failure under seismic loads, as evidenced by experimental tests and post-earthquake observations.
2. The main deficiencies of pre-1970s non-seismic joints include a lack of transverse reinforcement in the joint core, inadequate beam reinforcement anchorage, and a strong beam–weak column design, leading to brittle failure mode.
3. Externally bonded FRP composites are effective for retrofitting but are highly susceptible to premature debonding, which limits their retrofitting potential.
4. Experimental studies confirm that the grooving method (EBROG) delays debonding, enhances FRP performance, and shifts the plastic hinge into the beam, improving joint behavior.
5. The combination of EBROG with FRP fan and wrap anchorages significantly enhances shear capacity and seismic performance of deficient BCJs.

Key findings from the finite element Modelling and Validation.

1. The proposed finite element model accurately captures the behavior of shear-deficient BCJs retrofitted using the GM, with the numerical predictions closely align with experimental results, with a peak load deviation limited to 7%.
2. Among the CDP model parameters, the dilation angle (ψ) and the K_c parameter have the greatest impact on the results. The default value of $K_c = 0.667$ provides the best accuracy, while the dilation angle requires careful calibration for reliable predictions.
3. Assuming a perfect bond between FRP and concrete produces results consistent with experimental observations, confirming the strong adhesion achieved through the GM.
4. The Hashin failure criteria realistically capture CFRP damage and post-peak behavior, ensuring better alignment between numerical and experimental results.
5. The numerical model demonstrated strong agreement with experimental results in terms of load-displacement envelope curves, peak loads, and failure modes, validating its effectiveness in simulating retrofitted BCJs.

Key findings from the Parametric Study.

1. A lower column axial load reduces the shear capacity of the joint core, allowing CFRP composites to contribute more effectively to shear resistance. This indicates that CFRP confinement becomes more beneficial when the joint experiences lower axial compression.
2. Under a lower beam longitudinal reinforcement ratio, it is essential to strengthen the beam near the column face to prevent premature beam flexural failure.
3. Increasing the joint aspect ratio reduces the joint shear capacity, allowing CFRP retrofitting to have a greater impact. This suggests that the retrofitting strategy is more beneficial for joints with higher aspect ratios.
4. Providing transverse reinforcement within the joint core as per ACI requirements enhances the joint's shear capacity, which in turn limits the effectiveness of CFRP retrofitting.
5. Basalt FRP (BFRP) composites can serve as a cost-effective alternative to CFRP for retrofitting BCJ, offering comparable retrofitting benefits with only a minor reduction in load-carrying capacity.

Bibliographic References

Bibliographic References

[1] Ong CB, Chin CL, Ma CK, Tan JY, Awang AZ, Omar W. Seismic retrofit of reinforced concrete beam-column joints using various confinement techniques: A review. Structures 2022;42:221–43. https://doi.org/10.1016/j.istruc.2022.05.114.

[2] Zabihi A. Seismic retrofitting of reinforced concrete beam-column joints using diagonal haunch 2020:235.

[3] Ghobarah A, Said A. Shear strengthening of beam-column joints. vol. 24. 2002.

[4] Clyde C, Pantelides C, Reaveley L. Performance-Based Evaluation of Exterior Reinforced Concrete Building Joints for Seismic Excitation Performance-Based Evaluation of Exterior. PEER Report Pacific Earthq Eng Res Cent 2000:1–49.

[5] Pantelides CP, Hansen J, Nadauld J, Reaveley LD. Assessment of Reinforced Concrete Building Exterior Joints with Substandard Details. Tech Rep No, PEER 2002, 18 2002:114.

[6] Wong HF, Kuang JS. Effects of beam-column depth ratio on joint seismic behaviour. Proc Inst Civ Eng Struct Build 2008;161:91–101. https://doi.org/10.1680/stbu.2008.161.2.91.

[7] Naser MZ, Hawileh RA, Abdalla JA. Fiber-reinforced polymer composites in strengthening reinforced concrete structures: A critical review. Eng Struct 2019;198:109542. https://doi.org/10.1016/j.engstruct.2019.109542.

[8] Siddika A, Mamun MA Al, Alyousef R, Amran YHM. Strengthening of reinforced concrete beams by using fiber-reinforced polymer composites: A review. J Build Eng 2019;25:100798. https://doi.org/10.1016/j.jobe.2019.100798.

[9] Sanginabadi K, Yazdani A, Mostofinejad D, Czaderski C. RC members externally strengthened with FRP composites by grooving methods including EBROG and EBRIG: A state-of-the-art review. Constr Build Mater 2022;324:126662. https://doi.org/10.1016/j.conbuildmat.2022.126662.

[10] Melo J, Engineering G, Varum H, Engineering F, Bisby L, Engineering E. Daniel A . Pohoryles , Scientific Project Officer , European Commission , Joint Research Centre (JRC), Ispra , Italy (corresponding author) n.d.:1–49.

[11] Ghobarah A, Said A. Shear strengthening of beam-column joints. vol. 24. 2002.

[12] Realfonzo R, Napoli A, Pinilla JGR. Cyclic behavior of RC beam-column joints strengthened with FRP systems. Constr Build Mater 2014;54:282–97. https://doi.org/10.1016/j.conbuildmat.2013.12.043.

[13] Antonopoulos CP, Triantafillou TC. Experimental Investigation of FRP-Strengthened RC Beam-Column Joints. J Compos Constr 2003;7:39–49. https://doi.org/10.1061/(asce)1090-0268(2003)7:1(39).

[14] Le-Trung K, Lee K, Lee J, Lee DH, Woo S. Experimental study of RC beam-column joints strengthened using CFRP composites. Compos Part B Eng 2010;41:76–85. https://doi.org/10.1016/j.compositesb.2009.06.005.

[15] Karayannis, C. G., and Sirkelis, G. M. (2008). “Strengthening and rehabilitation of RC beam–column 1074 joints using carbon-FRP jacketing and epoxy resin injection.” Earthquake Engineering & 1075 Structural Dynamics, 37(5), 769–790.

[16] Wang GL, Dai JG, Bai YL. Seismic retrofit of exterior RC beam-column joints with bonded CFRP reinforcement: An experimental study. Compos Struct 2019;224. https://doi.org/10.1016/j.compstruct.2019.111018.

[17] Zaferani MJ, Shariatmadar H. Repair and retrofitting of external RC beam-to-column joints using the hybrid NSM + EBR method. Eng Struct 2022;263:114370. https://doi.org/10.1016/j.engstruct.2022.114370.

[18] Mostofinejad D, Mahmoudabadi E. Grooving as Alternative Method of Surface Preparation to Postpone Debonding of FRP Laminates in Concrete Beams. J Compos Constr 2010;14:804–11. https://doi.org/10.1061/(asce)cc.1943-5614.0000117.

[19] Mostofinejad D, Shameli SM. Externally bonded reinforcement in grooves (EBRIG) technique to postpone debonding of FRP sheets in strengthened concrete beams. Constr Build Mater 2013;38:751–8. https://doi.org/10.1016/j.conbuildmat.2012.09.030.

[20] Nagib MT, Sakr MA, El-khoriby SR, Khalifa TM. Cyclic behaviour of squat reinforced concrete shear walls strengthened with ultra-high performance fiber reinforced concrete. Eng Struct 2021;246:112999. https://doi.org/10.1016/j.engstruct.2021.112999.

[21] Khan MI, Al-Osta MA, Ahmad S, Rahman MK. Seismic behavior of beam-column joints strengthened with ultra-high performance fiber reinforced concrete. Compos Struct 2018;200:103–19. https://doi.org/10.1016/j.compstruct.2018.05.080.

[22] Mostofinejad D, Hajrasouliha M. 3D beam–column corner joints retrofitted with X-shaped FRP sheets attached via the EBROG technique. Eng Struct 2019;183:987–98. https://doi.org/10.1016/j.engstruct.2019.01.038.

[23] Mostofinejad D, Hajrasouliha M. Shear Retrofitting of Corner 3D-Reinforced Concrete Beam-Column Joints Using Externally Bonded CFRP Reinforcement on Grooves. J Compos Constr 2018;22. https://doi.org/10.1061/(asce)cc.1943-5614.0000862.

[24] Mostofinejad D, Akhlaghi A. Experimental Investigation of the Efficacy of EBROG Method in Seismic Rehabilitation of Deficient Reinforced Concrete Beam–Column Joints Using CFRP Sheets. J Compos Constr 2017;21:1–15. https://doi.org/10.1061/(asce)cc.1943-5614.0000781.

[25] Mostofinejad D, Akhlaghi A. Flexural strengthening of reinforced concrete beam-column joints using innovative anchorage system. ACI Struct J 2017;114:1603–14. https://doi.org/10.14359/51700953.

[26] Ilia E, Mostofinejad D. Seismic retrofit of reinforced concrete strong beam–weak column joints using EBROG method combined with CFRP anchorage system. Eng Struct 2019;194:300–19. https://doi.org/10.1016/j.engstruct.2019.05.070.

[27] Davodikia B, Saghafi MH, Golafshar A. Experimental investigation of grooving method in seismic retrofit of beam-column external joints without seismic details using CFRP sheets. Structures 2021;34:4423–34. https://doi.org/10.1016/j.istruc.2021.10.023.

[28] Saad AG, Sakr MA, El-korany TM. The shear strength of existing non-seismic RC beam-column joints strengthened with CFRP Sheets: Numerical and analytical study. Eng Struct 2023;291. https://doi.org/10.1016/j.engstruct.2023.116497.

[29] Baji H, Eslami A, Ronagh HR. Development of a nonlinear FE modelling approach for FRP-strengthened RC beam-column connections. Structures 2015;3:272–81. https://doi.org/10.1016/j.istruc.2015.06.003.

[30] Hognestad E, Hanson NW, Mchenry D. Concrete Stress Distribution in Ultimate Strength Design. ACI Journal Proceedings 1955;52: 455-80.

[31] Kent DC, Park R. Flexural members with confined concrete. Journal of the Structural Division 1971;52:455-80.

[32] Sato Y. Vecchio F. Tension stiffning and crack formation in reinforced concrete membres with fiber-reinforced polymer sheets. Journal of Structural Engineering 2003; 129: 717-24.

[33] Abu Tahnat YB, Dwaikat MMS, Samaaneh MA. Effect of using CFRP wraps on the strength and ductility behaviors of exterior reinforced concrete joint. Compos Struct 2018;201:721–39. https://doi.org/10.1016/j.compstruct.2018.06.082.

[34] ACI Committee 318**.** Building Code Requirements for Structural Concrete (ACI 318-14) and Commentary (ACI 318R-14). American Concrete Institute, Farmington Hills, MI; 2014..

[35] Tonidis M, Sharma A. Numerical investigations on the influence of transverse beams and slab on the seismic behavior of substandard beam-column joints. Eng Struct 2021;247:113123. https://doi.org/10.1016/j.engstruct.2021.113123.

[36] Melo J, Varum H, Rossetto T. Experimental assessment of the monotonic and cyclic behaviour of exterior RC beam-column joints built with plain bars and non-seismically designed. Eng Struct 2022;270. https://doi.org/10.1016/j.engstruct.2022.114887.

[37] El-Naqeeb MH, Abdelwahed BS. Nonlinear finite element investigations on different configurations of exterior beam-column connections with different concrete strengths in column and floor. Structures 2023;50:1809–26. https://doi.org/10.1016/j.istruc.2023.02.122.

[38] SIMULIA, Abaqus Analysis User's Guide. Dassault Systèmes Simulia Corp., Providence, RI, USA, 2014.

[39] Behnam H, Kuang JS, Samali B. Parametric finite element analysis of RC wide beam-column connections. Comput Struct 2018;205:28–44. https://doi.org/10.1016/j.compstruc.2018.04.004.

[40] Najafgholipour MA, Sarhadi F. A finite element study on the ultimate lateral drift capacity of interior reinforced concrete flat slab-column connections. Structures 2022;46:913–26. https://doi.org/10.1016/j.istruc.2022.10.128.

[41] Dassault Systèmes, Abaqus Analysis User's Guide, Version 6.5, Chapter 7.2, 2009. Available: https://classes.engineering.wustl.edu/2009/spring/mase5513/abaqus/docs/v6.5/books/gsx/default.htm?startat=ch07s02.html. [Accessed: 15-oct-2024].

[42] Genikomsou AS, Polak MA. Finite element analysis of punching shear of concrete slabs using damaged plasticity model in ABAQUS. Eng Struct 2015;98:38–48. https://doi.org/10.1016/j.engstruct.2015.04.016.

[43] Wosatko A, Pamin J, Polak MA. Application of damage-plasticity models in finite element analysis of punching shear. Comput Struct 2015;151:73–85. https://doi.org/10.1016/j.compstruc.2015.01.008.

[44] Al-Osta MA, Khan U, Baluch MH, Rahman MK. Effects of Variation of Axial Load on Seismic Performance of Shear Deficient RC Exterior BCJs. Int J Concr Struct Mater 2018;12. https://doi.org/10.1186/s40069-018-0277-0.

[45] El-Naqeeb MH, Abdelwahed BS, El-Metwally SE. Numerical investigation of RC exterior beam-column connection with different joint reinforcement detailing. Structures 2022;38:1570–81. https://doi.org/10.1016/j.istruc.2022.03.014.

[46] Lubliner J, Oliver J, Oller S, Onate E. A Plastic-Damage Model. Int J Solids Struct 1989;25:299–326.

[47] Jeeho Lee, Gregory L. Fenves. Plastic-Damage Model for Cyclic Loading of Concrete Structures. J Eng Mech 1998;124:892–900.

[48] El-Naqeeb MH, El-Naqeeb MH, Hassanli R, Ungermann J, Hegger J. Numerical modeling of the punching shear behavior of biaxially loaded RC footings. Eng Struct 2024;318:118747. https://doi.org/10.1016/j.engstruct.2024.118747.

[49] Saenz LP. Discussion of "Equation for the stress-strain curve of concrete" by Desayi and Krishnan. ACI J Proc 1964;61(9):1229–35.

[50] ACI Committee 318, Building Code Requirements for Structural Concrete and Commentary (ACI 318-19). American Concrete Institute: Farmington Hills, MI; 2019.

[51] Jankowiak T, Lodygowski T. Identification of parametres of concrete damage plasticity constitutive model. Foundations of Civil and Envirommental Engineering 2005; 6(1): 53-69.

[52] Hillerborg A, Modeer M, Petersson PE . Analysis of crack formation and crack growth in concrete by means of fracture mechanics and finite elements. Cem Conc Res 1976; 6:773-82.

[53] CEB-FIP-Model Code 1990: design code. London: Thomas Telford; 1993.

[54] Choobbor SS, Hawileh RA, Abu-Obeidah A, Abdalla JA. Performance of hybrid carbon and basalt FRP sheets in strengthening concrete beams in flexure. Compos Struct 2019;227. https://doi.org/10.1016/j.compstruct.2019.111337.

[55] Hashin Z. Failure Criteria for Unidirectional Fiber Composites. Journal of applied mechnics. 1980;47:329-34.

[56] Ngo MD. Renforcement au cisaillement des poutres béton armé par matériaux composites naturels (fibre de Lin). [Thèse de doctorat]. Université de Lyon; 2016.

[57] Gebreyohaness AS. Seismic Assessment of Pre-1936 Dual RC Wall-Riveted Steel Frame Buildings. Dep Civ Environ Eng 2013;1994.

[58] Bahraq AA, Al-Osta MA, Khan MI, Ahmad S. Numerical and analytical modeling of seismic behavior of beam-column joints retrofitted with ultra-high performance fiber reinforced concrete. Structures 2021;32:1986–2003. https://doi.org/10.1016/j.istruc.2021.04.004.

[59] Najafgholipour MA, Dehghan SM, Dooshabi A, Niroomandi A. Finite element analysis of reinforced concrete beam-column connections with governing joint shear failure mode. Lat Am J Solids Struct 2017;14:1200–25. https://doi.org/10.1590/1679-78253682.

[60] El-Naqeeb MH, El-Metwally SE, Abdelwahed BS. Performance of exterior beam-column connections with innovative bar anchorage schemes: Numerical investigation. Structures 2022;44:534–47. https://doi.org/10.1016/j.istruc.2022.08.034.

[61] Dooshabi A, Najafgholipour MA. Nonlinear finite element analysis of shear defective reinforced concrete beam to column connections strengthened with three practical techniques. Eng Fail Anal 2024;163:108535. https://doi.org/10.1016/j.engfailanal.2024.108535.